

PARAMETER-DEPENDENT DYNAMICS OF SPATIO-TEMPORAL SYSTEMS

by

Sayomi Kamimoto

A Dissertation

Submitted to the

Graduate Faculty

of

George Mason University

In Partial fulfillment of

The Requirements for the Degree

of

Doctor of Philosophy

Mathematics

Committee:

- _____ Dr. Evelyn Sander, Committee Chair
- _____ Dr. Ira Schwartz, Committee Member
- _____ Dr. Thomas Wanner, Committee Member
- _____ Dr. Matthew Holzer, Committee Member
- _____ Dr. David Walnut, Department Chair
- _____ Dr. Donna Fox, Associate Dean for
Student Affairs, College of Science
- _____ Dr. Fernando Miralles-Wilhelm, Dean,
College of Science

Date: _____

Fall Semester 2020

George Mason University

Fairfax, VA

Parameter-Dependent Dynamics of Spatio-Temporal Systems

A dissertation submitted in partial fulfillment of the requirements for the degree of
Doctor of Philosophy at George Mason University

By

Sayomi Kamimoto
Director: Dr. Evelyn Sander, Professor
Department of Mathematical Sciences

Fall Semester 2020
George Mason University
Fairfax, VA

Copyright © 2020 by Sayomi Kamimoto
All Rights Reserved

Dedication

To:

My sons Shin Young and Young Pal Stallings, who have grown up watching me grow in mathematics since their toddler-hoods.

My stepsons Martin and Antoine Mathias who have tried to teach me how to play Belote.

My mother Kikumi Kamimoto for giving me life.

My father Katsuzo Kamimoto for his quiet support from afar.

My parents-in-law Maryse and Edgard Mathias who have embraced me into their family unconditionally, and showed interests in my work as a gesture of their support.

My grandmother in Okinawa, Yoshiko Kamimoto, who is turning 99 this year. I might be getting a PhD but she will always be better than me at doing mental calculation.

My late grandmother in Nigata, Haru Oe, from whom I learned so many things in life.

My late piano teacher Walter Hautzig, for bringing me to the United States, although he thought he would make a pianist out of me.

Lastly but not least importantly, I dedicate this dissertation to my husband Emmanuel Benjamin Mathias for building a place called home in my heart. I probably would have given up on myself long before now without his endless cheers. May Every Woman Find Her Emmanuel Mathias.

Acknowledgments

My deepest gratitude goes to Dr. Evelyn Sander who tirelessly lead me from nothing to where I am today. You will always be my teacher wherever I go.

I would like to thank the Department of Mathematical Sciences at George Mason University, in particular the following professors for their warmest guidance: Dr. Flavia Colonna, Dr. Thomas Wanner, Dr. Matthew Holzer, Dr. Habier Antil and Dr Maria Emelianenko.

I would also like to thank an enormous support and team efforts from the Nonlinear Dynamics division of Plasma Physics section at the US Naval Research Laboratory. In particular: Dr. Ira Schwartz, the division head, his wife Janine Tucker, Dr. Jason Hindes and Dr. Ioana Triandaf.

Lastly, the following friends receive big thanks and hugs from me for their many years of just being there: Steven Beck, Yuko Izuhara Gordon, Thibault Meiland, Julia C. Braumiller, Livio Oboti, Andreas Kern, Andrew Sanders, and Joyce Hsiao.

Table of Contents

	Page
List of Tables	vii
List of Figures	viii
Abstract	xiii
1 Introduction	1
1.1 Parameter-dependent dynamics, spatio-temporal systems	1
1.2 Computer assisted study of red coral dynamics	3
1.2.1 Red coral population dynamics	4
1.3 Dynamics of swarms with communication delay	5
1.3.1 Swarms with range-dependent delay	8
1.3.2 Unstable modes and bi-stability in delay-coupled swarms	11
1.3.3 Future work	11
2 Computer Assisted Study of Red Coral Dynamics	13
2.1 Red coral population model	14
2.1.1 Description of the model	14
2.1.2 Fixed points of the coral population model	20
2.1.3 The basic reproduction number	21
2.1.4 The fixed point bifurcation diagram	22
2.1.5 Oscillations	23
2.2 Branch validation and continuation	28
2.2.1 The constructive implicit function theorem	29
2.2.2 Continuation and an extended system	33
2.2.3 Preconditioning the coral map	44
2.3 Validation of the bifurcation points	45
2.3.1 Validation of the Neimark-Sacker bifurcation point	45
2.3.2 Validation of the saddle-node bifurcation point	53
2.3.3 Validation of the transcritical bifurcation point	55
2.4 Conclusion	56
3 Dynamics of Swarms with Communication Delay	57

3.1	Swarms with range-dependent delay	58
3.1.1	The swarm model	60
3.1.2	Mean-field equation of range dependent delay coupled swarm	65
3.1.3	Numerical analysis of the mean field equation	67
3.1.4	Conclusions	70
3.2	Unstable modes and bi-stability in delay-coupled swarms	72
3.2.1	Swarming pattern and stability	73
3.2.2	Conclusion	81
3.3	Future work: On interacting swarm dynamics	81
3.3.1	Statement of the problem	82
3.3.2	Background and relevance of previous work	82
3.3.3	General methodology and procedures	84
3.3.4	Explanation of new or unusual techniques	86
3.3.5	Expected results and their significance	87
	Bibliography	89

List of Tables

Table	Page
2.1 Observational red coral data from [24]. Our calculations are based on their fitting functions given in (2.1) and (2.2), which were established using this data.	17
2.2 Validation constants for the system (2.19) at the Neimark-Sacker bifurcation point. All values are written with four decimal places, unless less accuracy is known. For more efficient computation, we multiplied by a preconditioning matrix and determined the bounds ρ , K , and L_1 . We selected a matrix close to the Jacobian matrix of H_{ns} , whose inverse was used as a preconditioner. The accuracy constant δ_1 and the isolation bound δ_2 were derived using ρ , K and L_1 . For the three conditions (c), (d), and (e), which were checked separately after the validation involving H_{ns} , we used an interval arithmetic enclosure of the approximate solution with radius δ_1 . Note that the angle in (d) is given in degrees.	49
2.3 Validation constants for the extended system in (2.21) at the saddle-node bifurcation point. All values are written up to four decimal places. For more efficient computation, we multiplied by a preconditioning matrix and obtained the bounds ρ , K , and L_1 . We selected a matrix close to the Jacobian matrix of H_{sn} , whose inverse was used as a preconditioner. The accuracy constant δ_1 and the isolation bound δ_2 were derived using ρ , K , and L_1 . For the two conditions (c) and (d), which were checked separately after the validation involving H_{sn} , we used an interval arithmetic enclosure of the approximate solution with radius δ_1	53

List of Figures

Figure	Page
1.1 Photographs of red coral colonies. The individual polyps are visible particularly in the right-hand image. Photos from [5, 27]	4
1.2 Diagram of a global coupled delay swarm model	7
1.3 Drones used in the experiments in the works presented. Photo from [17] . .	8
1.4 Diagram of swarm with range dependent delay discussed in [75]	9
2.1 Polyp is a tiny jellyfish like creature that forms a colony. The new colonies are called recruits. From [5]	15
2.2 Life cycle of the coral population	16
2.3 The recruits-to-larvae ratio function ϕ plotted with respect to polyp density P	18
2.4 The bifurcation diagram of polyp density P as a function of the reproductive number R . While the diagram covers the range $R \in (12, 300)$, the birth rate data collected by Bramanti et al. in [52] are for $R \approx 29$	22
2.7 Invariant cycles for ten (left) and 500 (right) different parameter values. Even though we are guaranteed that some of the cycles contain stable periodic orbits, the periods are sufficiently high and the parameter ranges for which they exist are sufficiently small that it is hard to see them even in a close zoom (not depicted). Each orbit was computed using 100,000 iterates.	24
2.5 Dynamical behavior of some sample orbits of the red coral population model. All of these figures show the temporal evolution of the polyp population density P , and they are simulated over a time frame of 100 years each, at various parameter values.	25

- 2.6 After the Neimark-Sacker bifurcation, oscillating orbits appear. After removing transients in the orbit, the orbit lies on an invariant closed curve. On the left, we plot the x_1 - and x_2 -components of these limit cycles. As the parameter R increases, the size of the closed curve increases. For large values of R , the coral population is close to the extinction point at the origin. On the right, the same orbits are shown with respect to R , along with the corresponding unstable fixed points at the same parameter value.

2.8 The rotation number for the cycles shown in Figure 2.7 (top left) and a close up view of the rotation numbers (top right), this time with one million iterates. The periodic orbits are of such high periods that we cannot detect the devil's staircase type behavior of the rotation number within the Arnold tongue locking regions. The rotation number is computed using the angle difference between successive values of (x_1, x_2) , computed with respect to the point $(x_1, x_2) = (2500, 2500)$, and the angle versus angle difference is depicted here (bottom) for the cycles for ten different R values. The minimum occurs at the angle pointing towards the extinction point.

2.9 A schematic depiction of the constructive implicit function theorem. The theorem guarantees that under appropriate hypothesis, an approximate zero (blue dot) guarantees that within a uniqueness region (orange region) there is a curve in the zero set with a unique point at each fixed α value (red curve), and the this curve is located within an accuracy region (blue region). The uniqueness region contains the accuracy region. It is bounded in norm by straight lines, and the accuracy region is bounded in norm by parabolas. . .

2.10 Left, the validated bifurcation diagram of polyp density P as a function of the reproductive number R , along with the three validated bifurcation points. The blue curve consists of 5000 continuation steps, corresponding to 5000 linked boxes, for the preconditioned map with $\alpha = 0.8 \delta_\alpha$. The initial validated box contains $(R, P) = (300, 3256)$, which is in the upper right corner of the bifurcation diagram, and the last validated box contains $(R, P) = (71.91, 1.493)$, which is close to the green transcritical bifurcation point. For comparison purposes, 4000 continuation steps for the unconditioned map are shown in red within the extremely small square region in the upper right-hand corner. Right, the norm of the uniqueness region of the solution. As the solution gets near the transcritical bifurcation at the origin, the uniqueness region gets smaller. This is expected, since there is no longer any uniqueness when the two branches of the solution curve meet.

32

2.11 A schematic diagram of the the pseudo-arc length continuation method. Top left image: The result guarantees a uniqueness region for the zero set. This takes place in an adapted coordinate system, meaning that the box is slanted, but the uniqueness region is still bounded by straight lines. Since we only continue the curve in one direction, this figure only depicts the left half of the uniqueness region. The center line segment of this region is given by $(\lambda_k^*, u_k^*) + \alpha(\mu_k, v_k)$ for $0 \leq \alpha \leq \delta_\alpha$. At a fixed α value, we use Newton's method to find the next approximate zero along the line $(\lambda_k^*, u_k^*) + \alpha(\mu_k, v_k) + (\sigma, x)$, where (σ, x) denotes the vector pointing from $(\lambda_k^*, u_k^*) + \alpha(\mu_k, v_k)$ to the point $(\lambda_k^*, u_k^*) + \alpha(\mu_k, v_k) + (\sigma, x)$, and which is orthogonal to (μ_k, v_k) . Top right image: After we fixed the value $\alpha = \alpha^*$, we label this next approximation $(\lambda_{k+1}^*, u_{k+1}^*)$. Bottom image: Inside the uniqueness region (orange) is an accuracy region (blue). The accuracy region is bounded by curves which are parabolic in norm in the adapted coordinate system.

34

2.12 Left image: Associated with each successive approximation, there is a uniqueness region and an accuracy region. Right image: In order to guarantee that the k -th and $(k + 1)$ -st region enclose the same component of the zero set (the green curve), we must verify the linking condition. This requires that the accuracy curve of the $(k + 1)$ -st box at $\alpha = 0$ (such as the blue point on the upper edge of the $(k + 1)$ -st blue box) is contained in the uniqueness region of the k -th box (orange region).	42
3.1 Three basic swarm states.	59
3.2 Three snapshots of swarm state in space for $\epsilon = 0.01, a = 2.0, \tau = 1.75$. Sample times $t_0, t_1 = t_0 + 20, t_2 = t_0 + 40$	63
3.3 Left: Swarm Ring State $\epsilon = 0.01, a = 2.0, \tau = 1.75$. (a) Time series of the x-component of a single agent. (b)The power spectrum, that was computed by FFT method in MATLAB, showing a sharp frequency. (c) A phase portrait of the orbit of a single agent. Right: Swarm instability $\epsilon = 0.25, a = 2.0, \tau = 1.75$. (a)Time series of the x-component of a single agent. (b)The Power spectrum showing a slight broadening and birth of a new frequency. (c)A phase portrait of the orbit of a single agent.	64
3.4 Poincare map of Eqs. 3.1-3.4 for (a) $\epsilon = 0.25$, (b) $\epsilon = 0.5$. Other parameters are fixed: $a = 2.0, \tau = 1.75$. See text for details.	65
3.5 Periodic motion of the mean field Eq. 3.9 for $\epsilon = 0.01, a = 0.64, \tau = 1.6$. (a) Time series of the x-component of the mean field. (b) Power spectra of the time series.	67
3.6 Quasi-periodic motion of the mean field Eq. 3.9 for $\epsilon = 0.01, a = 0.64, \tau = 1.609$. (a) Time series of the x-component of the mean field. Solid (red) line denotes period length of dominant spectral peak. Dashed line denotes period length of secondary peak. (b) Power spectra of the time series.	68
3.7 Bifurcation plot on the mean field equation showing the L^2 norm of the periodic orbits as a function of delay τ . Parameter $a=0.68$. Red (blue) markers denote unstable (stable) orbits.Cyan symbols denote the change in stability where a pair of complex eigenvalues cross the imaginary axis.	70

3.8	Plotted is the locus of points at which torus bifurcations emerge as a function of coupling amplitude a , delay τ for various range radii ϵ for the mean field Eq. 3.9.	71
3.9	Stability diagram for delay-coupled swarms. (a) The blue (upper) curve denotes a Hopf bifurcation for the ring state (b, upper). The red (lower) curve denotes a combined line for saddle-node and double-Hopf bifurcations for the rotating state (b, lower). Points denote simulation-determined stability changes for $N = 600$: a ring state with all agents rotating in the same direction (blue circles), a ring state with half the agents rotating in the opposite direction (blue squares), and a rotating state (red diamonds). (b) Snapshots for both states in the x-y plane ($a = 1, \tau = 2.6, N = 100$). Positions are drawn with red circles and velocities with blue arrows. In all panels $m = \alpha = \beta = 1$	75
3.10	Frequency of unstable modes near bifurcation. (a) unstable frequency for the ring state at the Hopf bifurcation (black line) determined from the power spectrum of the swarm's center-of-mass (red circles). (b) unstable frequency for the rotating state at the double-Hopf bifurcation (black line) determined from the power spectrum for a single agent. Inlet panels show example spectra for both states: (a) when ($a = 1.565, \tau = 3.243$), (b) when ($a = 3.5, \tau = 1.059$). In all panels $m = \alpha = \beta = 1$	77

Abstract

PARAMETER-DEPENDENT DYNAMICS OF SPATIO-TEMPORAL SYSTEMS

Sayomi Kamimoto, PhD

George Mason University, 2020

Dissertation Director: Dr. Evelyn Sander

Dynamical systems with intricate behavior are pervasive in many fields of science such as biology, physics, climatology, ecology, engineering and robotics. Many of the most curious processes indicate the presence of a bifurcation, that is a phenomenon where a small change in a system parameter causes changes in qualitative behavior of the dynamics. Some dynamical systems are also characterized by a well defined spatial organization like a swarm of drones or red coral population models, for instance. In order to properly describe their dynamics, one must take into account both their spatial and temporal properties. Overall, mathematical theoretical works in dynamical systems investigate the stability of constant steady states, the existence of non-constant steady states, and bifurcation, which can be used to deduce a standard parameter control relation and in return can provide a theoretical basis for numerical simulations and experiments.

There are two parts in this dissertation. In the first part, we present a systematic study of red coral population model, shedding light on the long-term dynamics of the red coral populations. We can see the long-term effect of change in reproduction fitness as a parameter. We establish the equilibrium structure and bifurcation points for the model, find a set of stable periodic invariant cycles, and show that for a large range of reproduction fitness these cycles get close to population extinction.

In addition to these observations, we present and implement methods which allow us to rigorously validate the model's equilibrium and bifurcation structure. From a mathematical point of view, the advantage of rigorously validated computations is such that the outcomes can be used as components in the building of mathematical theorems along with other properties of the dynamical system.

In the second part, we introduce the analysis of bifurcation structures and numerical simulations of a delay-coupled swarm model. We typically rely on mean-field equations to analytically predict transitions between regimes of different collective swarm motions as a function of model parameters, such as delay and coupling amplitude. However, the mean-field does not capture global bifurcation behavior, such as multi-stability. By correctly identifying the relevant spatio-temporal modes, we are able to accurately predict unstable oscillations beyond the mean-field dynamics and multi-stability in large swarms. In addition, we present that when communicating networks of a swarm have range-dependent delays, rotational pattern in the swarm, which are typically periodic, undergo a bifurcation and create swarm dynamics on a torus. The observed bifurcation yields additional frequencies into the dynamics, which may lead to quasi-periodic behavior of the swarm.

Chapter 1: Introduction

1.1 Parameter-dependent dynamics, spatio-temporal systems

A dynamical system consists of a set of possible states together with a rule that determines the present state in terms of past states. The rule is deterministic if we can determine the present state uniquely from the past states. If there is a randomness in a rule, that is called a random or stochastic process. For example, a mathematical model for the price of wheat as a function of time would be able to predict today's price to be that of yesterday plus or minus some quantities with the two possibilities equally likely. If the rule is applied at discrete times, it is called a discrete-time dynamical system which is also called a map. A discrete dynamical system takes the current state as an input and updates by producing a new state as an output. A continuous dynamical system is the limit of discrete system with smaller and smaller updating times. The governing rule in that case becomes a set of differential equations and the term continuous-time dynamical system is used [88].

Dynamical systems with intricate behavior are pervasive in many fields of science such as biology, physics, climatology, ecology, engineering and robotics. Many of the most curious processes indicate the presence of a bifurcation, that is a phenomenon where a small change in a system parameter causes changes in qualitative behavior of the dynamics [46]. Bifurcation theory has become a rich field of research in its own right and evaluating the bifurcation behavior of a given dynamical system can be challenging, and we most often have to rely on numerical solvers or simulations to aid our analysis. Overall mathematical theoretical works in dynamical systems investigate the stability of constant steady states,

the existence of non-constant steady states, and bifurcation, which can be used to deduce a standard parameter control relation and in return can provide a theoretical basis for numerical simulations and experiments.

Some dynamical systems are also characterized by a well defined spatial organization like a swarm of drones [2], aggregation of bacteria [9] or red coral population models [52], for instance. In order to properly describe their dynamics, one must take into account both their spatial and temporal properties. Especially from a physical point of view, one should note that interactions in space can give rise to large scale spatio-temporal patterns such as spiral waves, spatio-temporal turbulence, stationary patterns and transitions between these modes. Complex spatio-temporal systems may exhibit irregular behaviors when driven far from equilibrium. Those are systems exhibiting nonlinear, non-stationary, and possibly even chaotic behavior which is generally difficult to model or analyze as their occurrence and properties are largely independent of the precise interaction structure. Our aim is to understand the robustness of the systems to changes in the mathematical model of a problem; this could inform efforts in various field of studies in order to understand or prepare for an abrupt transitions that may occur as system parameters drift.

In this dissertation, we will discuss two aspects of parameter-dependent dynamics of spatio-temporal systems. The computer assisted study of red coral population dynamics found in the second chapter is a joint work with Hye Kyung Kim, Evelyn Sander and Thomas Wanner, that will appear in *Pure and Applied Functional Analysis* [45]. The second portion of the thesis deals with understanding the dynamics of large scale swarms with communication delay. First two sections of the third chapter are part of the work at Nonlinear Dynamical Systems Section of Plasma Physics Division of the US. Naval Research Laboratory. The first section, Large-scale swarms having range-dependent delay, was published in [75] jointly with Ira B. Schwartz, Victoria Edwards, Klimka Kasraie, M. Ani Hsieh, Ioana Triandaf and Jason Hindes. The second section, Unstable modes and bi-stability in delay-coupled swarms, appeared in [39] with Jason Hindes, Victoria Edwards, Ioana Triandaf and Ira B. Schwartz. We conclude the last chapter of the dissertation with the discussion of

future work, which will be done in the capacity of National Research Council postdoctoral research associateship, tenured at the U.S. Naval Research Laboratory.

1.2 Computer assisted study of red coral dynamics

We often are unable to follow a particular solution with complete certainty because there is round off error in the calculations or we are using some numerical scheme to find the solution. In particular to the setting of zero finding problems in dynamical systems, we rely on root finding solvers so that accuracy of fixed point finding methods matters. We are interested to know whether the approximate solution we calculate is related to a true solution of the exact equations. In rigorous numerics, also known as computer assisted proofs, we care about providing a mathematically rigorous statement about the validity of a concrete numerical simulation, unlike scientific computing where the goal is to achieve highly reliable result for a very complicated problem.

Likewise, unlike numerical analysis where the analysis is a tool to develop a sophisticated computational methods to solve applied problems, our primary focus is to use computational framework to construct mathematical statements in order to establish the numerical result as a theoretical proof. The distinction is that there are some convergence and error statements for the general or typical numerical case, but there is no rigorous statement that we have not found a worst case in which the numerics did not work as advertised. With rigorous numerics, we are able to guarantee every single case that we calculate is as good as we claim. In the second chapter, we concentrates on implementing techniques to establish such proofs for equilibrium depending on a parameter in a dynamical system.

Rigorous numerics requires a setup that allows analysis and numerics to go hand in hand. In the context of equilibria branch validation, we need to find

1. A good numerical approximation of the equilibrium, usually by using Newton's method.
2. A mathematical theorem which establishes an actual zero near the approximation, including error bounds.

3. A computational framework which allows us to verify the assumptions of the theorem rigorously

The implicit function theorem is modified in such a way that is better suited for the use in numerics in a sense that we can actually go beyond “the existence” and come up with a particular value of a rigorous bound of the neighborhood in which the theorem guarantees the unique zero of the fixed point equation that is calculated numerically [73]. Besides mathematical theorems, rigorous validation uses the tool of interval arithmetic. The interval arithmetic is done by controlling, enclosing and propagating rounding and truncation errors which are inherent problems in computer numbers. With all the ingredients in place, we can provide a mathematically rigorous statement about the validity of the numerically calculated bifurcation diagram. In our work, we have used the interval arithmetic package INTLAB within MATLAB [69, 71].

1.2.1 Red coral population dynamics



Figure 1.1: Photographs of red coral colonies. The individual polyps are visible particularly in the right-hand image. Photos from [5, 27].

Red coral is a foundation of many Mediterranean ecosystems as it provides critical habitat for other marine lives. It is long lived and slow growing, and is now endangered due to over-harvesting, pollution, ocean acidification and global warming [51]. Bramanti, Iannelli, and Santangelo [24, 52] investigated red coral populations by scraping samples off the coast

of Italy in Calafuria in the Western Ligurian Sea, and observing their growth rate over a four-year period. They used this data to construct a Leslie-Lewis transition matrix, a static life table, and a 13-dimensional dynamical population model. Using this model, they studied population trends by comparing small young colonies and bigger older colonies. However, they only considered a small range of population trends. We present a systematic study of this coral population model, shedding light on the long-term dynamics of the red coral populations. We can see the long-term effect of change in reproduction fitness. We establish the equilibrium structure and bifurcation points for the model, find a set of stable periodic invariant cycles, and show that for a large range of reproduction fitness these cycles get close to population extinction.

In addition to these observations, we present and implement methods which allow us to rigorously validate the model's equilibrium and bifurcation structure, including both a saddle-node and a Neimark-Sacker bifurcation. These validations use a modification of the Newton-Kantorovitch type method developed in [73, 89, 90]. The previous version of this method merely used natural continuation. However, the natural continuation is not the numerical state of the art, and therefore we extended the rigorous method to the numerically efficient method. The current work being presented contains an extension of these results in which we consider rigorous validation using pseudo-arc length continuation [30, 47]. In addition, we use computer-assisted proof methods to prove the existence of saddle-node and Neimark-Sacker bifurcation points on the equilibrium branch. These methods significantly extend the range of applications of the constructive implicit function theorem which was introduced in [73].

1.3 Dynamics of swarms with communication delay

A swarm is a coordinated group of individuals, such as a flock of birds, a school of fish, African locusts, or a collection of interacting drones. Swarms consist of individuals with

simple rules but can self-organize into complex structures. As a result of this social interaction, one sees emergent collective behavior and dynamic pattern formation in a swarm. These systems are particularly interesting to the robotics community because they allow simple individual agents to achieve complex tasks in ways that are scalable in communication topology, extensible in space, and robust to failures of individual agents [48]. Given the many examples across a wide range of space and time scales, significant progress has been made in understanding swarming by studying simple dynamical models with general properties [1, 62, 86].

In addition, these swarming behaviors are able to form and persist in spite of complicating factors such as delayed actuation, latent communication, localized number of neighbors each agent is able to interact with, heterogeneity in agent dynamics, and environmental noise. These factors have been the focus of previous theoretical research in describing the bifurcating spatial-temporal patterns in swarms [42, 63, 76, 82]. Likewise, the application of swarms have been experimentally realized in areas, such as mapping [68], leader-following [64, 91], and density control [58]. To guarantee swarming behavior experimentally, control is typically employed [14, 26, 44, 80, 87] to prove convergence to a given state by relying on strict assumptions to guarantee the desired behavior. However, by relaxing certain assumptions, a number of studies show that even with simple interaction protocols, swarms of agents are able to converge to organized, coherent behaviors in a self-emergent manner; i.e. autonomously without control.

In almost all swarm models, there exists only a relatively small number of controllable parameters since the agents have just a few simple rules. The parameter set usually consists of a self-propulsion force, a potential function governing attracting and repelling forces between agents. Consider a system of mobile agents, or swarmers, moving under the influence of three forces: self-propulsion, friction, and mutual attraction. In the absence of attraction, each swarmer tends to a fixed speed, which balances propulsion and friction but has no preferred direction. The agents are assumed to communicate through a network with time delays. Namely, each agent is attracted to where its neighbors were at some moment

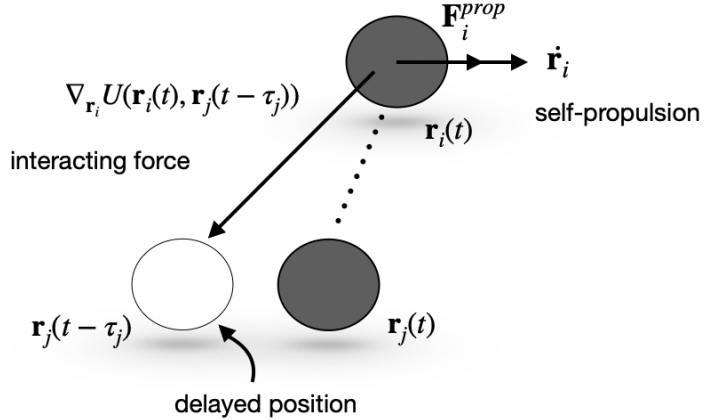


Figure 1.2: Diagram of a global coupled delay swarm model

in the past. A general model for N interacting self propelled agents in the plane based on Newton's laws of motion. The equation of the i -th particle is given by:

$$\ddot{\mathbf{r}}_i = \kappa_i \mathbf{F}^{\text{prop}}(\mathbf{r}_i(t)) - \kappa_i \sum_{j \in \mathcal{N}_i} \nabla_{\mathbf{r}_i} U(\mathbf{r}_i(t), \mathbf{r}_j(t - \tau)).$$

where \mathbf{F}^{prop} is a self-propulsion and frictional drag forces given by $(1 - ||\dot{\mathbf{r}}_i||^2)\dot{\mathbf{r}}_i$. The parameter τ_{ij} represents the time delayed position of r_j relative to r_i , and \mathcal{N}_i is a set of nodal connections to i . κ_i is a heterogeneous acceleration factor, a is a coupling amplitude. For $U : \mathbb{R}^{2n} \rightarrow \mathbb{R}$, a potential function of the two agents' position, we use a spring potential with short-range repulsion:

$$U(\mathbf{r}_i, \mathbf{r}_j^\tau) = c_r e^{-\frac{||\mathbf{r}_i - \mathbf{r}_j||}{l_r}} - \frac{a}{2N} (|\mathbf{r}_i - \mathbf{r}_j^\tau|^2), \quad \mathbf{r}_j(t - \tau_j) = \mathbf{r}_j^\tau.$$

In both robotic and biological swarms, an additional parameter appears as a delay between the time information is perceived and the actuation (reaction) time of an agent.

Such delays have now been measured in swarms of bats, birds, fish, and crowds of people [19, 28, 65].

Understanding the effects of delay is key to understanding many swarm behaviors in natural, as well as engineered, systems. The theoretical approach is in conjunction with ongoing experiments conducted in mixed reality swarm research at the US. Naval Research Laboratory.

1.3.1 Swarms with range-dependent delay

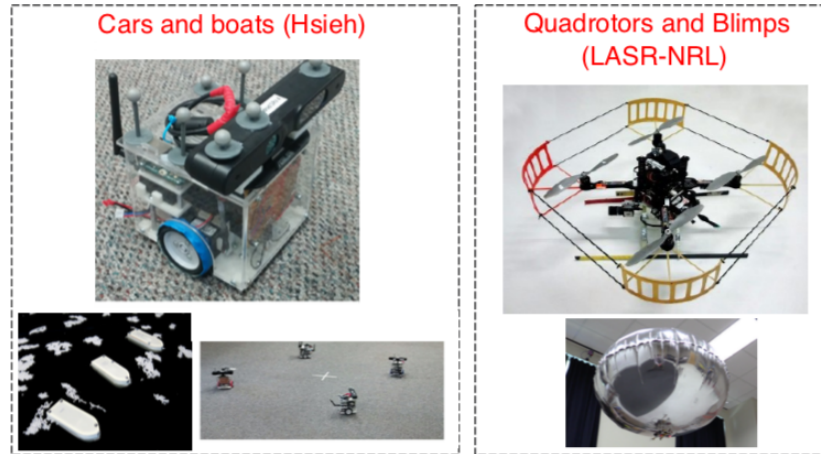


Figure 1.3: Drones used in the experiments in the works presented. Photo from [17]

Previously, there have been a number of studies done for fixed delay [42, 78]. Based on the previous work of global coupled delay case, we consider range dependent distributed delay which is novel and more realistic for swarm analysis. The basic idea is that if the delayed distance is within an ϵ ball, then we evaluate the coupling without delay and otherwise the delay is on. As $\epsilon \rightarrow 0$, we recover the global coupling delay case, for which we already know some basic structures of dynamics.

The relative distances of j -th agent(s) with respect to the i -th agent, a distance function can be computed as:

$$D_{i,j}^\tau \equiv \|\mathbf{r}_i - \mathbf{r}_j^\tau\|.$$

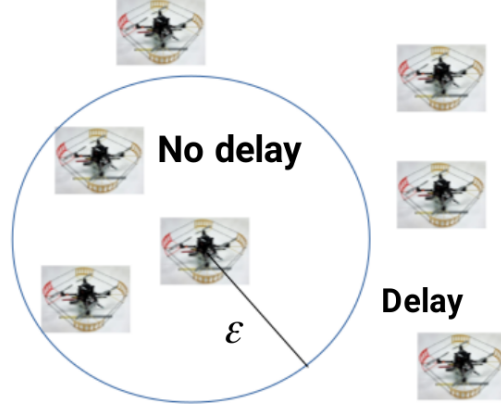


Figure 1.4: Diagram of swarm with range dependent delay discussed in [75]

We use Heaviside function $H(x)$, that is zero when $x \leq 0$, and 1 otherwise. Then we have the coupling term at the i -th agent as:

$$C_i = -\frac{a}{N} \sum_{j \in \mathcal{N}_i} (\mathbf{r}_i - \mathbf{r}_j^\tau) H(D_{i,j}^\tau - \epsilon) \\ - \frac{a}{N} \sum_{j \in \mathcal{N}_i} (\mathbf{r}_i - \mathbf{r}_j)(1 - H(D_{i,j}^\tau - \epsilon)).$$

Finally, the equation of the i -th particle for the range dependent delay case for the spring potential without repulsion is given by:

$$\ddot{\mathbf{r}}_i = \kappa_i \mathbf{F}^{\text{prop}}(\mathbf{r}_i(t)) - \frac{a}{N} \sum_{j \in \mathcal{N}_i} (\mathbf{r}_i - \mathbf{r}_j^\tau) H(D_{i,j}^\tau - \epsilon) - \frac{a}{N} \sum_{j \in \mathcal{N}_i} (\mathbf{r}_i - \mathbf{r}_j)(1 - H(D_{i,j}^\tau - \epsilon)).$$

This model contains individual agents and the simulations predict complex self-organized dynamic patterns which change as parameters of the model are varied. Our specific goal is to characterize this behavior as a function of physical parameters. We use a combination of computational packages and mathematical analysis in order to characterize the

dynamical behavior and locate bifurcation points of the delay differential equation that models the swarm. This allows us to predict bifurcations resulting from stability changes of delay-coupled swarms. We have done a number of numerical simulations by varying the communication delay and coupling strength, and we have observed some interesting dynamical behaviors of the center of mass of the swarm.

- In order to make the analysis of range-dependent case tractable, we consider the mean field of the full system as seen in the case of the global coupled delay model [94]. We used MATLAB toolbox DDE BIFTOOL, but bifurcation plots of the mean-field model in our publication were done with a compartment model for τ computed with AUTO. This bifurcation analysis could lead to a better understanding, leading to further simulation.
- The current model uses a spring potential. We plan to consider different potential functions such as a Morse potential. We will compare difference in the emerging pattern formation as a result. This will be further discussed in the future work.
- In order to capture more detailed behavior of the swarm not described by the mean field equation, it is necessary to test the relationship between the individual model and the mean field model, since mean field analysis is only relevant in the limit of large numbers. There are three types of behaviors in the swarms: translating, ring and rotating [94]. Our current mean field model is a first order approximation, and does not predict all behaviors such as bi-stability. A natural matter of a sequence seems to do a higher-order approximation of the mean-field, the technique that might predict bi-stability qualitatively, it suffers from quantitative inaccuracy and is difficult to analyze [95].

The last point leads to the topic discussed in the second section in the third chapter.

1.3.2 Unstable modes and bi-stability in delay-coupled swarms

We have demonstrated that generally, research on the spatio-temporal patterns of swarm dynamics presents results that are valid in the limit where the number of agents is assumed to be large. We typically rely on mean-field equations to analytically predict transitions between regimes of different collective swarm motions as a function of model parameters, such as delay, coupling amplitude, or the radius outside of which communication delay is assumed. However, there is a limitation to mean-field analysis in swarm dynamics since it does not capture global bifurcation behavior, such as multi-stability. We have shown that it is necessary to test the relationship between a whole swarm model and the mean-field model. By correctly identifying the relevant spatio-temporal modes, we are able to accurately predict unstable oscillations beyond mean-field dynamics and multi-stability in large swarms.

It is known that introducing time delays into the communication network of mobile-agent swarms produces coherent rotational patterns, from both theory and experiments. Often such spatio-temporal rotations can be bi-stable with other swarming patterns, such as milling and flocking. Yet, most known bifurcation results related to delay-coupled swarms rely on inaccurate mean-field techniques. As a consequence, the utility of applying macroscopic theory as a guide for predicting and controlling swarms of mobile robots has been limited. To overcome this limitation, we perform an exact stability analysis of two primary swarming patterns in a general model with time-delayed interactions. By correctly identifying the relevant spatio-temporal modes, we are able to accurately predict unstable oscillations beyond the mean-field dynamics and bi-stability in large swarms, laying the groundwork for comparisons to robotics experiments.

1.3.3 Future work

The proposed future work uses the foundation of single swarm dynamics towards a comprehensive analysis of multiple interacting swarms, a topic which is still in its infancy,

and remains an active area of research. Our aim is to develop new theories of interacting swarms dynamics in order to control multiple swarm behaviors. The future research will enable us to solve the problem of employing small and large swarms to sense and control other swarms. The interactions will be based on human leadership/animal hierarchical networks, but will be autonomous in application. Our results will aid in designing interacting swarms of robotic agents that can perform more complex tasks than a single swarm alone can, with resilience and robustness.

Chapter 2: Computer Assisted Study of Red Coral Dynamics

Coral plays an important role in the marine ecosystem, and coral reefs provide habitats to many sea animals and protect coastlines from breaking waves and storms. Red coral is a long-lived, slow-growing species, dwelling on Mediterranean rocky bottoms. Red coral populations are at risk due to both global climate change and overharvesting [51]. Bramanti, Iannelli, and Santangelo [24, 52] investigated red coral populations by scraping samples off the coast of Italy in Calafuria in the Western Ligurian Sea ($43^{\circ}30' N$, $10^{\circ}20' E$, Italy, at a depth between 20 and 45m depth) and observing their growth rate over a four-year period. They used this data to construct a Leslie-Lewis transition matrix, a static life table, and a 13-dimensional dynamical population model. Using this model, they studied population trends by comparing small young colonies and bigger older colonies. However, they only considered a small range of population trends. In the current chapter, we present a systematic study of this coral population model, shedding light on the long-term dynamics of the red coral populations. We can see the long-term effect of change in reproduction fitness. We establish the equilibrium structure and bifurcation points for the model, find a set of stable periodic invariant cycles, and show that for a large range of reproduction fitness these cycles get close to population extinction.

In addition to these observations, we present and implement methods which allow us to rigorously validate the model's equilibrium and bifurcation structure, including both a saddle-node and a Neimark-Sacker bifurcation. These validations use a modification of the Newton-Kantorovitch type method developed in [73, 89, 90]. While the previous version of this method merely used natural continuation, this chapter contains an extension of these results in which we consider rigorous validation using pseudo-arc length continuation [30, 47]. In addition, we use computer-assisted proof methods to prove the existence of saddle-node and Neimark-Sacker bifurcation points on the equilibrium branch. These methods

significantly extend the range of applications of the constructive implicit function theorem which was introduced in [73]. While for the purposes of this chapter we restrict ourselves to the case of finite-dimensional Euclidean spaces, the results can easily be adapted to the general Banach space setting, with little change. Thus, the pseudo-arc length results can be used for example in the setting of partial differential equations, such as the setting described in [74]. In other words, the present chapter presents a functional analytic foundation for using pseudo-arc length continuation in the context of computer-assisted proofs based on the constructive implicit function theorem presented in [73].

The remainder of this chapter is organized as follows. We introduce the age-based red coral model in Section 2.1. In addition, we present a bifurcation diagram of fixed points and stability of the model, along with a detailed discussion of oscillations. These results show how even at high fitness levels, the oscillations lead to extreme vulnerability of the population. Section 2.2 contains a functional-analytic approach to the rigorous validation of the regular branches in the bifurcation diagram, which is based on a constructive version of the implicit function theorem. Subsequently, Section 2.3 details the validation for the three bifurcation points on the main fixed point branch; namely, the saddle-node bifurcation in 2.3.2, the Neimark-Sacker bifurcation in 2.3.1, and the transcritical bifurcation in 2.3.3. Section 2.4 contains conclusions and future work.

2.1 Red coral population model

In this section we present the red coral population model of Bramanti, Iannelli, and Santangelo [24, 52], based on their experimental and field data and a Leslie-Lewis transition matrix. In addition, we describe the dynamics of the model in terms of its bifurcation structure and discuss its implications.

2.1.1 Description of the model

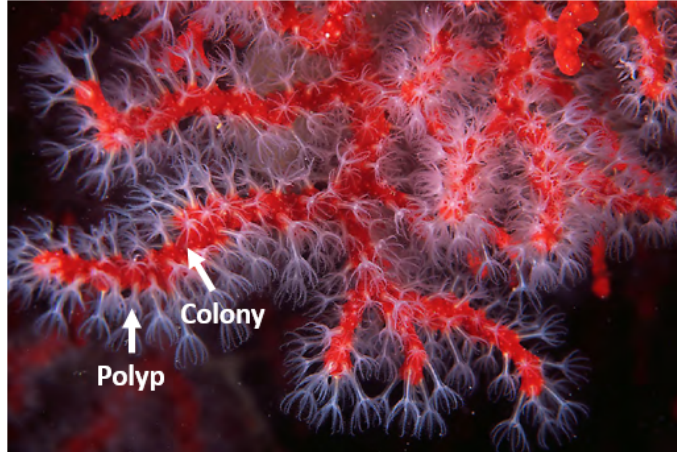


Figure 2.1: Polyp is a tiny jellyfish like creature that forms a colony. The new colonies are called recruits. From [5].

A coral population is a self-seeding independent group consisting of *polyps*, tiny soft-bodied organisms related to jellyfish. Polyps form into *colonies*, which are distinct clusters with polyps residing on a surface, as shown in Figure 1.1. A polyp is born to a parent colony in a free-swimming larval stage. At the end of the larval stage, the polyp permanently attaches itself to a colony and cannot move again. The age of a colony has implications in terms of its size and polyp density. As a result, colony age determines the polyp attachment rate, the larval birth rate, and the polyp survival rate. Based on these factors, larvae will attach either to an existing colony or, especially if there is a high polyp density, *recruitment* will occur. That is, larvae do not attach to existing colonies, but instead form new colonies. Red coral polyps can reproduce larvae starting two years after their birth, implying that there is no birth in a colony less than two years old, since none of the polyps are old enough to reproduce. Reproduction occurs at a discrete time in summer, implying that a discrete population model is a natural modeling assumption.

Based on the setting above, rather than modeling the total large number of polyps in a coral population, the age-based model is a discrete time model for (x_1, x_2, \dots, x_d) , where x_k is the number of colonies of age group k . The value d is the oldest colony in the population. While in principle this d could be large, in the observations made there was no colony of age

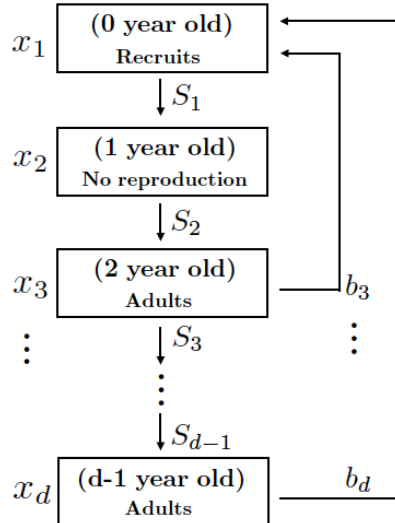


Figure 2.2: Life cycle of the coral population

group greater than 13. The value of x_k changes with respect to time (in years), where x_k^n denotes the number of colonies of age group k at year n . The colony life cycle is displayed in the schematic diagram shown in Figure 2.2. The downward arrows in Figure 2.2 indicate that x_{k+1} , the number of colonies in age group $k + 1$, is determined exclusively by the number of colonies in age group k in the previous year. This relation is linear with respect to population, with the survival rate constant S_k , i.e., we have $x_{k+1}^n = S_k x_k^{n-1}$. The survival rate values are determined by observation, and are given in Table 2.1, based on [24, Table 2].

The upward arrows Figure 2.2 indicate that recruits may be larvae from any colony of age two or greater. Though it is not obvious from the schematic diagram, the recruitment rate is not linear, and it depends on both the total number of polyps in the colonies, as well as on the larvae birth rates. Considering that the base variables x_k denote the number of colonies in age group k , the total number of polyps can be deduced from the numbers p_k of polyps per colony in a colony of age group k , and the birth rates b_k depend on the fertility rates F_k given in Table 2.1. Combined with the observational data in [52], Bramanti et al. have then derived empirical expressions for the polyp per colony numbers p_k and the birth

Class k	Survival rate S_k	Fertility F_k
1	0.89	0
2	0.63	0
3	0.70	0.36
4	0.52	0.64
5	0.44	0.82
6	0.29	0.97
7	0.57	0.98
8	0.33	0.99
9	0.75	1
10	1	1
11	0.33	1
12	1	1
13		1

Table 2.1: Observational red coral data from [24]. Our calculations are based on their fitting functions given in (2.1) and (2.2), which were established using this data.

rates b_k , which are given by

$$p_k = 1.239 k^{2.324} \quad \text{and} \quad b_k = F_k k^{2.324}. \quad (2.1)$$

For our calculations in the present section, we use these fitting functions rather than the original data, in keeping with the equations in [52]. In addition to the birth rates, the number of recruits x_1 depends also on a nonlinear function ϕ , which in turn depends on the density of polyps per unit area. This function ϕ is given by

$$\phi(y) = \frac{c_1 e^{-\alpha y}}{y^2 + c_2 e^{-\beta y}}, \quad \text{with} \quad c_1 = 1.8 \cdot 10^5, \quad c_2 = 1.3 \cdot 10^7, \quad (2.2)$$

$$\alpha = 5 \cdot 10^{-4}, \quad \beta = 3.4 \cdot 10^{-3},$$

which again is a fit for the observational data in [52]. The shape of this nonlinearity is depicted in Figure 2.3. For a small density of polyps, the function ϕ increases with polyp density, whereas too large of a polyp density inhibits the creation of new colonies due to

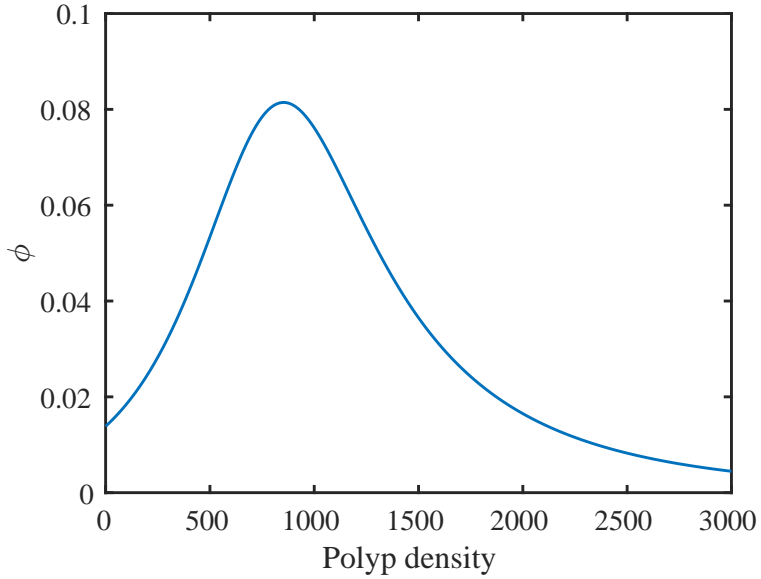


Figure 2.3: The recruits-to-larvae ratio function ϕ plotted with respect to polyp density P .

competition for resources.

We now explain how to compute the polyp population density P . We have already seen that the numbers p_k of polyps per colony in a colony of age group k satisfy the empirical formulas in (2.1). Thus, the total number of polyps in age group k is given by $p_k x_k$. Now let Ω denote the total area of the population site, which was measured to be equal to 36 dm^2 in [52]. Moreover, let $x = (x_1, x_2, \dots, x_d)$ be a column vector giving the number of colonies of each age group, and let $p = (p_1, p_2, \dots, p_d)$ denote the vector of polyps per colony in each age group. Then the total number of polyps in the (non-recruit!) population Q and the polyp population density P satisfy the identities

$$Q = \sum_{k=2}^d p_k x_k \quad \text{and} \quad P = \frac{Q}{\Omega}. \quad (2.3)$$

Based on these preliminaries, let $x^n = (x_1^n, x_2^n, \dots, x_d^n)$ represent the vector containing the number of colonies at year n , and let P be the polyp population density defined in (2.3). If

we now define

$$L(\lambda, x) = \begin{bmatrix} \lambda b_1 \phi(P) & \lambda b_2 \phi(P) & \dots & \lambda b_{d-1} \phi(P) & \lambda b_d \phi(P) \\ S_1 & 0 & \dots & 0 & 0 \\ 0 & \ddots & \ddots & & \vdots \\ \vdots & \ddots & \ddots & 0 & \vdots \\ 0 & \dots & 0 & S_{d-1} & 0 \end{bmatrix}, \quad (2.4)$$

where the bifurcation parameter λ is described below, then our model is given by

$$x^{n+1} = L(\lambda, x^n)x^n. \quad (2.5)$$

The model (2.4) and (2.5) is an age-structured, nonlinear, discrete-time dynamical model. For the parameter value $\lambda = 1$, it is precisely based on the observational data in [52]. The nonlinearity arises only in the evolution of the variable x_1 , which describes the number of recruit colonies. In a slight reformatting of notation, let the function $f : \mathbb{R} \times \mathbb{R}^d \rightarrow \mathbb{R}^d$ be given by $f(\lambda, x) = L(\lambda, x)x$. Then $x^{n+1} = f(\lambda, x^n)$, meaning that the dynamical population variation corresponds to the iteration of the parameter-dependent nonlinear map f .

We still have to justify the introduction of the bifurcation parameter λ in the above formulas. Previous work concentrated on the effect of varying the biologically relevant reproductive number R , the total number of larvae produced by a single colony during its life span. This parameter is directly proportional to λ , as we will show in Section 2.1.3. The birth rate parameters b_k in the above equation are determined by observation of a specific coral population over a small time period. In order to consider a population model in which the population is placed under stress, such as in the case of climate change, it is necessary to change the parameters beyond what has been observed. While we could also consider modification of other parameters, we choose to follow along the lines of [52] and vary the birth rates, making the assumption that every birth rate parameter will be equally affected.

Therefore, in our subsequent analysis, for every k we let the birth rate be given by λb_k , a fixed scaling factor compared to the originally observed birth rate.

2.1.2 Fixed points of the coral population model

We now consider the set of fixed points for the coral population model, given by the nonlinear function f defined above, and how this set changes as a function of the parameter λ . That is, we wish to determine the set of all pairs $(\lambda, x) \in \mathbb{R} \times \mathbb{R}^d$ such that $f(\lambda, x) = x$. As it turns out, this can be reformulated equivalently as a one-dimensional problem. To see this, assume that we have $x = f(\lambda, x)$. Then for all indices $k = 1, \dots, d-1$ one has $x_{k+1} = S_k x_k$. Using these statements iteratively, one readily obtains

$$x_2 = S_1 x_1 , \quad x_3 = S_2 S_1 x_1 , \quad \dots \quad x_d = S_{d-1} \cdots S_2 S_1 x_1 .$$

Thus, for all $k = 2, \dots, d$ we have $x_k = a_k x_1$, where one uses the abbreviation

$$a_k = \prod_{i=1}^{k-1} S_i , \tag{2.6}$$

and we further define $a_1 = 1$ then one also has $x_1 = a_1 x_1$. Since we can write each component x_k for $k \geq 2$ as a function of x_1 alone, the fixed point problem is a one-dimensional problem, which is only a matter of determining x_1 . Recall that we defined the polyp population density P in (2.3), and let $b = (b_1, b_2, \dots, b_d)$. Then the equation for x_1 is given by

$$x_1 = \lambda(b \cdot x) \phi(P) .$$

Moreover, let $a = (a_1, a_2, \dots, a_d)$. This immediately implies the identities

$$x = x_1 a , \quad P = \frac{x_1}{\Omega} \sum_{k=2}^d p_k a_k , \quad \text{and} \quad b \cdot x = (b \cdot a) x_1 .$$

Altogether, this shows that a vector $x = (x_1, \dots, x_d)$ is a fixed point for the map $f(\lambda, \cdot)$ if and only if $x = x_1 a$ and its first component x_1 satisfies the nonlinear equation

$$x_1 = \lambda (b \cdot a) x_1 \phi \left(\frac{x_1}{\Omega} \sum_{k=2}^d p_k a_k \right). \quad (2.7)$$

From this equation, one can then determine all fixed points of the coral population model. Notice that we clearly have the trivial solution $x = 0$ for all values of the parameter λ , which corresponds to an extinct population.

2.1.3 The basic reproduction number

An important biological parameter for the coral population is the total number of larvae produced by a single colony in its entire life span. This number only depends on the birth and survival rates, and one can easily see that it is given by

$$R = \lambda b_1 + \lambda b_2 S_1 + \lambda b_3 S_2 S_1 + \dots + \lambda b_d S_{d-1} S_{d-2} \dots S_1 = \lambda \sum_{i=1}^d a_i b_i. \quad (2.8)$$

The number R is called the *basic reproduction number*. Using the notation from the last subsection, the above equation can be rewritten as

$$R = (b \cdot a) \lambda. \quad (2.9)$$

In particular, while it is possible to vary R in such a way that the relationship between the birth rate constants vary, under our assumptions, the vectors b and a are fixed constant vectors, and we therefore have a fixed linear relationship between R and λ . To make it easy to compare our results with those of previous works, we have chosen to plot all bifurcation diagrams with respect to the basic reproduction number R .

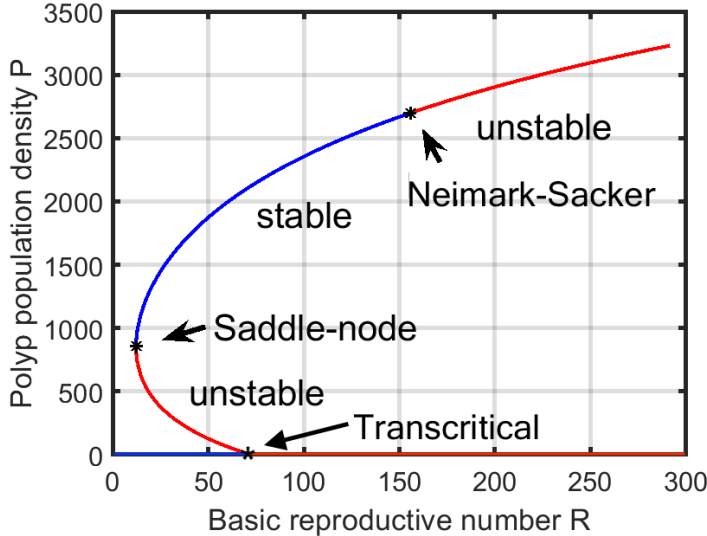


Figure 2.4: The bifurcation diagram of polyp density P as a function of the reproductive number R . While the diagram covers the range $R \in (12, 300)$, the birth rate data collected by Bramanti et al. in [52] are for $R \approx 29$.

2.1.4 The fixed point bifurcation diagram

We now turn our attention to a description of the bifurcation diagram of the fixed points for the coral population system. This diagram is shown in Figure 2.4, where the set of fixed points is plotted in terms of the reproductive number R versus polyp population density P . The color in the diagram depicts the stability of the fixed points, and the diagram indicates the existence of three bifurcation points: a saddle-node and a Neimark-Sacker bifurcation on the nontrivial branch, which itself bifurcates from the trivial branch at a transcritical bifurcation. While following subsections of this section will be used to verify the bifurcation diagram using computer-assisted proofs, the remainder of the current subsection is devoted to the discussion of dynamical aspects which are observed through numerical simulations.

Throughout our computations, we used the case of $d = 13$ age groups. The bifurcation diagram in Figure 2.4 was computed using a numerical continuation method starting at reproduction number $R = 300$, and allowing R to decrease. There appears to be a

saddle-node point for $R \approx 12.28$ (which corresponds to $\lambda \approx 0.4213$), after which the basic reproduction number R of the fixed points begins to increase again. In Section 2.3 we use a computer-assisted proof to rigorously validate this saddle-node bifurcation point. The curve continues further until the population density reaches zero, which corresponds to an extinct population. We will see later that the extinction point can be found explicitly, and that it occurs at $R \approx 72.22$ (which corresponds to $\lambda \approx 2.478$). Moreover, the stability of the trivial solution $x = 0$ can readily be determined from the Jacobian matrix of f at the origin, and this shows that the extinction fixed point is stable for small R , corresponding to low fitness, and unstable for all larger values of the basic reproduction number R , with instability index 1. The bifurcation between the extinction fixed point being stable and unstable occurs at the transcritical bifurcation point. All of these statements will be established rigorously in Section 2.3, including the appearance of the transcritical bifurcation point. Unlike the other two bifurcation points, no computer-assisted proofs are necessary along the trivial solution.

As mentioned before, the stability of the fixed points $x^* \in \mathbb{R}^{13}$ is indicated by color, with blue indicating stable fixed points and red representing unstable ones. The local stability at each fixed point in Figure 2.4 is determined numerically, based on whether all the eigenvalues of the Jacobian matrix $D_x f(\lambda, x)$ lie inside the unit circle or not. In the bifurcation diagram, we have not distinguished the index of the stability. If at least one of the eigenvalues lies outside the complex unit circle, then the fixed point is colored red, meaning unstable.

2.1.5 Oscillations

Figure 2.4 only shows the existence and stability behavior of fixed point solutions. But what about the dynamical behavior of the system? In this last subsection of Section 2.1, we focus on dynamical aspects of the model, in particular its oscillatory behavior on attracting invariant circles that form as a result of the Neimark-Sacker bifurcation. For a fixed parameter value $R > 154.1$ and for a typical initial condition, solutions converge to these invariant circles, and therefore the age-structured coral populations oscillate as time varies.

Figure 2.5 shows the dynamics of initial populations near fixed points, starting at a variety of different parameters and different initial aged-structured population vectors $y \in \mathbb{R}^{13}$. At reproduction number $R = 8.744$ (which corresponds to $\lambda = 0.3$), the solutions converge to the stable fixed point zero, i.e., the point of extinction. For $R = 29.15$ (corresponding to $\lambda = 1$), if we start at initial conditions ranging roughly from $0.15y$ to $2y$, where y is a vector of age-structured initial number of colonies which was chosen with polyp population density $P = 1500$, then solutions converge to a nontrivial stable fixed point. There is also an unstable fixed point denoted by the red line. In addition, one can observe bistability at this parameter value. If we start at a smaller value of P , such as for example at initial populations with polyp population density smaller than $0.15y$, solutions converge to zero, i.e., the coral population becomes extinct. At the basic reproduction number $R = 87.4437$ ($\lambda = 3$), though it takes longer time than 100 years, the solutions still converge to a stable nontrivial fixed point. In contrast, at $R = 160.31$ ($\lambda = 5.5$), population starting at $P = 1.5y$ oscillate. We used connected lines to show these oscillations more effectively, but recall that the map is in fact discrete.

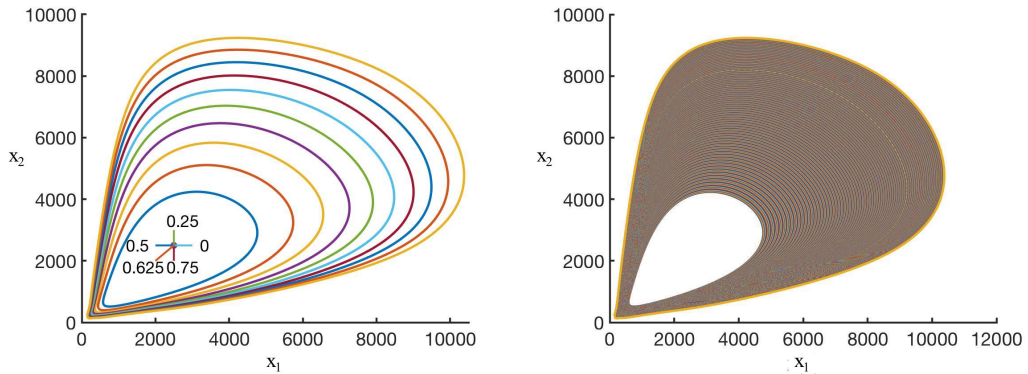


Figure 2.7: Invariant cycles for ten (left) and 500 (right) different parameter values. Even though we are guaranteed that some of the cycles contain stable periodic orbits, the periods are sufficiently high and the parameter ranges for which they exist are sufficiently small that it is hard to see them even in a close zoom (not depicted). Each orbit was computed using 100,000 iterates.

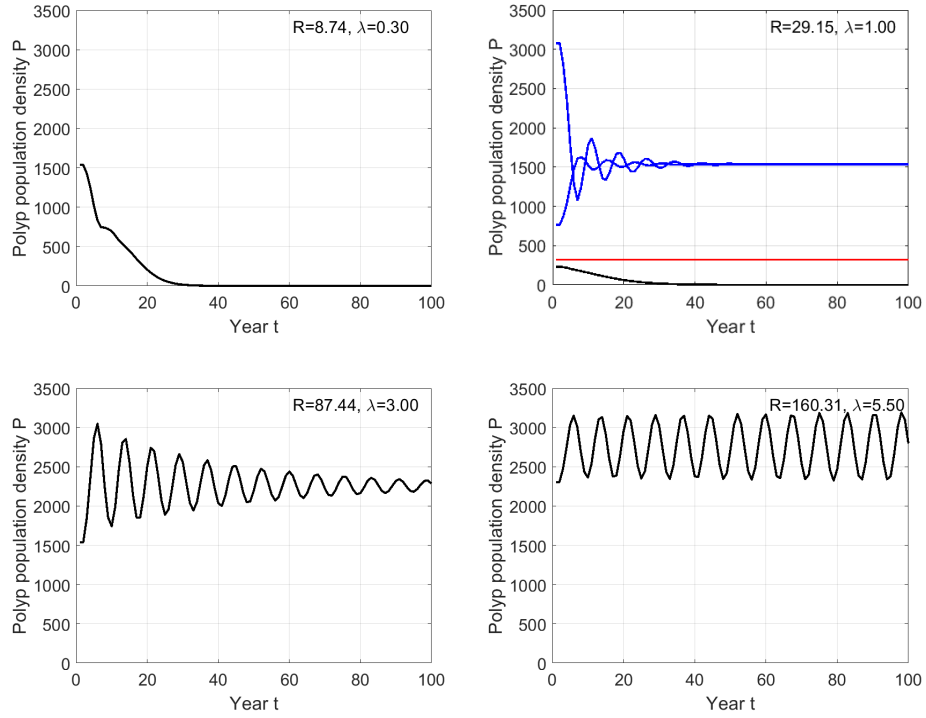


Figure 2.5: Dynamical behavior of some sample orbits of the red coral population model. All of these figures show the temporal evolution of the polyp population density P , and they are simulated over a time frame of 100 years each, at various parameter values.

The oscillations seen in the lower right subplot of Figure 2.5 form as a result of the Neimark-Sacker bifurcation. The fixed point stability switches from stable to unstable, and an invariant circle gains stability. Trajectories with initial conditions near fixed points but after the bifurcation are displayed in Figure 2.6. Perturbations around an unstable fixed point are repelled from the fixed point after the bifurcation, converging to an invariant closed curve. As the parameters R and λ increase, the size of the closed curve also increases, and the minimum population of a curve approaches the extinction point at the origin. That is, red coral populations become vulnerable at a large reproduction number, and a very small perturbation of the population would endanger the survival of the population despite the existing long recovery cycle.

In order to better understand the stable invariant limit cycles that form after bifurcation, we have computed the rotation number, meaning the average angle of rotation per iterate,

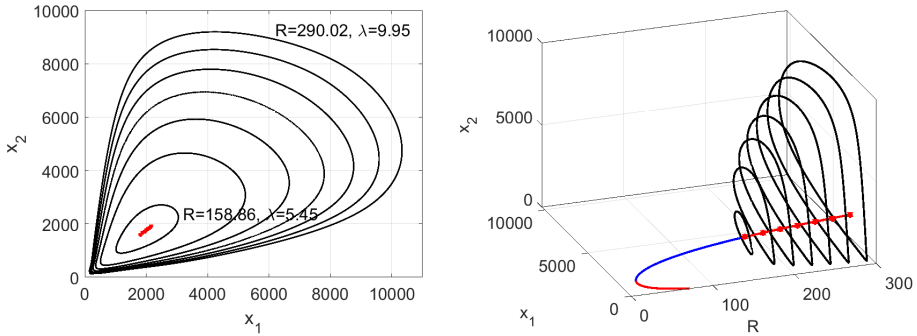


Figure 2.6: After the Neimark-Sacker bifurcation, oscillating orbits appear. After removing transients in the orbit, the orbit lies on an invariant closed curve. On the left, we plot the x_1 - and x_2 -components of these limit cycles. As the parameter R increases, the size of the closed curve increases. For large values of R , the coral population is close to the extinction point at the origin. On the right, the same orbits are shown with respect to R , along with the corresponding unstable fixed points at the same parameter value.

as a function of the parameter R . Specifically, we used the projection to the x_1x_2 -plane to compute the rotation numbers. Our computations are performed using the weighted Birkhoff average method described in [13]. Figure 2.7 shows cycles at ten distinct parameter values on the left, and for 500 distinct parameters on the right. The corresponding rotation numbers are shown in Figure 2.8. The values are angles, but they are rescaled to have values in the range $(0, 1)$. Each rotation number was computed by considering the angle difference between successive iterates when measured with respect to the point $(2500, 2500)$. To verify our numerics and check that we have used a sufficient number of iterates in our calculation, we compared the rotation number computed with 50,000 iterates to the rotation number computed with 40,000 for a series of test parameters. In these test parameters, the answer differs by 10^{-15} or less.

Note that we would expect to see a devil's staircase in the rotation numbers at the parameter values when there are periodic orbits, but what we see looks smooth even when quite zoomed in. This is due to the fact that the periodic orbits are extremely high period. In particular, we are able to use a Farey tree calculation to find the smallest denominator, corresponding to the lowest period, of a periodic orbit for the case of a rational rotation

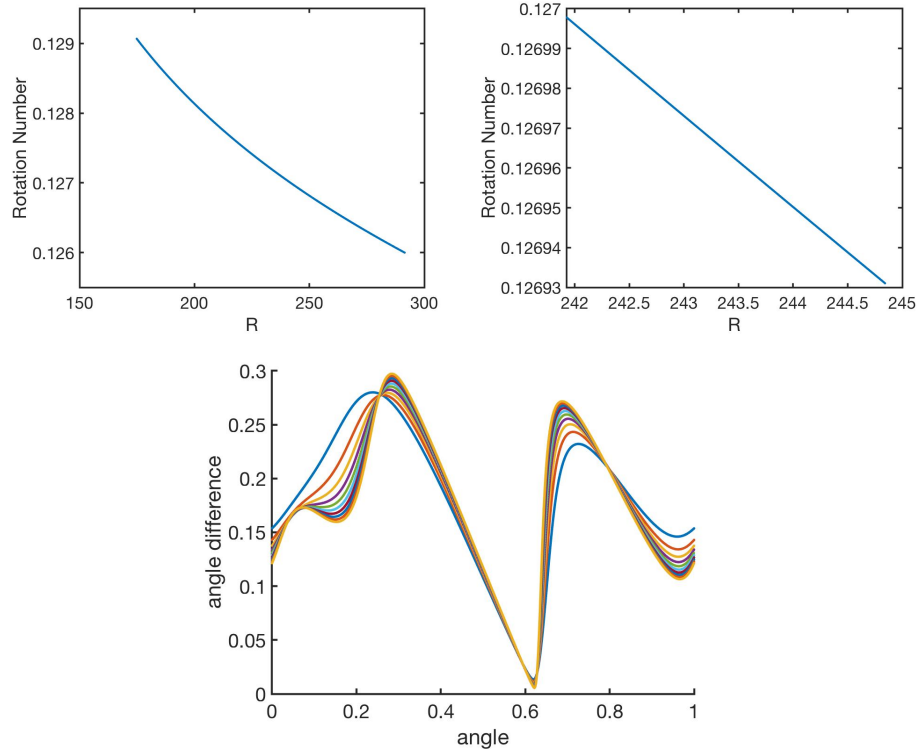


Figure 2.8: The rotation number for the cycles shown in Figure 2.7 (top left) and a close up view of the rotation numbers (top right), this time with one million iterates. The periodic orbits are of such high periods that we cannot detect the devil's staircase type behavior of the rotation number within the Arnold tongue locking regions. The rotation number is computed using the angle difference between successive values of (x_1, x_2) , computed with respect to the point $(x_1, x_2) = (2500, 2500)$, and the angle versus angle difference is depicted here (bottom) for the cycles for ten different R values. The minimum occurs at the angle pointing towards the extinction point.

number for this range of rotation numbers, using the method in [70, 72]. In particular, we find that the lowest denominator in the range $[0.126, 0.129]$ is 39 (fraction $5/39$). Not only is the lowest possible period quite large and therefore hard to distinguish from a limit cycle, but also the large periodicity implies that the Arnold tongue locking regions are very small parameter ranges, meaning that we are not able to resolve them without more delicate computations.

The average rotation number gives only the mean of how much the population is changing with respect to time. This leaves out some information as to how the change in population depends on the location of the population. In the bottom subplot in Figure 2.8, we show the angle difference as a function of the angle for ten different values of R . That is, for each point in the invariant circle, we graph how much the population is changing in one iterate (corresponding to one year) at each point in the invariant circle. The smallest angle difference, corresponding to the slowest change, occurs for angle ≈ 0.625 , corresponding to the values closest to the origin extinction point. Therefore, a portion of the invariant circles is getting dangerously close to the origin, such that a small perturbation could result in the extinction of the whole coral population. To compound matters further, the orbits are staying near the extinction point for longer than they remain in any other region, since at these points the observed angle differences are very close to zero. Thus the population remains extremely vulnerable for a particularly long time.

2.2 Branch validation and continuation

We now turn to the rigorous validation of fixed points, both for regular and bifurcation values. Our general approach is the constructive implicit function theorem from [73]. This is a rigorous result that combines with a numerical interval arithmetic calculation to give rise to a validated method for finding a branch in the zero set of a function which depends on a single parameter. In the following four subsections, we will first recall the constructive implicit function theorem, and then define an extended system which can be used for pseudo-arclength continuation. After that, we prove two results which form the basis of our approach, and describe the necessary preconditioning for the coral population model application.

2.2.1 The constructive implicit function theorem

Before stating the full result, here is a summary. Given an approximate zero (α^*, x^*) of a function $G(\alpha, x)$ where x is contained in a Banach space and $\alpha \in \mathbb{R}$, under certain hypotheses on G and its derivatives evaluated at the approximate zero (α^*, x^*) , combined with Lipschitz estimates near this point, there exist two regions in parameter and phase space. First, the *accuracy region*, which contains a curve of the zero set. Second, a *uniqueness region*, in which that zero set curve is unique. See the schematic in Figure 2.9. The blue dot shows the initial approximate zero. The orange curve is the zero set curve, which is guaranteed to lie within the accuracy region (the blue region). Note that the approximate zero does not in general lie on the zero set. The accuracy region is contained within the uniqueness region, shown in orange. The uniqueness region is largest in phase space when the parameter is closest α^* . As the parameter varies, the uniqueness region shrinks (meaning we have worse isolation). The constructive implicit function theorem guarantees that the uniqueness region is characterized by a linear norm condition, as depicted by the straight sides in the schematic diagram. The accuracy region has best (i.e., smallest) accuracy when the parameter is near the parameter of the original point α^* . The accuracy region grows (meaning we have worse accuracy) with a quadratic norm condition. This is depicted schematically by its parabolic shape. We now state the formal theorem.

Theorem 2.2.1 (Constructive Implicit Function Theorem). *Let \mathcal{P} , \mathcal{X} , and \mathcal{Y} be Banach spaces, suppose that the nonlinear operator $G : \mathcal{P} \times \mathcal{X} \rightarrow \mathcal{Y}$ is Fréchet differentiable, and assume the following hypotheses.*

(H1) *Small residual: There exists a pair $(\alpha^*, x^*) \in \mathcal{P} \times \mathcal{X}$ and a $\rho > 0$ such that*

$$\|G(\alpha^*, x^*)\|_{\mathcal{Y}} \leq \rho .$$

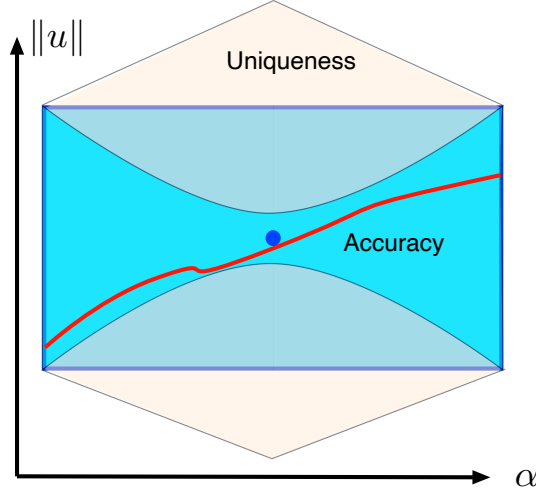


Figure 2.9: A schematic depiction of the constructive implicit function theorem. The theorem guarantees that under appropriate hypothesis, an approximate zero (blue dot) guarantees that within a uniqueness region (orange region) there is a curve in the zero set with a unique point at each fixed α value (red curve), and this curve is located within an accuracy region (blue region). The uniqueness region contains the accuracy region. It is bounded in norm by straight lines, and the accuracy region is bounded in norm by parabolas.

(H2) *Bounded derivative inverse:* There exists a constant $K > 0$ such that

$$\|D_x G(\alpha^*, x^*)^{-1}\|_{\mathcal{L}(\mathcal{Y}, \mathcal{X})} \leq K,$$

where $\|\cdot\|_{\mathcal{L}(\mathcal{Y}, \mathcal{X})}$ denotes the operator norm in $\mathcal{L}(\mathcal{Y}, \mathcal{X})$.

(H3) *Lipschitz bound:* There exist positive real constants L_1, L_2, ℓ_x , as well as $\ell_\alpha \geq 0$ such that for all $(\alpha, x) \in \mathcal{P} \times \mathcal{X}$ with $\|x - x^*\|_{\mathcal{X}} \leq \ell_x$ and $\|\alpha - \alpha^*\|_{\mathcal{P}} \leq \ell_\alpha$ we have

$$\|D_x G(\alpha, x) - D_x G(\alpha^*, x^*)\|_{\mathcal{L}(\mathcal{X}, \mathcal{Y})} \leq L_1 \|x - x^*\|_{\mathcal{X}} + L_2 \|\alpha - \alpha^*\|_{\mathcal{P}} .$$

(H4) *Lipschitz-type bound:* There exist positive real constants L_3 and L_4 , such that for all

parameters $\alpha \in \mathcal{P}$ with $\|\alpha - \alpha^*\|_{\mathcal{P}} \leq \ell_\alpha$ one has

$$\|D_\alpha G(\alpha, x^*)\|_{\mathcal{L}(\mathcal{P}, \mathcal{Y})} \leq L_3 + L_4 \|\alpha - \alpha^*\|_{\mathcal{P}} ,$$

where ℓ_α is the constant that was chosen in (H3).

Finally, suppose that

$$4K^2\rho L_1 < 1 \quad \text{and} \quad 2K\rho < \ell_x . \quad (2.10)$$

Then there exist pairs of constants $(\delta_\alpha, \delta_x)$ with $0 \leq \delta_\alpha \leq \ell_\alpha$ and $0 < \delta_x \leq \ell_x$, as well as

$$2KL_1\delta_x + 2KL_2\delta_\alpha \leq 1 \quad \text{and} \quad 2K\rho + 2KL_3\delta_\alpha + 2KL_4\delta_\alpha^2 \leq \delta_x , \quad (2.11)$$

and for each such pair the following holds. For all $\alpha \in \mathcal{P}$ with $\|\alpha - \alpha^*\|_{\mathcal{P}} \leq \delta_\alpha$ there exists a uniquely determined element $x(\alpha) \in \mathcal{X}$ with $\|x(\alpha) - x^*\|_{\mathcal{X}} \leq \delta_x$ such that $G(\alpha, x(\alpha)) = 0$.

In other words, if we define

$$\mathcal{B}_\delta^{\mathcal{X}} = \{\xi \in \mathcal{X} : \|\xi - x^*\|_{\mathcal{X}} \leq \delta\} \quad \text{and} \quad \mathcal{B}_\delta^{\mathcal{P}} = \{p \in \mathcal{P} : \|p - \alpha^*\|_{\mathcal{P}} \leq \delta\} ,$$

then all points of the solution set of the equation $G(\alpha, x) = 0$ in the product set $\mathcal{B}_{\delta_\alpha}^{\mathcal{P}} \times \mathcal{B}_{\delta_x}^{\mathcal{X}}$ lie on the graph of the function $\alpha \mapsto x(\alpha)$.

In its classical form, the implicit function theorem is one of the central tools of bifurcation theory. Not only can it be used to establish the existence of small solution branches in nonlinear parameter-dependent equations, but by applying it as a tool to modified problems it can frequently be used to provide sufficient conditions for bifurcations. For example, the celebrated Crandall-Rabinowitz result [12] on bifurcation from a simple eigenvalue proves the existence of a bifurcating branch by applying the implicit function theorem to a modification of the original nonlinear problem which removes the trivial solution. The constructive implicit function theorem can similarly be used as a tool for bifurcation analysis, yet in

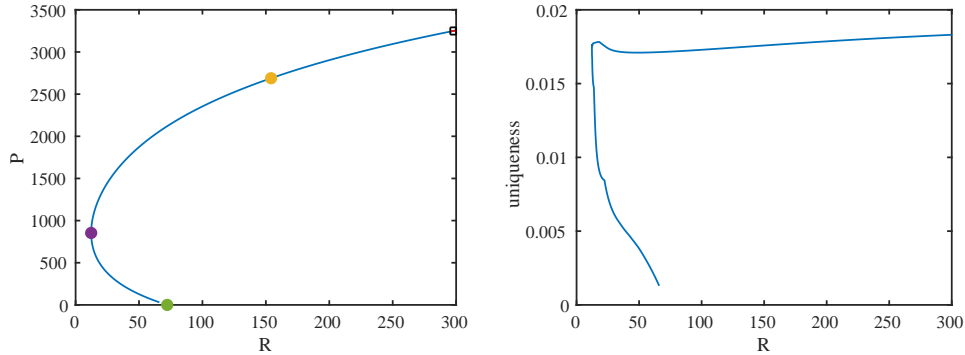


Figure 2.10: Left, the validated bifurcation diagram of polyp density P as a function of the reproductive number R , along with the three validated bifurcation points. The blue curve consists of 5000 continuation steps, corresponding to 5000 linked boxes, for the pre-conditioned map with $\alpha = 0.8 \delta_\alpha$. The initial validated box contains $(R, P) = (300, 3256)$, which is in the upper right corner of the bifurcation diagram, and the last validated box contains $(R, P) = (71.91, 1.493)$, which is close to the green transcritical bifurcation point. For comparison purposes, 4000 continuation steps for the unconditioned map are shown in red within the extremely small square region in the upper right-hand corner. Right, the norm of the uniqueness region of the solution. As the solution gets near the transcritical bifurcation at the origin, the uniqueness region gets smaller. This is expected, since there is no longer any uniqueness when the two branches of the solution curve meet.

a computer-assisted proof setting. In fact, some first applications in this direction have already been provided in [56, 73]. With the current work, we add two more applications.

More precisely, in the following we will be applying Theorem 2.2.1 in two different situations. In the remainder of this section, we apply it for branches of regular points. Through the introduction of a suitable extended system we can reformulate a validated step of pseudo-arc length continuation as an application of the constructive implicit function theorem to this extended system. Combined with suitable linking conditions, this establishes the existence of entire branches covered by slanted boxes.

In addition, in Section 2.3 we use Theorem 2.2.1 to validate bifurcation points. In that setting, and motivated by our earlier work [56], we will apply the theorem to an extended system without any parameter, as the parameter will be incorporated into the function for which we find a root. This parameter-free case means that we no longer need to find the Lipschitz constants relevant to the parameter variations, and we set these unused constants

equal to zero.

2.2.2 Continuation and an extended system

To elaborate further on the validation of regular fixed points, the constructive implicit function theorem as stated in [73] only applies to a single region, validated at a single point. The same paper contains a version of this theorem for slanted boxes, using natural continuation in order to validate a branch of solutions by linking their validation sets to validate a larger portion of the branch. However, natural continuation leaves something to be desired in terms of efficiency. In this section, we develop a method of validation of bifurcation branches using pseudo-arc length continuation which allows for the direct application of the constructive implicit function theorem, and apart from Lipschitz estimates, only requires estimates at a single point in each box. This method is an improvement on the previous natural continuation method in that we can continue at limit points without having to change coordinates. The methods in this section apply for regular orbits along branches. In the next section, we will show how to adapt the constructive implicit function theorem in order to rigorously validate bifurcation points.

Before launching into further technicalities, we describe our results. Applying the pseudo-arc length continuation method to a preconditioned version of the coral model (preconditioning is discussed in Section 2.2.3 below), the resulting rigorously validated curve of fixed points is shown in Figure 2.10. While Figure 2.4 shows a similar picture, the distinction is that those points were found using numerical methods, and though we have a priori error estimates for these methods, we cannot guarantee existence or accuracy. In contrast, the points shown on the new figure are rigorously validated. The depicted points are an accurate indication of existing fixed points of the system, with known and validated accuracy and uniqueness region. In particular, the accuracy of our solutions is known individually for each separate box, and is always less than $1.453 \cdot 10^{-13}$, where the error in $x \in \mathbb{R}^{13}$ is measured in the maximum norm. Figure 2.10 shows the norm of the uniqueness

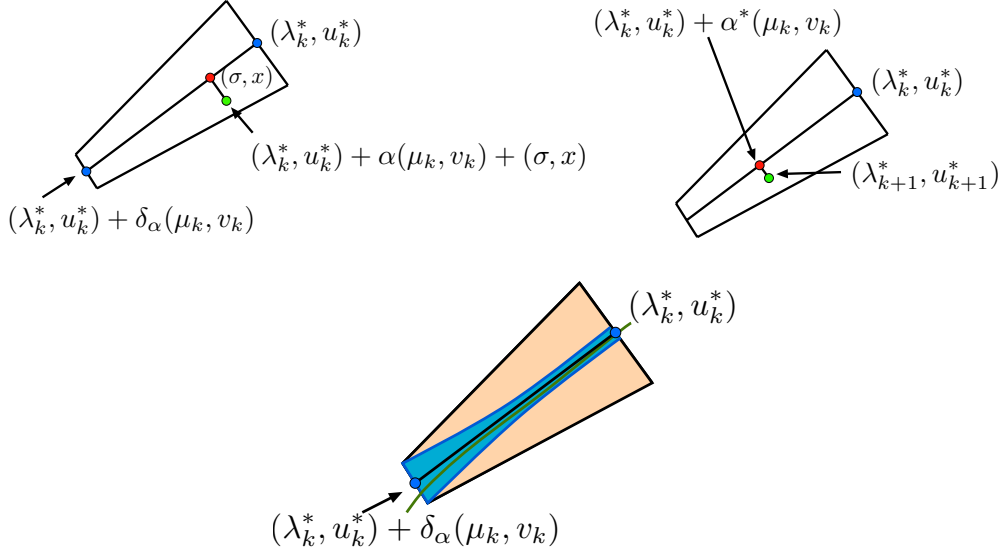


Figure 2.11: A schematic diagram of the the pseudo-arc length continuation method. Top left image: The result guarantees a uniqueness region for the zero set. This takes place in an adapted coordinate system, meaning that the box is slanted, but the uniqueness region is still bounded by straight lines. Since we only continue the curve in one direction, this figure only depicts the left half of the uniqueness region. The center line segment of this region is given by $(\lambda_k^*, u_k^*) + \alpha(\mu_k, v_k)$ for $0 \leq \alpha \leq \delta_\alpha$. At a fixed α value, we use Newton's method to find the next approximate zero along the line $(\lambda_k^*, u_k^*) + \alpha(\mu_k, v_k) + (\sigma, x)$, where (σ, x) denotes the vector pointing from $(\lambda_k^*, u_k^*) + \alpha(\mu_k, v_k)$ to the point $(\lambda_k^*, u_k^*) + \alpha(\mu_k, v_k) + (\sigma, x)$, and which is orthogonal to (μ_k, v_k) . Top right image: After we fixed the value $\alpha = \alpha^*$, we label this next approximation $(\lambda_{k+1}^*, u_{k+1}^*)$. Bottom image: Inside the uniqueness region (orange) is an accuracy region (blue). The accuracy region is bounded by curves which are parabolic in norm in the adapted coordinate system.

for each separate box. The uniqueness shrinks when the curve approaches zero. This is not surprising, since $x = 0$ is part of the zero set, putting a barrier on the size of the uniqueness region.

We now proceed with the constructive implicit function theorem for a validated pseudo-arc length continuation. In each continuation step we use continuation in a box with slanted sides, where the predictor step is performed along the middle of the box in the direction a specified vector (μ, v) (usually the estimated tangent to the zero set curve), and the corrector step uses a computation such as Newton's method to refine the estimate. This

refinement is performed in a direction orthogonal to the predictor direction (μ, v) . This is depicted in Figure 2.11. The left-hand image is a schematic diagram showing the box with its midline between two blue dots. The midline is the estimated tangent line in the direction (μ, v) . Our validation gives us a maximum length of the box for which we can guarantee accuracy and uniqueness of the solution. The predictor, shown with a red dot, must be chosen inside that box. The corrector, shown with a green dot is along an orthogonal line to the midline. The right-hand image shows the accuracy region in blue and the uniqueness region in orange. Note that the uniqueness region has large width near the starting point, and the accuracy region grows towards the ending point. In Figure 2.11, the uniqueness region for the box is approximately diamond shaped, whereas in Figure 2.12, the box is not only slanted but also has a uniqueness region which is asymmetric, more of a half-diamond. The half-diamond shape is in fact only half of the uniqueness box. In particular, as we are merely continuing in one direction, which in Figure 2.12 is to the left, we only show one side of the uniqueness box. The fact that we could continue to the right as well is not relevant for our continuation.

We now turn to the technical details of this approach. For this, we consider $F : \mathbb{R} \times U \rightarrow U$, where U denotes an arbitrary Euclidean space. Our goal is to implement pseudo-arclength continuation based on Theorem 2.2.1 to find branches of zeros of the nonlinear function F . For the specific application of this work, we will consider $U = \mathbb{R}^{13}$ and $F(\lambda, x) = f(\lambda, x) - x$, where f is the coral model. Nevertheless, we use the more general notation based on F to indicate that these methods are general. In fact, the methods readily generalize to the Banach space setting as well. However, in this work for convenience of notation we only consider the Euclidean space case. For any $(\lambda_0, u_0) \in \mathbb{R} \times U$, an approximate zero of F , and for a fixed direction vector $(\mu_0, v_0) \in \mathbb{R} \times U$, define $G : \mathbb{R} \times (\mathbb{R} \times U) \rightarrow \mathbb{R} \times U$ as follows

$$G(\alpha, (\sigma, x)) = \begin{pmatrix} \mu_0\sigma + v_0^t x \\ F(\lambda_0 + \alpha\mu_0 + \sigma, u_0 + \alpha v_0 + x) \end{pmatrix}. \quad (2.12)$$

The zeros of G as the parameter α varies correspond to the pseudo-arc length continuation solutions of F for a single continuation box. The first component of the function G guarantees that the pair (σ, x) is orthogonal to the direction (μ_0, v_0) . As we will show in the next subsection, one can apply the constructive implicit function theorem from [73] directly to the extended function G and thereby perform rigorously validated pseudo-arc length continuation.

Since we will need them later, we close this subsection by explicitly stating the derivatives of G with respect to both the variables (σ, x) and with respect to the parameter α . These are respectively given by

$$D_{(\sigma,x)}G(\alpha, (\sigma, x)) = \begin{pmatrix} A_{11} & A_{12} \\ A_{21} & A_{22} \end{pmatrix}, \quad (2.13)$$

where

$$\begin{aligned} A_{11} &= \mu_0, & A_{12} &= v_0^t, \\ A_{21} &= D_\lambda F(\lambda_0 + \alpha\mu_0 + \sigma, u_0 + \alpha v_0 + x), \\ A_{22} &= D_u F(\lambda_0 + \alpha\mu_0 + \sigma, u_0 + \alpha v_0 + x), \end{aligned} \quad (2.14)$$

as well as

$$D_\alpha G(\alpha, (\sigma, x)) = \begin{pmatrix} B_1 \\ B_2 \end{pmatrix}, \quad (2.15)$$

where

$$\begin{aligned}
B_1 &= 0, \\
B_2 &= D_\lambda F(\lambda_0 + \alpha\mu_0 + \sigma, u_0 + \alpha v_0 + x)\mu_0 \\
&\quad + D_u F(\lambda_0 + \alpha\mu_0 + \sigma, u_0 + \alpha v_0 + x)v_0
\end{aligned} \tag{2.16}$$

Pseudo-arc length validation theorem

We are now in a position to start establishing assumptions under which we can validate a branch in the zero set of F using pseudo-arc length continuation. For this we need the following modified set of assumptions. For the purposes of this work, we use the vector norm $\|(\alpha, x)\| = \max\{|\alpha|, \|x\|_U\}$ for all $(\alpha, x) \in \mathbb{R} \times U$, even though this could easily be modified.

(P1) We assume both

$$\|F(\lambda_0, u_0)\|_U \leq \rho \quad \text{and} \quad \|D_\lambda F(\lambda_0, u_0)\mu_0 + D_u F(\lambda_0, u_0)v_0\|_U \leq \xi. \tag{2.17}$$

(P2) Assume that there exists an explicit constant $K > 0$ which is a bound on the operator norm of the inverse of the matrix

$$D_{(\sigma, x)} G(0, (0, 0)) = \begin{pmatrix} \mu_0 & v_0^t \\ D_\lambda F(\lambda_0, u_0) & D_u F(\lambda_0, u_0) \end{pmatrix},$$

i.e., we suppose that

$$\|D_{(\sigma, x)} G(0, (0, 0))^{-1}\|_{\mathcal{L}(\mathbb{R} \times U, \mathbb{R} \times U)} \leq K.$$

For this, we interpret the matrix as a linear map on the product space $\mathbb{R} \times U$, and

the operator norm is the norm in $\mathcal{L}(\mathbb{R} \times U, \mathbb{R} \times U)$.

(P3) Let M_1, M_2, M_3 , and M_4 be Lipschitz constants such that for all pairs (λ, u) which satisfy $\|u - u_0\| \leq d_u$ and $|\lambda - \lambda_0| \leq d_\lambda$ we have the estimates

$$\|D_u F(\lambda, u) - D_u F(\lambda_0, u_0)\|_{\mathcal{L}(U, U)} \leq M_1 \|u - u_0\|_U + M_2 |\lambda - \lambda_0| ,$$

$$\|D_\lambda F(\lambda, u) - D_\lambda F(\lambda_0, u_0)\|_{\mathcal{L}(\mathbb{R}, U)} \leq M_3 \|u - u_0\|_U + M_4 |\lambda - \lambda_0| ,$$

where as usual we will identify the norm in $\mathcal{L}(\mathbb{R}, U)$ with the norm $\|\cdot\|_U$ in the following.

We would like to point out that all of the above three conditions are formulated in terms of the nonlinear parameter-dependent function F and an approximate solution (λ_0, u_0) of the equation $F(\lambda, u) = 0$.

We now turn our attention to the extended system described by the operator G introduced in (2.12). It turns out that the above three assumptions are tailor-made to establish the hypotheses (H1) through (H4) from the constructive implicit function theorem for the mapping G . One can easily see that (P1) implies

$$\|G(0, (0, 0))\|_{\mathbb{R} \times U} \leq \rho ,$$

i.e., hypothesis (H1) is satisfied. Furthermore, using the explicit derivative formulas from the end of the last subsection, the assumption (P2) immediately yields the estimate

$$\|D_{(\sigma, x)} G(0, (0, 0))\|_{\mathcal{L}(\mathbb{R} \times U, \mathbb{R} \times U)} \leq K ,$$

which establishes (H2). It remains to show that (P3) furnishes the estimates in (H3)

and (H4). For this, let ξ be defined as in (2.17), and define the four constants

$$\begin{aligned} L_1 &= \max(M_1 + M_3, M_2 + M_4), \\ L_2 &= (M_1 + M_3)\|v_0\|_U + (M_2 + M_4)|\mu_0|, \\ L_3 &= \xi, \\ L_4 &= (M_1\|v_0\|_U + M_2|\mu_0|)\|v_0\|_U + (M_3\|v_0\|_U + M_4|\mu_0|)|\mu_0|. \end{aligned}$$

Then the constants L_1 through L_4 are the Lipschitz constants for the extended function G as required by (H3) and (H4). For this, first note that in view of (2.13) and (2.14) we have

$$D_{(\sigma,x)}G(\alpha, (\sigma, x)) - D_{(\sigma,x)}G(0, (0, 0)) = \begin{pmatrix} 0 & 0 \\ D_\lambda F(w_1) - D_\lambda F(w_2) & D_u F(w_1) - D_u F(w_2) \end{pmatrix},$$

where $D_\lambda F$ and $D_u F$ are evaluated at $w_1 = (\lambda_0 + \alpha\mu_0 + \sigma, u_0 + \alpha v_0 + x)$ and $w_2 = (\lambda_0, u_0)$.

Then one can readily see that (H3) follows from (P3) and the estimates

$$\begin{aligned}
& \|D_{(\sigma,x)}G(\alpha, (\sigma, x)) - D_{(\sigma,x)}G(0, (0, 0))\|_{\mathcal{L}(\mathbb{R} \times U, \mathbb{R} \times U)} \\
& \leq \|D_uF(\lambda_0 + \alpha\mu_0 + \sigma, u_0 + \alpha v_0 + x) - D_uF(\lambda_0, u_0)\|_{\mathcal{L}(U, U)} \\
& \quad + \|D_\lambda F(\lambda_0 + \alpha\mu_0 + \sigma, u_0 + \alpha v_0 + x) - D_\lambda F(\lambda_0, u_0)\|_{\mathcal{L}(\mathbb{R}, U)} \\
& \leq M_1(|\alpha|\|v_0\|_U + \|x\|_U) + M_2(|\alpha|\|\mu_0\| + |\sigma|) \\
& \quad + M_3(|\alpha|\|v_0\|_U + \|x\|_U) + M_4(|\alpha|\|\mu_0\| + |\sigma|) \\
& = (M_1 + M_3)\|x\|_U + (M_2 + M_4)|\sigma| \\
& \quad + ((M_1 + M_3)\|v_0\|_U + (M_2 + M_4)|\mu_0|)|\alpha| \\
& = L_1\|(\sigma, x)\|_{\mathbb{R} \times U} + L_2|\alpha|.
\end{aligned}$$

Similarly, using (2.15) and (2.16) one can show that (H4) follows from (P1) and (P3), in combination with the inequalities

$$\begin{aligned}
& \|D_\alpha G(\alpha, (0, 0))\|_{\mathcal{L}(\mathbb{R}, \mathbb{R} \times U)} \\
& \leq \|D_\lambda F(\lambda_0, u_0)\mu_0 + D_uF(\lambda_0, u_0)v_0\|_U \\
& \quad + \|D_uF(\lambda_0 + \alpha\mu_0, u_0 + \alpha v_0)v_0 - D_uF(\lambda_0, u_0)v_0\|_U \\
& \quad + \|D_\lambda F(\lambda_0 + \alpha\mu_0, u_0 + \alpha v_0)\mu_0 - D_\lambda F(\lambda_0, u_0)\mu_0\|_U \\
& \leq \xi + (M_1\|v_0\|_U + M_2|\mu_0|)|\alpha|\|v_0\|_U \\
& \quad + (M_3\|v_0\|_U + M_4|\mu_0|)|\alpha|\|\mu_0\| \\
& = L_3 + L_4|\alpha|.
\end{aligned}$$

Altogether, these estimates lead to the following result.

Theorem 2.2.2 (Pseudo-arclength continuation for a branch segment). *Consider the fixed pairs (u_0, λ_0) and (v_0, μ_0) in $\mathbb{R} \times U$, let d_λ and d_u be two positive constants, and suppose that our hypotheses (P1), (P2), and (P3) are satisfied. Moreover, assume that both*

$$4K^2\rho < 1 \quad \text{and} \quad 2K\rho < d_u$$

hold. Then we can choose constants

$$0 < \delta_\alpha \leq d_\lambda, \quad 0 < \delta_u \leq d_u, \quad \text{where} \quad \delta_\alpha \|(\mu_0, v_0)\| + \delta_u \leq \min(d_u, d_\lambda),$$

and such that

$$2KL_1\delta_u + 2KL_2\delta_\alpha \leq 1 \quad \text{and} \quad 2K\rho + 2KL_3\delta_\alpha + 2KL_4\delta_\alpha^2 \leq \delta_u.$$

Then for every $\alpha \leq \delta_\alpha$ there exists a unique (σ, x) in the zero set of G with $\|(\sigma, x)\| \leq \delta_u$.

These statements guarantee that there is a unique element of the zero set of F which lies on the hyperplane orthogonal to the center line in the slanted box between (λ_0, u_0) and $(\lambda_0 + \delta_\alpha\mu_0, u_0 + \delta_\alpha v_0)$ and passes through the point $(\lambda_0 + \alpha\mu_0, u_0 + \alpha v_0)$. This unique zero is given by $(\lambda_0 + \alpha\mu_0, u_0 + \alpha v_0) + (\sigma, x)$. Additionally, let

$$\delta_{\min} = 2K\rho.$$

Then for $\alpha = 0$ we can guarantee that the resulting pair in the zero of G is accurate within δ_{\min} of (λ_0, u_0) , and this zero is unique within the set $\|(\sigma, x)\| \leq \min\{(2KL_1)^{-1}, d_u, d_\alpha\}$.

Proof. To show the theorem we follow the proof of [73, Theorem 5]. Aside from the changes in the Lipschitz constants which have already been derived before the formulation of the theorem, the only changes to the cited proof are due to the fact that for a fixed parameter of G , the values of both the parameter λ and the phase space value x of F can vary. Therefore, in order to guarantee that the Lipschitz estimates on F hold, we need to assure

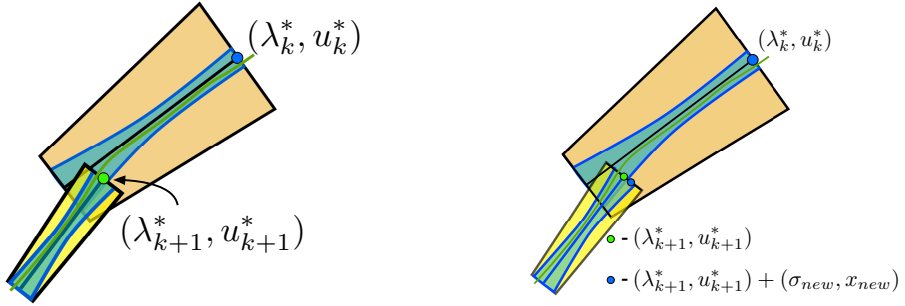


Figure 2.12: Left image: Associated with each successive approximation, there is a uniqueness region and an accuracy region. Right image: In order to guarantee that the k -th and $(k + 1)$ -st region enclose the same component of the zero set (the green curve), we must verify the linking condition. This requires that the accuracy curve of the $(k + 1)$ -st box at $\alpha = 0$ (such as the blue point on the upper edge of the $(k + 1)$ -st blue box) is contained in the uniqueness region of the k -th box (orange region).

that for every $\alpha \leq \delta_\alpha$ and all $\|(\sigma, x)\| \leq \delta_u$ the norm $\|\alpha(\mu_0, v_0) + (\sigma, x)\|$ is bounded by both d_u and d_λ . This immediately leads to the additional constraints in the formulation of the theorem. \square

The above theorem gives a method for validating a branch segment of the zero set within a single slanted box. In practice we use this result successively to validate a whole solution branch. For each pair (λ_k^*, u_k^*) , and for the approximate tangent (μ_k, v_k) , we then define an extended function G_k , and validate a branch segment for F within the k -th box. For a fixed parameter value $\alpha_k \leq \delta_\alpha$, we then use Newton's method to find an approximate zero of F which is orthogonal to (μ_k, v_k) , i.e., which is a zero of G_k . We abbreviate this approximate zero as $(\lambda_{k+1}^*, u_{k+1}^*)$, and can now repeat the entire process for the $(k + 1)$ -st branch segment, see also Figure 2.12. What remains to be shown is that the successive validated boxes are linked, meaning that the branch segment in the k -th box and the branch segment in the $(k + 1)$ -st box are on the same branch. That is, the accuracy region of the $(k + 1)$ -st box has to be contained within the uniqueness region of the k -th box at the point α_k where we made the numerical estimate. We give the linking condition for two boxes in the next theorem.

Theorem 2.2.3 (Linking branch segments). *Let $\delta_{k+1,\min} = 2K_{k+1}\rho_{k+1}$ be the accuracy of the solution*

$$(\lambda_{k+1}^*, u_{k+1}^*) = (\lambda_k^* + \alpha_k \mu_k + \sigma^*, u_k^* + \alpha_k v_k + x^*) .$$

In order to guarantee that the two validated boxes are linked, we require the estimates

$$|\alpha_k| + \frac{\delta_{k+1,\min}}{\|(\mu_k, v_k)\|} < \delta_{k,\alpha} \quad \text{and} \quad |(\sigma^*, x^*)| + \delta_{k+1,\min} < \delta_{k,u} .$$

Proof. The accuracy of the $(k+1)$ -st solution at $\alpha = 0$ is given by $\delta_{k+1,\min}$. That is, there exists a unique exact solution to $F = 0$ of the form

$$(\tilde{\lambda}, \tilde{u}) = (\lambda_{k+1}^* + \sigma_{new}, u_{k+1}^* + x_{new}) ,$$

where $\|(\sigma_{new}, x_{new})\| < \delta_{k+1,\min}$. In order to derive our linking condition we need to establish that this solution is contained in the uniqueness region of the k -th segment. We can therefore write

$$(\tilde{\lambda}, \tilde{u}) - (\lambda_k^*, u_k^*) = (\alpha_k + \alpha^*)(\mu_k, v_k) + (\sigma^* + \sigma^+, x^* + x^+) ,$$

where $(\sigma_{new}, x_{new}) = \alpha^+(\mu_k, v_k) + (\sigma^+, x^+)$, and (μ_k, v_k) is orthogonal to the vector (σ^+, x^+) .

Thus we have

$$\|\alpha^+(\mu_k, v_k) + (\sigma^+, x^+)\| < \delta_{k+1,\min} .$$

By the orthogonality of the two vectors, both the estimate $|\alpha^+| \|(\mu_k, v_k)\| < \delta_{k+1,\min}$ and the estimate $\|(\sigma^+, x^+)\| < \delta_{k+1,\min}$ are satisfied. In order to satisfy the linking condition, we have to require that both $|\alpha_k + \alpha^+| < \delta_{k,\alpha}$ and $\|(\sigma^* + \sigma^+, x^* + x^+)\| < \delta_{k,u}$ hold. This translates into the conditions

$$|\alpha_k + \alpha^+| \leq |\alpha_k| + \frac{\delta_{k+1,\min}}{\|(\mu_k, v_k)\|} < \delta_{k,\alpha} ,$$

as well as

$$\|(\sigma^* + \sigma^+, x^* + x^+)\| \leq \|(\sigma^*, x^*)\| + \delta_{k+1,\min} < \delta_{k,u} .$$

This completes the proof of the theorem. \square

2.2.3 Preconditioning the coral map

If we use the above method on the coral system, it is extremely slow to produce the bifurcation diagram. This is due to the different relative sizes of the components of the population and the parameter. We are able to significantly speed up the method by using preconditioning. In particular, for $k = 1, \dots, d$ let

$$\tilde{f}_k(\tilde{R}, \tilde{u}) = \frac{f_k(100\tilde{R}, (s_1\tilde{u}_1, \dots, s_d\tilde{u}_d))}{s_k} ,$$

where s_1, \dots, s_d are empirically determined positive scale constants. Then it is clear that if we write $(R, u) = (100\tilde{R}, (s_1\tilde{u}_1, \dots, s_d\tilde{u}_d))$, then (R, u) is a fixed point of f if and only if (\tilde{R}, \tilde{u}) is a fixed point of the preconditioned map \tilde{f} . However, the map \tilde{f} is better scaled in the sense that we expect all components and the parameter to be of the same order of magnitude. Therefore the pseudo-arc length continuation can be performed more efficiently. In particular, we find that the size of δ_α in the preconditioned version is (in comparable coordinates) around two orders of magnitude larger than those for the system without modification. This means that we are able to validate a much larger portion of the bifurcation diagram with the same number of continuation steps. Figure 2.10 shows 5000 continuation steps for the preconditioned case starting at $R = 300$ in the upper right corner, shown in blue. For comparison purposes, 4000 continuation steps are shown in red for the unmodified case. The bifurcation curve goes through a limit point and almost to $\|u\| = 0$ for the preconditioned case, but is hardly even a visible piece of red curve for the original unmodified map. A similar preconditioning is performed in the case of the

bifurcation points, as described in the next section.

2.3 Validation of the bifurcation points

In this section, we discuss the validation of the bifurcation points. Namely, we have used a computer-assisted proof to validate the Neimark-Sacker bifurcation point, where the invariant circles form in Section 2.3.1 and the saddle-node bifurcation point in Section 2.3.2. In each case, to do so we create an extended system H such that $H = 0$ guarantees the needed conditions for a bifurcation point. We then apply the constructive implicit function theorem to H . In both cases, we use interval arithmetic for a separate computational validation of the extra transversality and nondegeneracy conditions. We also prove that there is a transcritical bifurcation point on the extinction axis. However, this last case does not require a computer-assisted proof for validation, since the calculations are simple enough for a closed form calculation.

2.3.1 Validation of the Neimark-Sacker bifurcation point

In Sections 2.1.4 and 2.1.5, we observed that at $(R, P) \approx (154.1, 2689)$, there is a change in stability of the fixed points, and for $R > 154.1$, typical initial conditions converge to populations which are oscillating in time. This is the behavior associated with a Neimark-Sacker bifurcation. In this section we detail the process of rigorous validation of the Neimark-Sacker bifurcation point seen in the upper right corner of Figure 2.4. While this is the first time that a rigorous validation of a Neimark-Sacker bifurcation has been performed in this way, rigorous validation of Hopf bifurcations was performed in [84] in the context of ordinary and partial differential equations, but using a quite different method. Rather than considering conditions along a curve of fixed points or equilibria, instead the method used a validated continuation of periodic orbits with a renormalization technique, validating that there was a bifurcation of equilibria at the turning point of this invariant closed curve of solutions. Moreover, computer-assisted proofs were used in [10] to rigorously establish an

invariant circle in a two-dimensional map, which is created via a Neimark-Sacker bifurcation. They do not, however, establish the bifurcation point itself directly. While it would be interesting to adapt their method to the coral model, this lies beyond the scope of the current work.

We now proceed with our validation of the Neimark-Sacker bifurcation. As a first step, we state the standard theoretical Neimark-Sacker bifurcation theorem found in a bifurcation theory textbook. We then show how to adapt this classical result to create a rigorous computer-assisted bifurcation theorem.

Theorem 2.3.1 (Neimark-Sacker bifurcation point). *There is a Neimark-Sacker bifurcation for the coral system in (2.4) and (2.5) for the basic reproduction number $R_* \approx 154.1$ and with polyp population density $P_* \approx 2689$. The precise error bounds are stated in Table 2.2.*

The remainder of this subsection is devoted to the proof of this theorem. Our approach is to verify the classical conditions for a *Neimark-Sacker bifurcation*, as described for example in [50] — and which we briefly review in the following. Consider a smooth map $f : \mathbb{R} \times \mathbb{R}^d \rightarrow \mathbb{R}^d$. Furthermore, we begin by assuming the following two conditions:

- (a) *Existence of a fixed point:* The map f has a fixed point at a specific parameter value, i.e., we assume that $f(\lambda_0, x_0) = x_0$.
- (b) *Pair of imaginary eigenvalues on the unit circle:* The Jacobian matrix $D_x f(\lambda_0, x_0)$ has exactly one simple conjugate pair of imaginary eigenvalues on the unit circle. We denote these eigenvalues by $e^{\pm i\theta_0}$, for some angle $0 < \theta_0 < \pi$.

These two conditions have to be supplemented by another three transversality and nondegeneracy conditions, which will be stated in detail below. For this, however, we first need to introduce some additional notation.

Due to the implicit function theorem, as long as the Jacobian matrix in (b) does not have the eigenvalue 1, there exists a smooth curve of locally unique fixed points, which we

denote by $(\lambda, x_0(\lambda))$. Moreover, we define

$$A(\lambda) = D_x f(\lambda, x_0(\lambda)) .$$

We would like to point out that in our application to the coral system, the rigorously established existence of the branch of fixed points as a side effect also implies that along the branch near the Neimark-Sacker point, the Jacobian matrix never has an eigenvalue 1.

Now let $p \in \mathbb{C}^d$ and $q \in \mathbb{C}^d$ denote the right eigenvectors of $A(\lambda_0)$ corresponding to $e^{i\theta_0}$ and $e^{-i\theta_0}$, respectively, and normalized in such a way that $\langle p, q \rangle = 1$, where the bracket notation denotes the usual complex scalar product $\langle p, q \rangle := \bar{p}^t q$. Finally, by Taylor's formula we can expand the function f in the form

$$f(\lambda_0, x) - x_0 = A(\lambda_0)x + \frac{1}{2}B(x, x) + \frac{1}{6}C(x, x, x) + O(\|x\|^4) , \quad (2.18)$$

where B and C denote the second- and third-order derivative terms at the point (λ_0, x_0) in the form

$$B_i(y, z) = \sum_{j,k=1}^d \frac{\partial^2 f}{\partial x_j \partial x_k}(\lambda_0, x_0) y_j z_k$$

and

$$C_i(y, z, w) = \sum_{j,k,l=1}^d \frac{\partial^3 f}{\partial x_j \partial x_k \partial x_l}(\lambda_0, x_0) y_j z_k w_l .$$

After these preparations, we can now complete our description of the conditions needed for the Neimark-Sacker theorem:

(c) *Transversality condition:* Using the notation above, suppose that

$$\operatorname{Re} \left(e^{-i\theta_0} \left\langle p, \frac{dA}{d\lambda}(\lambda_0)q \right\rangle \right) \neq 0 .$$

(d) *Nondegeneracy condition I:* Suppose that

$$\theta_0 \neq \frac{\pi}{2} \quad \text{and} \quad \theta_0 \neq \frac{2\pi}{3}.$$

(e) *Nondegeneracy condition II:* Suppose that

$$\begin{aligned} Re (e^{-i\theta_0} (\langle p, C(q, q, \bar{q}) \rangle + 2\langle p, B(q, (I - A)^{-1}B(q, \bar{q})) \rangle \\ + \langle p, B(\bar{q}, (e^{2i\theta_0} I - A)^{-1}B(q, q)) \rangle)) \neq 0. \end{aligned}$$

To summarize, the transversality condition implies that the pair of complex conjugate eigenvalues at λ_0 crosses the imaginary axis with nonzero speed. The first nondegeneracy condition indicates that the eigenvalues $e^{\pm i\theta_0}$ are not k -th roots of unity for $k = 1, \dots, 4$. Since the proof of the Neimark-Sacker theorem is based on the Poincaré normal form theorem, this condition excludes resonances. Finally, the left-hand side of the second nondegeneracy condition gives the coefficient of the cubic term in the complex Poincaré normal form, and its sign distinguishes between a sub- and super-critical Neimark-Sacker bifurcation. For more details we refer the reader to the part of [50, Section 5.4] devoted to the Neimark-Sacker bifurcation.

Under the above conditions, the Neimark-Sacker theorem guarantees that a locally unique invariant closed curve bifurcates from the set of fixed points at the point (λ_0, x_0) . As already mentioned, the type of bifurcation depends on the sign of the left-hand side of (e).

In order to create the validation version of this theorem, we use a suitable extended system to validate assumptions (a) and (b). After having established an existence and uniqueness result for this extended system, one can then validate conditions (c), (d), and (e) separately using interval arithmetic. For convenience, we have converted the complex system into the following real system of equations. We are seeking zeros of the function $H_{ns} : \mathbb{R}^m \rightarrow$

R	λ	x_1	P
154.1	5.286	1794	2689
δ_1	δ_2	ρ	K
$1.473 \cdot 10^{-10}$	$1.220 \cdot 10^{-8}$	$6.166 \cdot 10^{-11}$	1.000
L_1	(c)	(d)	(e)
$4.097 \cdot 10^7$	$4.338 \cdot 10^{-2}$	46.85	$-1.21 \cdot 10^{-6}$

Table 2.2: Validation constants for the system (2.19) at the Neimark-Sacker bifurcation point. All values are written with four decimal places, unless less accuracy is known. For more efficient computation, we multiplied by a preconditioning matrix and determined the bounds ρ , K , and L_1 . We selected a matrix close to the Jacobian matrix of H_{ns} , whose inverse was used as a preconditioner. The accuracy constant δ_1 and the isolation bound δ_2 were derived using ρ , K and L_1 . For the three conditions (c), (d), and (e), which were checked separately after the validation involving H_{ns} , we used an interval arithmetic enclosure of the approximate solution with radius δ_1 . Note that the angle in (d) is given in degrees.

\mathbb{R}^m , which is defined as

$$H_{ns}(x, \lambda, w, u, a, b) = \begin{pmatrix} f(\lambda, x) - x \\ D_x f(\lambda, x)w - aw + bu \\ D_x f(\lambda, x)u - bw - au \\ a^2 + b^2 - 1 \\ \|w\|^2 - 1 \\ \|u\|^2 - 1 \end{pmatrix}. \quad (2.19)$$

The first equation in the system is the fixed point condition. The second through fourth equations form the simple complex eigenvalue pair condition, where we write $e^{\pm i\theta_0} = a \pm ib$, and the eigenvectors p and q are given by $u \pm iw$, up to normalization. The last two equations are included to single out a locally unique eigenvector.

For a function of the form $f : \mathbb{R} \times \mathbb{R}^d \rightarrow \mathbb{R}^d$, we have $x \in \mathbb{R}^d$, $\lambda \in \mathbb{R}$, $u, w \in \mathbb{R}^d$, as well as $a, b \in \mathbb{R}$. Therefore, the extended system $H_{ns} : \mathbb{R}^m \rightarrow \mathbb{R}^m$ lives in dimension $m = 3d + 3$.

In our numerical validation, we are working with a 13-dimensional system, implying that this extended system has dimension 42.

Using standard numerical methods, we obtained an approximate bifurcation point satisfying $H_{ns}(x, \lambda, w, u, a, b) = 0$, for the function H_{ns} in (2.19), and with values for R, λ, x_1 , and P as stated in Table 2.2. Since H_{ns} is parameter free, we only seek rigorous solutions of the extended system in (2.19) which satisfy $H_{ns} = 0$ in \mathbb{R}^{42} . Thus we only need to verify the hypotheses of the constructive implicit function theorem which involve the values of ρ , K , L_1 , and $\ell_x > 0$ at our computed approximation point. See also Theorem 2.2.1. Table 2.2 summarizes the constants found for the validation of the solution of system (2.19).

We obtain the bounds ρ and K by using interval arithmetic. While the bound ρ can be found in a straightforward way, the constant K cannot easily be found by using interval arithmetic to compute matrix inverses. Therefore, we first compute an approximate numerical inverse. However, we still need a bound on the exact inverse, and a bound on the accuracy of the approximate inverse. This is required in both the computation of K and twice when we verify condition (e). The required quantities can be determined using the following lemma. While we apply this lemma only for matrices, it is stated for the case of Banach spaces.

Lemma 2.3.2 (Inverse bounds). *Let A be a bounded linear operator between two Banach spaces, and let B be an approximate inverse of A . Assume further that*

$$\|I - BA\| \leq \rho_1 < 1 \quad \text{as well as} \quad \|B\| \leq \rho_2 .$$

Then A is one-to-one, onto, and we have both

$$\|A^{-1}\| \leq \frac{\rho_2}{1 - \rho_1} \quad \text{and} \quad \|B - A^{-1}\| \leq \frac{\rho_1 \rho_2}{1 - \rho_1} .$$

The bound on A^{-1} is due to a Neumann series argument, and the proof can be found in [73]. In addition, the second bound is a consequence of $\|B - A^{-1}\| \leq \|I - BA\| \|A^{-1}\|$.

Having described how the constants ρ and K can be estimated rigorously, we now turn our attention to the Lipschitz constant L_1 . It can be determined using the mean value theorem for multivariate functions from the calculations in (2.20) below. For this, suppose that the function $H_{ns} : \mathbb{R}^m \rightarrow \mathbb{R}^m$ is differentiable and let $h_{ij}(x) = (\partial(H_{ns})_i / \partial x_j)(x)$. Then $h_{ij} : \mathbb{R}^m \rightarrow \mathbb{R}$, and we let $h : \mathbb{R}^m \rightarrow \mathbb{R}^{m \times m}$ denote the matrix-valued function with entries h_{ij} . Throughout our computations, we used the maximum norms for vectors x , and the induced matrix norm for matrices A . Recall that one then has $\|x\| = \|x\|_\infty = \max_{i=1,\dots,m} |x_i|$, as well as $\|A\| = \|A\|_\infty = \max_{i=1,\dots,m} \sum_{j=1}^m |A_{ij}|$. After these preparations, the mean value theorem implies

$$|h_{ij}(x) - h_{ij}(y)| \leq \max_{c \in D} \|\nabla h_{ij}(c)\|_1 \|x - y\|,$$

where D denotes the line segment between the points x and y . Together with the definition of the functions h_{ij} one further obtains

$$\begin{aligned} |h_{ij}(x) - h_{ij}(y)| &\leq \max_{c \in D} \left\| \left(\frac{\partial^2 (H_{ns})_i}{\partial x_1 \partial x_j}(c), \dots, \frac{\partial^2 (H_{ns})_i}{\partial x_n \partial x_j}(c) \right) \right\|_1 \|x - y\| \\ &\leq m \max_{c \in D, k=1,\dots,m} \left| \frac{\partial^2 (H_{ns})_i}{\partial x_k \partial x_j}(c) \right| \|x - y\|. \end{aligned}$$

This finally furnishes

$$\begin{aligned} \|h(x) - h(y)\| &= \max_{i=1,\dots,m} \sum_{j=1}^m |h_{ij}(x) - h_{ij}(y)| \\ &\leq \max_{i=1,\dots,m} \sum_{j=1}^m \left(m \max_{c \in D, k=1,\dots,m} \left| \frac{\partial^2 (H_{ns})_i}{\partial x_k \partial x_j}(c) \right| \right) \|x - y\|. \end{aligned} \quad (2.20)$$

The factor in front of $\|x - y\|$ on the right-hand side is then the Lipschitz constant L_1 , and

it can be determined via interval arithmetic and automatic differentiation.

Altogether, our rigorous computer-assisted proof of Theorem 2.3.1 can be summarized as follows. After completing the validation of the conditions that guarantee that the constructive implicit function theorem holds, we are able to verify the accuracy and uniqueness regions for the bifurcation point. In addition, we can use Intlab [69] to rigorously show that the Jacobian matrix $D_x f(\lambda_0, u_0)$ has in fact only two eigenvalues on the unit circle, by verifying that the remaining eleven eigenvalues all lie inside the unit disk. This implies that a bifurcation occurs within the specified error of the approximate bifurcation point. We then verify that this bifurcation is indeed a Neimark-Sacker bifurcation by showing that conditions (c), (d), and (e) hold using interval arithmetic on these conditions. Here are a few remarks which give a more detailed explanation:

- For each condition, we show that the interval containing the exact answer does not contain zero for (c) and (e), and does not contain any of the avoided angles for (d).
- While we are able to work with real-valued quantities a, b, u, v in the initial calculations of parts (a) and (b), we must switch to the complex case to verify the extra conditions (c), (d), (e), and we normalize the complex vectors p and q using the normalization condition $\langle p, q \rangle = 1$.
- We need to be able to guarantee that all three conditions are satisfied for the entire accuracy region. Therefore we evaluate these conditions on an interval vector whose midpoint is the approximate bifurcation point, and whose radius is δ_1 . That is, every component of the vector is an interval. The actual computed values of the conditions (c)-(e) are intervals, but the values given in Table 2.2 are the worst-case scenario values. Even with the interval calculations, conditions (c) and (d) are known to more than four significant digits, but condition (e) is only known to three digits of accuracy.

This completes the proof of Theorem 2.3.1.

R	λ	x_1	P	δ_1	δ_2
12.28	0.4213	569.5	853.4	$3.306 \cdot 10^{-12}$	$4.015 \cdot 10^{-7}$
ρ	K	L_1	(c)	(d)	
$1.653 \cdot 10^{-12}$	1	$1.245 \cdot 10^6$	-353.4	$-9.924 \cdot 10^{-4}$	

Table 2.3: Validation constants for the extended system in (2.21) at the saddle-node bifurcation point. All values are written up to four decimal places. For more efficient computation, we multiplied by a preconditioning matrix and obtained the bounds ρ , K , and L_1 . We selected a matrix close to the Jacobian matrix of H_{sn} , whose inverse was used as a preconditioner. The accuracy constant δ_1 and the isolation bound δ_2 were derived using ρ , K , and L_1 . For the two conditions (c) and (d), which were checked separately after the validation involving H_{sn} , we used an interval arithmetic enclosure of the approximate solution with radius δ_1 .

2.3.2 Validation of the saddle-node bifurcation point

In this section, we use a computer-assisted proof to show that there is a saddle-node bifurcation point in the coral model. The precise result can be stated as follows.

Theorem 2.3.3 (Saddle-node bifurcation point). *The coral model in (2.4) and (2.5) has a saddle-node bifurcation point near the basic reproduction number $R_* \approx 12.28$, which corresponds to the parameter value $\lambda_* \approx 0.4213$, and for polyp population density $P_* \approx 853.4$. The precise error bounds are stated in Table 2.3.*

As in the previous subsection, the remainder of the present one is devoted to the verification of this theorem via computer-assisted rigorous methods. In order to establish the theorem, we need to verify the following conditions from the *classical saddle-node bifurcation theorem*, see for example [50]. Let $f : \mathbb{R} \times \mathbb{R}^d \rightarrow \mathbb{R}^d$ be a smooth mapping. Furthermore, assume the following four conditions:

(a) *Existence of a fixed point*: The map f has a fixed point at a specific parameter value,

i.e., we assume that $f(\lambda_0, x_0) = x_0$.

(b) *Simple eigenvalue 1*: The Jacobian matrix $D_x f(\lambda_0, x_0)$ has a simple eigenvalue of 1.

Let p and q denote the corresponding left and right eigenvectors, and suppose they

are normalized to satisfy $p^t q = 1$.

(c) *Transversality condition:* Using the above notation we assume

$$p^t D_\lambda f(\lambda_0, x_0) \neq 0 .$$

(d) *Nondegeneracy condition:* Now let $A(\lambda_0) = D_x f(\lambda_0, x_0)$, and consider the expansion of f given in (2.18). Then we suppose further that

$$p^t B(q, q) \neq 0 .$$

Then the classical saddle-node bifurcation theorem guarantees a saddle-node bifurcation at the pair (λ_0, x_0) .

In order to validate our bifurcation point using this theorem, we use again an extended system of the form $H_{sn} = 0$ to validate conditions (a) and (b), and then we verify conditions (c) and (d) separately afterwards. This time, the extended mapping H_{sn} is a map $H_{sn} : \mathbb{R}^{27} \rightarrow \mathbb{R}^{27}$, and it is defined as

$$H_{sn}(x, v, \lambda) = \begin{pmatrix} f(\lambda, x) - x \\ D_x f(\lambda, x)v - v \\ \|v\|^2 - 1 \end{pmatrix} . \quad (2.21)$$

In order to validate (c), and (d), we use interval arithmetic for both of these conditions, and show that 0 does not lie in the interval containing the resulting answer. Note that the vector q is just a multiple of v , and p can be found in a verified way using Intlab [69]. The summary of the constants of this validation process is given in Table 2.3. This computer-assisted proof is quite similar to the one used for the Neimark-Sacker bifurcation in the last subsection, and therefore we do not give any more elaboration on the technique used to

compute these values. This completes the proof of Theorem 2.3.3.

2.3.3 Validation of the transcritical bifurcation point

We close this section by showing that there is indeed a transcritical bifurcation on the trivial solution curve, i.e., the extinction curve. This time, it is not necessary to perform a computer-assisted proof, as the bifurcation can be established directly by hand.

Theorem 2.3.4 (Transcritical bifurcation point). *For the coral population model in (2.4) and (2.5) there exists a transcritical bifurcation point for basic reproduction number $R_* = c_2/c_1 \approx 72.22$, which corresponds to the parameter value $\lambda_* = R_*/(b \cdot a)$ and to $x_* = 0 \in \mathbb{R}^{13}$. Recall that the constants c_1 and c_2 were introduced in (2.2), and the vectors a and b were defined in (2.6) and the following paragraph.*

Proof. It is clear from the model that $x = 0$ is a fixed point for all values of the parameter λ . Furthermore, one can easily show that

$$\det(D_x f(\lambda, 0) - I) = \lambda - \frac{c_2}{c_1(b \cdot a)} .$$

Therefore, the Jacobian matrix of $f(\lambda, \cdot)$ at the origin has a simple eigenvalue of 1 if and only if λ equals

$$\lambda_* = \frac{c_2}{c_1(b \cdot a)} .$$

Now denote the right and left eigenvectors of $D_x f(\lambda_*, x_*)$ by v and w , respectively. One can show directly that $v = a$ defined in (2.6), and w is such that

$$w_1 = b \cdot a , \quad w_d = b_d , \quad \text{and} \quad w_k = b_k + S_k w_{k+1} \quad \text{for} \quad k = 2, \dots, d-1 .$$

Then in order to establish the transcritical bifurcation, two nondegeneracy conditions have

to be verified. Since we have $w^t D_\lambda f(\lambda_*, x_*) = 0$, one first has to show that

$$w^t D_{x\lambda} f(\lambda_*, x_*) v = \frac{(b \cdot a) c_1}{c_2} w^t b$$

is nonzero, which is clearly satisfied since all the terms of b and w are non-negative, and contains terms of the form b_k^2 (which are strictly positive for each nonzero b_k).

Second, we need to show that $w^t D_{xx} f(\lambda_*, x_*)[v, v] \neq 0$. Since only the first component of f , which we call f_1 , is nonlinear, one merely needs to consider the second derivative of this component function. We get the following formula.

$$D_{xx} f_1(\lambda_*, x_*)[v, v] = \frac{2(\beta - \alpha)}{\Omega} \sum_{k=2}^d p_k a_k.$$

By looking at the corresponding parameter values, this value is also nonzero, and therefore the second nondegeneracy condition holds. This completes the proof of the theorem. \square

2.4 Conclusion

In this chapter, we have considered an age-structured population model for red coral populations with a parameter of fitness. When the fitness increases sufficiently, a set of stable invariant closed curves of oscillating orbits form, and these stable curves persist for large values of the fitness parameter. It is not surprising that for small fitness parameters, solutions limit to extinction, but we see that even for large fitness, populations become extremely vulnerable, as they limit to oscillation spending long period of time near extinction.

The coral population model has a curve of fixed points containing a Neimark-Sacker, saddle-node, and transcritical bifurcation point. We develop new methods based on previous computer-assisted proof methods and use these methods to validate the branch of fixed points, and the three bifurcation points.

Chapter 3: Dynamics of Swarms with Communication Delay

Swarming behavior, which we define as the emergence of spatio-temporal group behaviors from simple local interactions between pairs of agents, is widespread and observed over a range of application domains. Examples can be found in biological systems over a range of length scales, from aggregates of bacterial cells and dynamics of skin cells in wound healing [9, 53, 67] to dynamic patterns of fish, birds, bats, and even humans [28, 36, 54, 83]. These systems are particularly interesting because they allow simple individual agents to achieve complex tasks in ways that are scalable, extensible, and robust to failures of individual agents. In addition, these swarming behaviors are able to form and persist in spite of complicating factors such as delayed actuation, latent communication, localized number of neighbors each agent is able to interact with, heterogeneity in agent dynamics, and environmental noise.

These factors have been the focus of previous theoretical research in describing the bifurcating spatial-temporal patterns in swarms, as seen for example in Refs. [42, 63, 76, 82]. Likewise, the application of swarms have been experimentally realized in areas, such as mapping [68], leader-following [64, 91], and density control [58]. To guarantee swarming behavior experimentally, control is typically employed [14, 26, 44, 80, 87] to prove convergence to a given state by relying on strict assumptions to guarantee the desired behavior. However, by relaxing certain assumptions, a number of studies show that even with simple interaction protocols, swarms of agents are able to converge to organized, coherent behaviors in a self-emergent manner; i.e. autonomously without control.

Different mathematical approaches yielded a wide selection of both agent-based [36, 54, 83, 85] and continuum models that predict swarming dynamics [16, 67, 82]. In almost all models, since the agents have just a few simple rules, there exists only a relatively small number of controllable parameters. The parameter set usually consists of a self-propulsion

force, a potential function governing attracting and repelling forces between agents, and a communicating radius governing the local neighborhood at which the agents can sense and interact with each other.

In both robotic and biological swarms, an additional parameter appears as a delay between the time information is perceived and the actuation (reaction) time of an agent. Such delays have now been measured in swarms of bats, birds, fish, and crowds of people [19, 28, 65]. The measured delays are longer than the typical relaxation times of the agents, and may be space and time dependent. Robotic swarms experience communication delays which provide similar effects to the delay experienced in natural swarms. Incorporating stationary delays along with a minimal set of parameters in swarm models results in multi-stability of rotational patterns in space [17, 41, 77, 78, 94].

In particular, for delays that are equal and fixed, one observes three basic swarming states or modes: Flocking, or translation state, which is a translating center of mass, Milling, or ring state, where the agents are splayed out on a ring in phase about a stationary center of mass, and a Rotating state, where the center of mass itself rotates (see Fig. 3.1.) Note that rotational state is a product of fixed delays, not previously seen in cases without any delays. This has been verified both theoretically and experimentally [17, 78]. However, in situations with robots, even simple communication models are based on the distance between agents [43, 96]. Accordingly, if one assumes that the delays are range dependent, the problem becomes one of studying state dependent delays where delays depend implicitly on the relative positions between agents.

3.1 Swarms with range-dependent delay

In general, range-dependent delay is a delay that depends only on distance between agents. When placing swarms in realistic environments, delays are not necessarily a continuous function of range, but rather it is the increasing probability of delays increasing stochastically

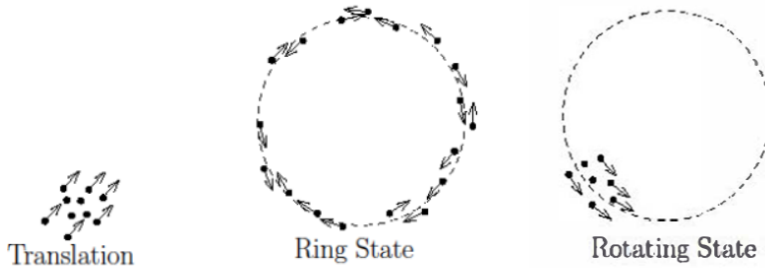


Figure 3.1: Three basic swarm states.

when agents move further away from one another beyond a certain radius [20, 21]. That is, the rate of communication becomes spatially dependent, whereby near agents see a signal with a fast rate of communication, but due to shading and fading of signals, communication rates are slowed and complex outside a given radius. Underwater communication of marine robot teams is an excellent swarm example where delays outside a significant radius impart rates of communication of one to two orders of magnitude greater than local communication rates [4].

The following swarm model takes a globally coupled swarm, and explicitly relaxes the fixed delay assumption, by including range dependent delay based on a fixed communication radius. We show that when range-dependent delays are included, new frequencies are introduced in the swarm center of mass, generating bifurcations and creating swarm dynamics on a torus. Our findings are important for robotic swarming where one of the goals is to produce desired patterns autonomously, without external controls. The pattern formations predicted in this section show how delayed information, whether coming from communication, actuations, or both, impacts the stability of swarm states, such as ring and/or rotating states. In an attempt to locate those parameter regions where patterns are destabilized, we may provide a more comprehensive characterization of the autonomously

accessible swarm states in the presence of range-dependent delay.

3.1.1 The swarm model

Consider a swarm of delay-coupled agents in \mathbb{R}^2 . Each agent is indexed by $i \in \{1, \dots, N\}$. We use a simple but general model for swarming motion. Each agent has a self-propulsion force that strives to maintain motion at a preferred speed and a coupling force that governs its interaction with other agents in the swarm. The interaction force is defined as the negative gradient of a pairwise interaction potential $U(\cdot, \cdot)$. All agents follow the same rules of motion; however, mechanical differences between agents may lead to heterogeneous dynamics; this effect is captured by assigning different acceleration factors (denoted κ_i) to the agents. In this section, we assume $\kappa_i = 1$ for all i . For the effect of heterogeneity on the swarm bifurcations, see [76].

Agent-to-agent interactions occur along a graph $\mathcal{G} = \{\mathcal{V}, \mathcal{E}\}$, where \mathcal{V} is the set of vertices v_i in the graph and \mathcal{E} is the set of edges e_{ij} . The vertices correspond to individual swarm agents, and edges represent communication links; that is, agents i and j communicate with each other if and only if $e_{ij} \in \mathcal{E}$. All communications links are assumed to be bi-directional, and all communications occur with a time delay τ . That is, range dependence is not included. Let $\mathbf{r}_i \in \mathbb{R}^2$ denote the position of the agent i and let $\mathcal{N}_i = \{v_j \in \mathcal{V} : e_{ij} \in \mathcal{E}\}$ denote its set of neighbors of agent i . The motion of agent i is governed by the following equation:

$$\ddot{\mathbf{r}}_i = \kappa_i(1 - \|\dot{\mathbf{r}}_i\|^2)\dot{\mathbf{r}}_i - \kappa_i \sum_{j \in \mathcal{N}_i} \nabla_x U(\mathbf{r}_i(t), \mathbf{r}_j^\tau(t)), \quad (3.1)$$

where superscript τ is used to denote time delay, so that $\mathbf{r}_j^\tau(t) = \mathbf{r}_j(t - \tau)$, $\|\cdot\|$ denotes the Euclidean norm, and ∇_x denotes the gradient with respect to the first argument of U . The first term in Eq. 3.1, $(1 - \|\dot{\mathbf{r}}_i\|^2)\dot{\mathbf{r}}_i$, is the self-propulsion and frictional drag forces on each agent. Therefore, in the absence of coupling, agents tend to move on a straight line with unit speed $\|\mathbf{r}_i\| = 1$ as time goes to infinity.

To analyze the dynamics of a large scale swarm, we use a harmonic interaction potential with short-range repulsion.

$$U(\mathbf{r}_i, \mathbf{r}_j^\tau) = c_r e^{-\frac{\|\mathbf{r}_i - \mathbf{r}_j\|}{l_r}} + \frac{a}{2N} \|\mathbf{r}_i - \mathbf{r}_j^\tau\|^2. \quad (3.2)$$

In Eq. 3.1, it is assumed that the communication delay, τ , is independent of the distance, or range, between any pair of agents. (Notice that the exponent of the repulsion term is independent of the delay since the repulsion force is local.) With the addition of delays in the network, it was shown in homogeneous communication networks that in addition to the usual dynamical translating and milling (or ring) states, for sufficiently large τ , new rotational states emerge [78]. In particular, for a given attractive coupling strength, there is a delay that destabilizes the periodic ring state into a rotating state, in which the agents coalesce to a small group and move around a fixed center of rotation; this behavior is quite different from the ring state where agents are spread out in a splay state phase. The rotating state is only observed with delay introduced in the communication network, and it appears through a Hopf bifurcation as previously studied [94].

However, in real-world robotic swarms, communication delays are not uniform between all pairs of agents; delays may be stochastic or even state-dependent. In order to handle range dependent delays, we will make an approximation that depends on a communication range radius.

Approximating range dependent delayed coupling

For the coupling term, we are interested in introducing an approximation to range based coupling delay. Since all communicating agents send signals with some delay, we compute relative distances defined as

$$D_{i,j}^\tau \equiv \|\mathbf{r}_i - \mathbf{r}_j^\tau\|. \quad (3.3)$$

We define a Heaviside function, $H(x)$, that is zero when $x \leq 0$ and 1 otherwise, and we employ global coupling based on a spring potential. For our range dependent metric, we let $\epsilon \geq 0$ denote the range radius. Suppose that when the separation between two agents is small, that is less than ϵ , then sensing between two agents is almost immediate. In practice, the time needed for sensing depends on several factors, such as actuation times, and so distances in practice are computed with delay. Therefore, we model the coupling term for the i^{th} agent as

$$\begin{aligned} C_i(\mathbf{r}_i, \mathbf{r}_j, \mathbf{r}_j^\tau, \epsilon) &= -\frac{a}{N} (\nabla_x U(\mathbf{r}_i(t), \mathbf{r}_j^\tau(t))) H(D_{i,j}^\tau - \epsilon) \\ &\quad - \frac{a}{N} (\nabla_x U(\mathbf{r}_i(t), \mathbf{r}_j(t))) (1 - H(D_{i,j}^\tau - \epsilon)), \end{aligned} \quad (3.4)$$

where the first coupling term has delay turned on since the distance is outside a ball of radius ϵ , while the second term has no delay since the distance is within the ϵ ball. The resulting swarm model with range dependence from Eq. 3.4 is now

$$\ddot{\mathbf{r}}_i = \kappa_i (1 - \|\dot{\mathbf{r}}_i\|^2) \dot{\mathbf{r}}_i - \kappa_i \sum_{j \in \mathcal{N}_i} C_i(\mathbf{r}_i, \mathbf{r}_j, \mathbf{r}_j^\tau, \epsilon). \quad (3.5)$$

If the delayed distance is within an ϵ ball, then we evaluate the coupling without delay. Otherwise the coupling is delayed. Thus the coupling function takes into account when delay is active or not between pairs of communicating agents, and depends on the range radius, ϵ .

The Heaviside function of the right hand side of Eq. 3.9 renders the differential delay equation derivatives discontinuous, and as such poses a numerical integration problem. To mollify the lack of smoothness, we approximate $H(x)$ by letting $H(x) \approx \frac{1}{\pi} \arctan(kx) + \frac{1}{2}$, where $k \gg 1$ and constant, and limits on the Heaviside function as $k \rightarrow \infty$.

Using only the delayed distance to compute a range dependent coupling assumes that any measurement is not instantaneous. If one were to be able to compute the ideal situation

where delay would not be a sensing factor, then certain issues would need to be resolved, which we do not consider here.

Numerical simulations of full swarms

Examples of simulations using the swarm model with the range dependent coupling are shown below. Here the number of agents, $N = 150$, and the coupling strength, $a = 2.0$. For the remainder of the analysis, we set $c_r = 0$, and note that the attractors persist when the repulsive amplitude is sufficiently small [78].

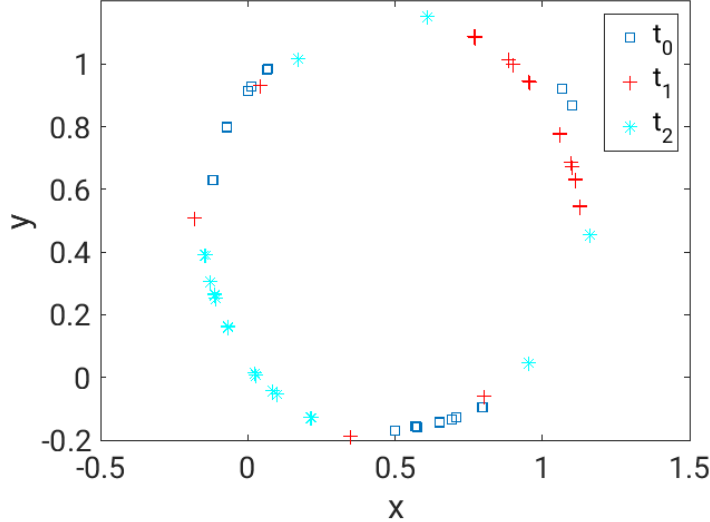


Figure 3.2: Three snapshots of swarm state in space for $\epsilon = 0.01$, $a = 2.0$, $\tau = 1.75$. Sample times $t_0, t_1 = t_0 + 20, t_2 = t_0 + 40$.

Note that even when ϵ is very small, as shown in Fig. 3.2, we observe a mix of clustered states which are a combination of pure ring and rotation states. The agents tend to cluster into local groups, and the clusters move in clockwise and counter-clockwise directions as in the ring state. Here, however, the phase differences between agents are non-uniform. When examining a single random agent, as shown in Fig 3.3, it is periodic with a sharp

frequency of rotation, and the relative positions of all individual agents are phase locked. When considering the center of mass of the positions over all agents, $\mathbf{R} \equiv \frac{1}{N} \sum_i \mathbf{r}_i$, the center of mass does small amplitude oscillations about a fixed point (not shown).

As the radius ϵ increases, instability of the periodic mixed state occurs, giving rise to more complicated behavior, as seen in Fig. 3.3. New frequencies are introduced, causing the ring state to appear as a quasi-periodic attractor. Moreover, the dynamics of the center of mass has its own non-trivial dynamics which includes the effects of new frequencies.

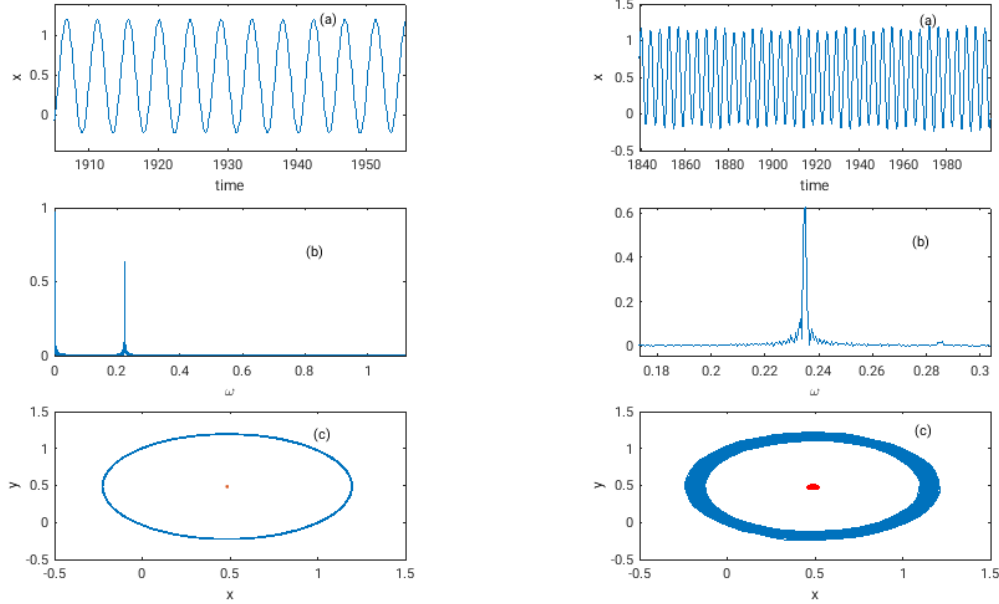


Figure 3.3: Left: Swarm Ring State $\epsilon = 0.01, a = 2.0, \tau = 1.75$. (a) Time series of the x-component of a single agent. (b) The power spectrum, that was computed by FFT method in MATLAB, showing a sharp frequency. (c) A phase portrait of the orbit of a single agent. The red point denotes the center of mass. Right: Swarm instability $\epsilon = 0.25, a = 2.0, \tau = 1.75$. (a) Time series of the x-component of a single agent. (b) The Power spectrum showing a slight broadening and birth of a new frequency. (c) A phase portrait of the orbit of a single agent.

By examining the Poincare map of the attractors, the instability gives rise to dynamics

which we conjecture is motion on a torus. Letting (M_x, M_y) denote the time averaged center of mass over all agents, we compute the sequence $x(t_i), i = 1..M$ when $y(t_i) = 0$ and $x(t_i) > M_x$. The result is shown in the two panels in Fig. 3.4. Panel (a) shows a complicated toroidal motion after transients are removed of the center of mass in Fig. 3.3c. For a single frequency, the dynamics of the center of mass would be a single fixed point. The addition of new frequencies is revealed in the Poincare map as complicated motion on a torus. For larger values of ϵ , the motion on the torus converges to a periodic attractor in panel (b).

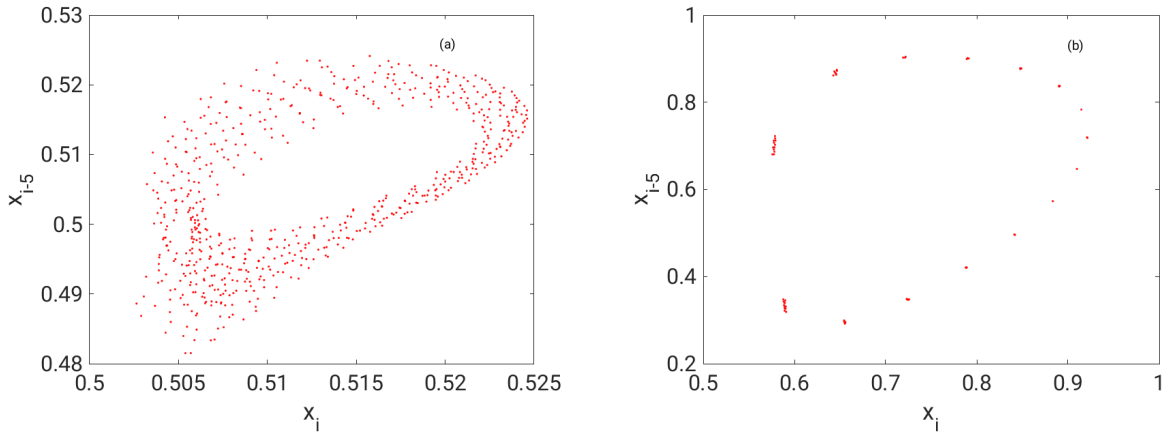


Figure 3.4: Poincare map of Eqs. 3.1-3.4 for (a) $\epsilon = 0.25$, (b) $\epsilon = 0.5$. Other parameters are fixed: $a = 2.0, \tau = 1.75$. See text for details.

3.1.2 Mean-field equation of range dependent delay coupled swarm

In order to shed some light on the origin of the bifurcation to dynamics on a torus, we examine the full swarm model from a mean-field perspective. The mean field is much lower dimensional, and a full bifurcation analysis may be done. We consider the case of all-to-all

communication. We define $\mathbf{R} = \frac{1}{N} \sum_{i=1}^N \mathbf{r}_i$ and $\mathbf{r}_i = \mathbf{R} + \delta\mathbf{r}_i$, where $\delta\mathbf{r}_i$ is a fluctuation term

with the identity

$$\sum_{i=1}^N \delta \mathbf{r}_i = 0. \quad (3.6)$$

Then we can write Eq. 3.5 as

$$\begin{aligned} \ddot{\mathbf{R}} + \delta \ddot{\mathbf{r}}_i &= (1 - |\dot{\mathbf{R}} + \delta \dot{\mathbf{r}}_i|^2)(\dot{\mathbf{R}} + \delta \dot{\mathbf{r}}_i) \\ &\quad - \frac{a}{N} \sum_{j=1, j \neq i}^N ((\mathbf{R} + \delta \mathbf{r}_i) - (\mathbf{R}^\tau + \delta \mathbf{r}_j^\tau)) C_{1,i} \\ &\quad - \frac{a}{N} \sum_{j=1, j \neq i}^N ((\mathbf{R} + \delta \mathbf{r}_i) - (\mathbf{R} + \delta \mathbf{r}_j)) C_{2,i}, \end{aligned} \quad (3.7)$$

where

$$\begin{aligned} C_{1,i} &= H(\|\mathbf{r}_i - \mathbf{r}_j^\tau\| - \epsilon) \\ &= H(\|(\mathbf{R} + \delta \mathbf{r}_i) - (\mathbf{R}^\tau + \delta \mathbf{r}_j^\tau)\| - \epsilon) \\ &= H(\|\mathbf{R} - \mathbf{R}^\tau + \delta \mathbf{r}_i - \delta \mathbf{r}_j^\tau\| - \epsilon) \end{aligned}$$

and

$$C_{2,i} = 1 - C_{1,i}.$$

We use the following to reduce the equations of motion to the mean field: From Eq. 3.6, we note

$$\begin{aligned} \sum_{i=1}^N \delta \mathbf{r}_i^\tau &= \sum_{j=1, j \neq i}^N \delta \mathbf{r}_j^\tau + \delta \mathbf{r}_i^\tau = 0 \iff \\ &\quad - \sum_{j=1, j \neq i}^N \delta \mathbf{r}_j^\tau = \delta \mathbf{r}_i^\tau. \end{aligned} \quad (3.8)$$

We further assume that all perturbations from the mean, $\delta\mathbf{r}_i$, are all negligible. (This is always true if the coupling amplitude is sufficiently large.) In addition, we use the fact that $\frac{a(N-1)}{N}$ limits to a , as $N \rightarrow \infty$. Therefore, we obtain mean field approximation for the center of mass of range dependent coupled delay case:

$$\dot{\mathbf{R}} = (1 - |\dot{\mathbf{R}}|^2) \cdot \dot{\mathbf{R}} - a(\mathbf{R} - \mathbf{R}^\tau) \cdot H(\|\mathbf{R} - \mathbf{R}^\tau\| - \epsilon) \quad (3.9)$$

3.1.3 Numerical analysis of the mean field equation

Examples of rotational attractors

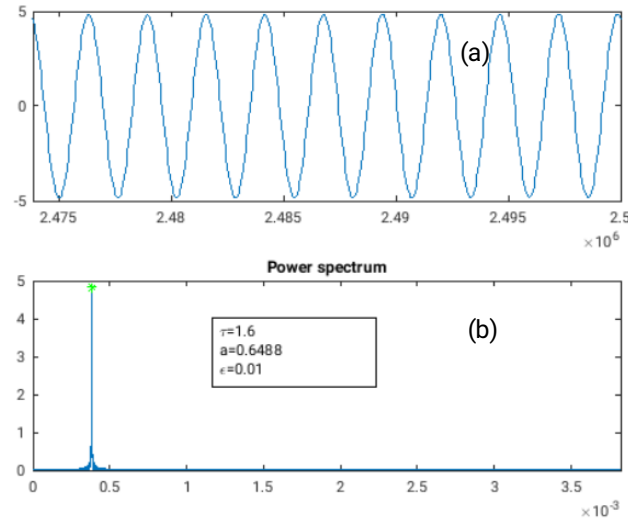


Figure 3.5: Periodic motion of the mean field Eq. 3.9 for $\epsilon = 0.01, a = 0.64, \tau = 1.6$. (a) Time series of the x-component of the mean field. (b) Power spectra of the time series.

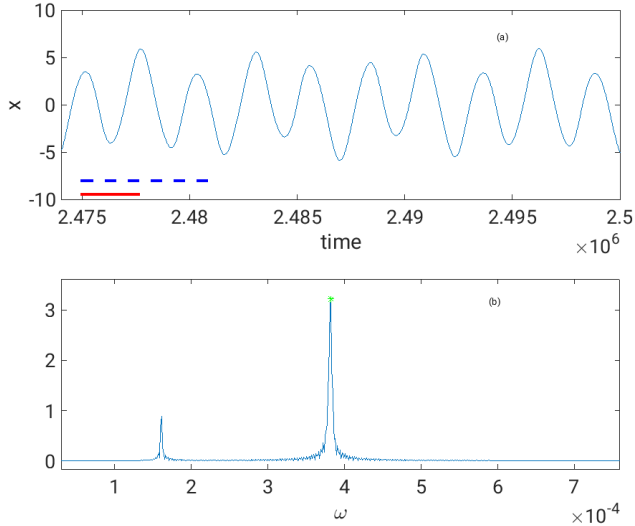


Figure 3.6: Quasi-periodic motion of the mean field Eq. 3.9 for $\epsilon = 0.01, a = 0.64, \tau = 1.609$. (a) Time series of the x-component of the mean field. Solid (red) line denotes period length of dominant spectral peak. Dashed line denotes period length of secondary peak. (b) Power spectra of the time series.

As in the case for the full multi-agent system, we see the existence of periodic behavior for τ sufficiently below an instability threshold, as shown in the time series of Fig. 3.5. As we increase τ , we expect the periodic orbit to lose stability, resulting in a new attractor. In particular, one notices the emergence of a new frequency in addition to the existing dominant one, as shown in Fig. 3.6. The additional frequency usually implies a bifurcation to dynamics on a torus, or a higher dimensional torus.

We now investigate this transition by tracking the stability via monitoring the Floquet exponents corresponding to the periodic orbit. For a general differential delay equation given by $\dot{\mathbf{x}}(t) = \mathbf{F}(\mathbf{x}(t), \mathbf{x}(t - \tau))$, if $\phi(t) = \phi(t + T)$ for all $t \geq 0$, then stability is determined by

examining the linearized equation along $\phi(t)$:

$$\begin{aligned}\dot{\mathbf{X}}(t) &= \frac{\partial \mathbf{F}}{\partial \mathbf{x}(t)}(\phi(t), \phi(t-\tau)) \mathbf{X}(t) \\ &\quad + \frac{\partial \mathbf{F}}{\partial \mathbf{x}(t-\tau)}(\phi(t), \phi(t-\tau)) \mathbf{X}(t-\tau).\end{aligned}\tag{3.10}$$

The stability of the periodic solution is determined by the spectrum of the time integration operator $U(T, 0)$ which integrates Eq. 3.10 around $\phi(t)$ from time $t = 0$ to $t = T$. This operator is called the monodromy operator and its (infinite number of) eigenvalues, which are independent of the initial state, are called the Floquet multipliers [31]. For autonomous systems, it is necessary and sufficient there exists a trivial Floquet multiplier at 1, corresponding to a perturbation along the periodic solution [32, 34]. The periodic solution is stable provided all multipliers (except the trivial one) have modulus smaller than 1; it is unstable if there exists a multiplier with modulus larger than 1. Bifurcations occur whenever Floquet multipliers move into or out of the unit circle. Generically three types of bifurcations occur in a one parameter continuation of periodic solutions: a turning point, a period doubling, and a torus bifurcation where a branch of quasi-periodic solutions originates and where a complex pair of multipliers crosses the unit circle [31]. We have tracked a set of stable periodic orbits for various radii of ϵ , and located the change in stability by computing the Floquet multipliers as detailed above. The results plotted in Fig. 3.7 show that for a range of radii ϵ , there exists a bifurcation to a torus at some delay. Notice that as ϵ increases, there results an increase in the size of the orbits, which qualitatively agrees with our full agent based simulations.

Since there exists a range of delays which destabilize periodic swarm dynamics for each ϵ , we summarize the onset of torus bifurcations by plotting the locus of points at which stability changes as a function of coupling amplitude and delay. The results are plotted in Fig. 3.8, with AUTO by using compartment model for τ . Fig. 3.8 is revealing in that

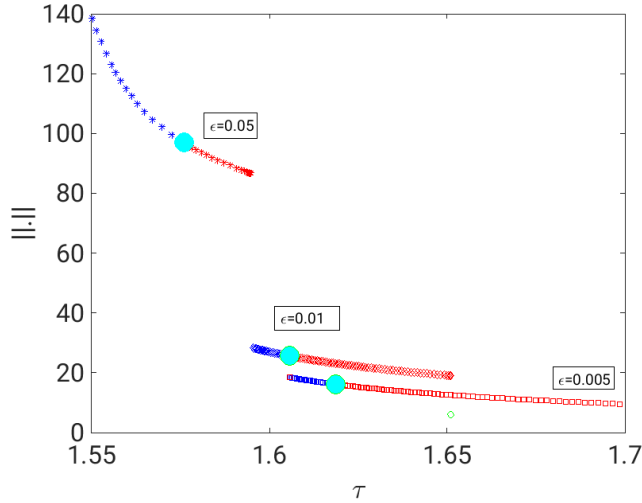


Figure 3.7: Bifurcation plot on the mean field equation showing the L^2 norm of the periodic orbits as a function of delay τ . Parameter $a=0.68$. Red (blue) markers denote unstable (stable) orbits.Cyan symbols denote the change in stability where a pair of complex eigenvalues cross the imaginary axis.

it shows a functional relationship of the bifurcation onset that is similar over a range of ϵ . For larger values of ϵ , it is clear that lower values of delay and coupling are required to generate bifurcations. This holds true over two orders of ϵ . For a fixed value of ϵ , we also see monotonic relationship between delay and coupling strength, so that it is easier for smaller delays to destabilize periodic motion for larger coupling strengths.

3.1.4 Conclusions

We considered a new model of a swarm with delay coupled communication network, where the delay is considered to be range dependent. That is, given a range radius, delay is on if two agents are outside the radius, and zero otherwise. The implication is that small delays do not matter if the agents are close to each other.

The additional range dependence creates a new set of bifurcations not previously seen. For general swarms without delay, the usual states consist of flocking (translation) or ring / rotational state (milling), with agents spread in phase. With the addition of a fixed delay,

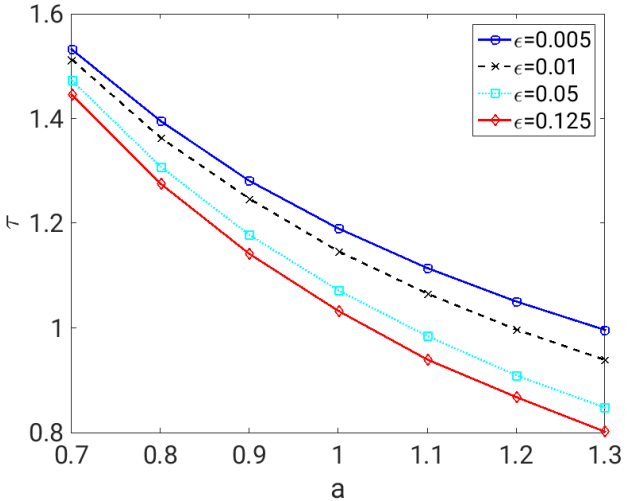


Figure 3.8: Plotted is the locus of points at which torus bifurcations emerge as a function of coupling amplitude a , delay τ for various range radii ϵ for the mean field Eq. 3.9.

a rotational state bifurcates that has all agents in phase and rotate together [39]. Range dependence introduces a new rotational bifurcating state that exhibits behavior observed as a new mixed state combining dynamics of both ring and rotating states.

The radius parameter ϵ was used to quantify the bifurcation of the rotational mixed state. For small ϵ , we see dynamics for the full swarm shows clustered counter-rotational behavior that is periodic. This agrees for small radius values in the mean field description as well. As the radius increases, the mixed periodic state generates new frequencies in the full model, which are manifested as torus bifurcations in the mean field. Mean field analysis was done by tracking Floquet multipliers that cross the imaginary axis as complex pairs. Frequency analysis explicitly shows the additional frequencies in the mean field.

Finally, we tracked the locus of coupling amplitudes and delay for various values of ϵ locating the parameters at which torus bifurcation occur. The results reveal that as ϵ increases, torus bifurcations onset at lower values of coupling amplitude and delay. The implications are that more complicated behavior than periodic motion has a greater probability of being observed in both theory and experiment if range dependence of delay is

included.

3.2 Unstable modes and bi-stability in delay-coupled swarms

Deriving inspiration from nature, embodied artificial swarm systems have been created to mimic emergent pattern formation— with the ultimate goal of designing robotic swarms that can perform complex tasks autonomously [6–8,93]. Recently robotic swarms have been used experimentally for applications such as mapping [68], leader-following [64, 91], and density control [58]. To achieve swarming behavior, often, robots are controlled based on models, where swarm properties can be predicted exactly [14, 26, 44, 80, 87]. Such approaches rely on strict assumptions to guarantee behavior. Any uncharacterized dynamics can cause patterns to be lost or changed. This is particularly the case for robotic swarms that move in uncertain environments and must satisfy realistic communication constraints.

In general, time-delays in swarms may result in multi-stability of rotational patterns in space, and the possibility of switching between patterns [2, 17, 33, 37, 41, 49, 77, 78, 94]. Though observed in simulations and experiments, swarm bi-stability due to time-delay has lacked an accurate quantitative description, which we provide in this section.

Consider a system of mobile agents, or swarmers, moving under the influence of three forces: self-propulsion, friction, and mutual attraction. In the absence of attraction, each swarmer tends to a fixed speed, which balances propulsion and friction but has no preferred direction. The agents are assumed to communicate through a network with time delays. Namely, each agent is attracted to where its neighbors were at some moment in the past. A simple model which captures the basic physics is

$$m\ddot{\mathbf{r}}_l = (\alpha - \beta \|\dot{\mathbf{r}}_l\|^2) \dot{\mathbf{r}}_l + \frac{a}{N} \sum_{j \neq l} [\mathbf{r}_j(t - \tau) - \mathbf{r}_l] + \xi_l(t). \quad (3.11)$$

where m is the mass of each agent, α is a self-propulsion constant, β is a friction constant, a is a coupling constant, τ is a characteristic time delay, N is the number of agents, \mathbf{r}_l is

the position-vector for the l -th agent in two spatial dimensions, and $\xi_l(t)$ is a small noise source [15, 18, 23, 57, 94]. Equation (3.11) has been implemented in experiments with several robotics platforms including autonomous cars, boats, and quad-rotors [17, 78]. Note that we take $m = \alpha = \beta = 1$ and neglecting noise, we recover Equation (3.1) for $\kappa_i = 1$ case from the previous section. Again in this section, we consider the simple case of spring interaction forces and global communication topology for illustration and ease of analysis; however, these assumptions can be relaxed with predictable effects on the dynamics [11, 42, 78, 82].

3.2.1 Swarming pattern and stability

From generic initial conditions a swarm described by Eq.(3.11) tends to one of two spatio-temporal patterns: a ring (milling) state, or a rotating state – depending on initial conditions and parameters [23]. The two patterns can be seen in Fig.3.9(b). Note that the snapshots in time are drawn from simulations of Eq.(3.11) with Gaussian white-noise, $\langle \xi_l^{(c)}(t) \xi_j^{(c')}(t') \rangle = 0.02 \cdot \delta(t - t') \delta_{lj} \delta_{cc'}$, where c and c' denote the Cartesian components, x or y . The emergence and stability of the ring and rotating patterns are often qualitatively described using mean-field approximations, in which the motions of agents relative to the swarm’s center-of-mass are neglected [61, 94]. Though useful, such descriptions do not capture bi-stability and noise-induced switching, let alone the more complex motions observed in experiments [17, 78]. What’s more, higher-order approximation techniques predict bi-stability qualitatively, but suffer from quantitative inaccuracy, and are difficult to analyze [95]. Hence, an analyzable and accurate description of stability is needed, especially for robotics experiments which use Eq.(3.11) (and its generalizations) as a basic autonomy-controller. In support of such experiments, we analyze the linear stability of the ring and rotating states exactly for large N in the noiseless limit, and compare our predictions to simulations.

Ring state

First, since the ring and rotating states are effectively two types of phase-locked solutions with different phase distributions and frequencies, it is useful to transform Eq.(3.11) into polar coordinates where each can be naturally represented as fixed-point solutions in appropriately chosen rotating reference frames. Introducing the coordinate transformations $\mathbf{r}_l \equiv \langle r_l \cos(\phi_l), r_l \sin(\phi_l) \rangle$, substituting into Eq.(3.11), and neglecting noise, we obtain:

$$mr_l\ddot{\phi}_l = [\alpha - \beta(r_l^2\dot{\phi}_l^2 + \dot{r}_l^2)]r_l\dot{\phi}_l - 2m\dot{r}_l\dot{\phi}_l \quad (3.12)$$

$$+ \frac{a}{N} \sum_{j \neq l} r_j(t - \tau) \sin(\phi_j(t - \tau) - \phi_l),$$

$$m\ddot{r}_l = [\alpha - \beta(r_l^2\dot{\phi}_l^2 + \dot{r}_l^2)]\dot{r}_l + mr_l\dot{\phi}_l^2 \quad (3.13)$$

$$+ \frac{a}{N} \sum_{j \neq l} [r_j(t - \tau) \cos(\phi_j(t - \tau) - \phi_l) - r_l].$$

For large N we can approximate the restricted sums in Eqs.(3.12-3.13), over all but one of the agents, with sums over all of the agents. In this case, ring-state formations are solutions of Eqs.(3.12-3.13) where radii and frequencies are constant [94], and phases are splayed uniformly,

$$r_j(t) = \sqrt{\frac{m\alpha}{\beta a}}, \quad \phi_j(t) = \frac{2\pi(j-1)}{N} + \sqrt{\frac{a}{m}}t. \quad (3.14)$$

This is easy to check by direct substitution. In general, many related ring states also exist, i.e, where some number of agents have the opposite frequency, $-\sqrt{a/m}$, and are distributed uniformly around a concentric ring. In our stability analysis below, we focus on the case where all agents rotate in the same direction for three reasons: this case persists when small repulsive forces are added (as in robotics experiments [17, 78]), the stability of any given

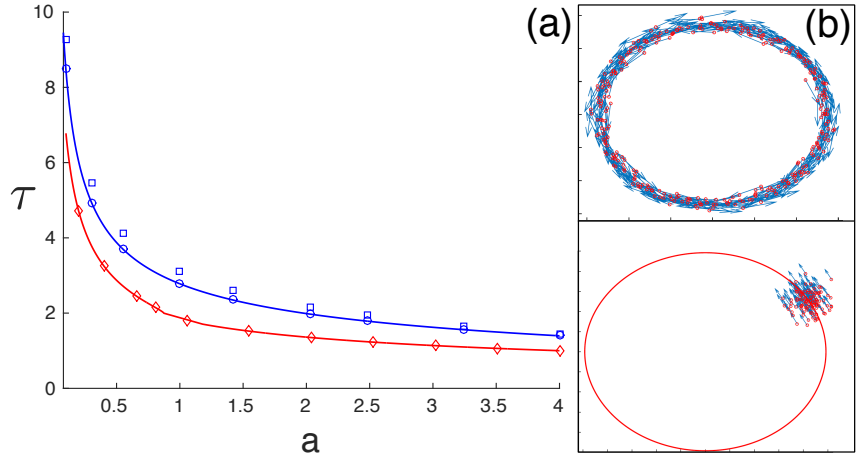


Figure 3.9: Stability diagram for delay-coupled swarms. (a) The blue (upper) curve denotes a Hopf bifurcation for the ring state (b, upper). The red (lower) curve denotes a combined line for saddle-node and double-Hopf bifurcations for the rotating state (b, lower). Points denote simulation-determined stability changes for $N = 600$: a ring state with all agents rotating in the same direction (blue circles), a ring state with half the agents rotating in the opposite direction (blue squares), and a rotating state (red diamonds). (b) Snapshots for both states in the x-y plane ($a = 1, \tau = 2.6, N = 100$). Positions are drawn with red circles and velocities with blue arrows. In all panels $m = \alpha = \beta = 1$.

ring pattern has only a weak dependence on the number of nodes rotating in each direction (as demonstrated with simulations), and analytical tractability.

To determine the local stability of the ring state we need to understand how small perturbations to Eq.(3.14) grow (or decay) in time. Our first step is to substitute a general perturbation, $r_j(t) = \sqrt{m\alpha/\beta a} + B_j(t)$ and $\phi_j(t) = 2\pi(j - 1)/N + \sqrt{a/m} t + A_j(t)$, into Eqs.(3.12-3.13) and collect terms to first order in $A_j(t)$ and $B_j(t)$ (assuming $|A_j|, |B_j| \ll 1 \forall j$). The result is the following linear system of delay-differential equations for $N \gg 1$ *with constant coefficients* – the latter property is a consequence of our transformation into

the proper coordinate system and is what allows for an analytical treatment:

$$\sqrt{\frac{m\alpha}{\beta a}}[m\ddot{A}_l + 2\alpha\dot{A}_l] + 2\sqrt{\frac{a}{m}}[m\dot{B}_l + \alpha B_l] = \frac{a}{N} \sum_j [B_j^\tau \sin\left(\frac{2\pi(j-l)}{N} - \sqrt{\frac{a}{m}}\tau\right) + (A_j^\tau - A_l)\sqrt{\frac{m\alpha}{\beta a}} \cos\left(\frac{2\pi(j-l)}{N} - \sqrt{\frac{a}{m}}\tau\right)], \quad (3.15)$$

$$m\ddot{B}_l - 2m\sqrt{\frac{\alpha}{\beta}}\dot{A}_l = \frac{a}{N} \sum_j [B_j^\tau \cos\left(\frac{2\pi(j-l)}{N} - \sqrt{\frac{a}{m}}\tau\right) - (A_j^\tau - A_l)\sqrt{\frac{m\alpha}{\beta a}} \sin\left(\frac{2\pi(j-l)}{N} - \sqrt{\frac{a}{m}}\tau\right)] \quad (3.16)$$

where $A_j^\tau \equiv A_j(t - \tau)$ and $B_j^\tau \equiv B_j(t - \tau)$.

Given the periodicity implied by the equally-spaced phase variables in Eq.(3.14), it is natural to look for eigen-solutions of Eqs.(3.15-3.16) in terms of the discrete Fourier transforms of $A_j(t)$ and $B_j(t)$. In fact, by inspection we can see that only the first harmonic survives the summations on the right-hand sides of Eqs.(3.15-3.16), because of the sine and cosine terms, and hence we look for particular solutions: $A_j(t) = A \exp\{\lambda t - 2\pi i(j-1)/N\}$ and $B_j(t) = B \exp\{\lambda t - 2\pi i(j-1)/N\}$. Substitution and a fair bit of algebra gives the following transcendental equation for the stability exponent, λ , of the ring state:

$$\frac{m\lambda^2 + 2\alpha\lambda - \frac{a}{2}e^{-\tau[\lambda+i\sqrt{\frac{a}{m}}]}}{2m\sqrt{\frac{a}{m}}\lambda - \frac{a}{2i}e^{-\tau[\lambda+i\sqrt{\frac{a}{m}}]}} + \frac{2\sqrt{\frac{a}{m}}[m\lambda + \alpha] - \frac{a}{2i}e^{-\tau[\lambda+i\sqrt{\frac{a}{m}}]}}{m\lambda^2 - \frac{a}{2}e^{-\tau[\lambda+i\sqrt{\frac{a}{m}}]}} = 0. \quad (3.17)$$

In general, the ring state will be linearly stable if there are no solutions to Eq.(3.17) with $Re[\lambda] > 0$. In fact, varying a and τ while fixing the other parameters, we discover a Hopf bifurcation, generically, at which $\lambda = \pm i\omega_c$ [50]. An example Hopf line is shown in Fig.3.9(a) in blue for $m = \alpha = \beta = 1$. Based on our analysis, we expect the ring state to be locally stable

below the blue line and unstable above it. For comparison, the blue circles in Fig.3.9(a) denote simulation-determined transition points: the largest $\tau(a)$ for which a swarm of 600 agents, initially prepared in a ring state with a small random perturbation (i.e., independent and uniformly distributed A_j and B_j over $[-10^{-5}, 10^{-5}]$), returns to a ring configuration after an integration time of $t = 20000$. Numerical predictions from Eq.(3.17) show excellent agreement with these simulation results. Similarly determined transition points for a ring formation in which half the agents rotate in one direction, and half rotate in the opposite direction, are shown with blue squares. We can see that the ring's Hopf-transition line still gives a good approximation for this more general case, especially for larger values of a .

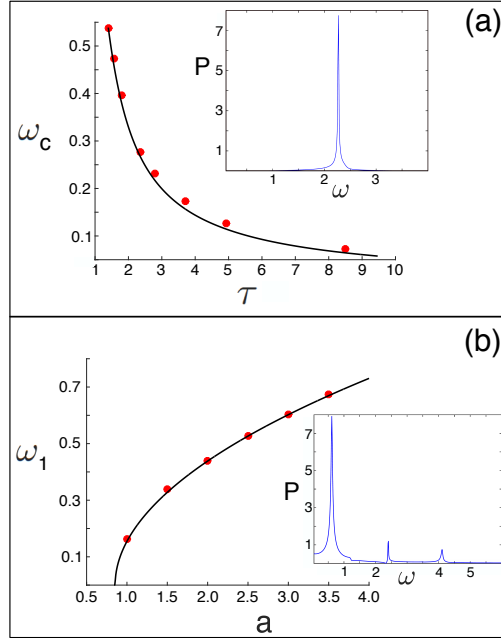


Figure 3.10: Frequency of unstable modes near bifurcation. (a) unstable frequency for the ring state at the Hopf bifurcation (black line) determined from the power spectrum of the swarm's center-of-mass (red circles). (b) unstable frequency for the rotating state at the double-Hopf bifurcation (black line) determined from the power spectrum for a single agent. Inlet panels show example spectra for both states: (a) when $(a=1.565, \tau=3.243)$, (b) when $(a=3.5, \tau=1.059)$. In all panels $m=\alpha=\beta=1$.

In addition to the transition points, we can check the frequency of oscillations around the ring state, implied by the existence of an unstable mode for $\tau(a)$ slightly above the Hopf bifurcation. First we perform a simulation initially prepared in the ring state with a small perturbation (as described in the preceding paragraph), and compute the peak frequency, ω^* , in the Fourier spectrum of the swarm's center-of-mass, $\mathbf{R}(t) \equiv \sum_j \mathbf{r}_j/N$. An example is shown in the inlet panel of Fig.3.10(a) for ($a=3.243$, $\tau=1.565$); the symbol P denotes the absolute value of the Fourier transform. Second, we plot $\omega_c = \omega^* - \sqrt{a/m}$ and compare to predictions from solutions of Eq.(3.17) with $\lambda = \pm i\omega_c \neq 0$ for a range of time delays. The comparison is shown in Fig.3.10(a) with excellent agreement.

Rotating state

Next, we perform a similar stability analysis for the rotating state, which has a different bifurcation structure and unstable modes. Unlike the ring state, the rotating state entails a collapse of the swarm on to the center of mass with complete phase and amplitude synchronization (in the noiseless limit). In polar coordinates, the agents satisfy $r_j(t)=R$ and $\phi_j(t)=\Omega t$ [94], where

$$0 = m\Omega^2 - a[1 - \cos \Omega\tau], \quad (3.18)$$

$$R = \frac{1}{|\Omega|} \sqrt{\frac{\alpha - a \sin(\Omega\tau)/\Omega}{\beta}}. \quad (3.19)$$

In order to determine the local stability of the rotating state we substitute $r_j(t) = R + B_j \exp\{\lambda t\}$ and $\phi_j(t) = \Omega t + A_j \exp\{\lambda t\}$, into Eqs.(3.12-3.13) and, again, collect terms to first order in A_j and B_j (assuming $|A_j|, |B_j| \ll 1 \forall j$). The result is another linear system of equations with constant coefficients. After some algebra, and replacing the restricted

sums in Eqs.(3.12-3.13) by sums over all particles, we obtain:

$$R[m\lambda^2 - \lambda(\alpha - 3\beta R^2\Omega^2) + a \cos(\Omega\tau)]A_l + \Omega[2m\lambda - \alpha + 3\beta R^2\Omega^2]B_l \quad (3.20)$$

$$= \frac{ae^{-\lambda\tau}}{N} \sum_j [R \cos(\Omega\tau)A_j - \sin(\Omega\tau)B_j],$$

$$[aR \sin(\Omega\tau) - 2mR\Omega\lambda]A_l + [m\lambda^2 - m\Omega^2 - \lambda(\alpha - \beta R^2\Omega^2) + a]B_l \quad (3.21)$$

$$= \frac{ae^{-\lambda\tau}}{N} \sum_j [R \sin(\Omega\tau)A_j + \cos(\Omega\tau)B_j].$$

There are two primary categories of solutions to Eqs.(3.20-3.21). The first is $A_l = A$ and $B_l = B$, which we call the homogeneous modes. Because all agents move together (equal to the center-of-mass motion) the stability entailed by the homogeneous modes should match the mean-field approximation mentioned above and analyzed in [94]. Because the mean-field is known to be quantitatively inaccurate for capturing stability [17, 95], we focus on the second set of solutions: $\sum_j A_j/N = 0$ and $\sum_j B_j/N = 0$. The stability-exponents, λ , for these modes satisfy

$$\begin{aligned} & \frac{2m\Omega\lambda - a \sin(\Omega\tau)}{m\lambda^2 - \lambda(\alpha - 3\beta R^2\Omega^2) + a \cos(\Omega\tau)} - \\ & \frac{m\lambda^2 - m\Omega^2 - \lambda(\alpha - \beta R^2\Omega^2) + a}{\Omega[\alpha - 3\beta R^2\Omega^2 - 2m\lambda]} = 0. \end{aligned} \quad (3.22)$$

Equation (3.22) has four complex solutions.

In general, the rotating state will be linearly stable if there are no solutions to Eq.(3.22) with $Re[\lambda] > 0$. In practice, we find that changing a and τ while keeping all other parameters fixed, produces saddle-node, Hopf and double-Hopf bifurcations [40, 50]. In the former case,

a single real eigenvalue approaches zero, when

$$\tan(\Omega\tau) = \frac{m\Omega^2 - a}{\Omega(\alpha - 3\beta R^2\Omega^2)} . \quad (3.23)$$

Equation (3.23) gives the stability-line for the rotating state with small a and large τ . For large a and small τ , the stability changes through a double-Hopf bifurcation where two frequencies become unstable simultaneously, $\lambda = \pm i\omega_1, \pm i\omega_2 \neq 0$. Fig.3.9(a) shows the predicted composite stability-curve for the rotating state, combining both bifurcations. Plotted is the maximum τ , for fixed a , where $Re[\lambda] > 0$. Above the red line the rotating state is expected to be locally stable, and below it, unstable, which we have shown in [38].

As with the ring state, we compare our stability predictions to simulations, and determine the smallest value of $\tau(a)$ for which a swarm of $N = 600$ agents, initially prepared in the rotating state with a small, random perturbation, returns to a rotating state after a time of $t = 20000$. These points are shown with red diamonds in Fig.3.9(a) for several values of coupling. Again, we find excellent agreement with predictions. Another consequence of our analysis is the clear quantitative prediction of swarm bistability (between the red and blue curves in Fig.3.9) and noise-induced switching between ring and rotating patterns, which can now be precisely tested in experiments [17, 77, 78].

Lastly, just as with the ring state, we can compare the frequency of oscillations around the rotating state for $\tau(a)$ slightly below the double-Hopf bifurcation values, where we expect weak instability of modes orthogonal to the center-of-mass-motion. First we perform a simulation initially prepared in the rotating state with a small perturbation, and compute the peak frequency, ω^* , in the Fourier spectrum of $r_j - R$, where j is a randomly selected agent. An example is shown in the inlet panel of Fig.3.10(b) for ($a = 3.5, \tau = 1.059$). This peak frequency is compared to predictions from numerical solutions of Eq.(3.22) with $\lambda = \pm i\omega_1, \pm i\omega_2 \neq 0$ for a range of coupling strengths. In Fig.3.10(b) the smaller of the two frequencies, ω_1 is plotted along with ω^* – showing excellent agreement. Note that in this comparison, we do not subtract off the rotating state’s frequency, Ω , since r_j does not

oscillate in the rotating state but is equal to R .

3.2.2 Conclusion

In this section we studied the stability of ring and rotational patterns in a general swarming model with time-delayed interactions. We found that ring states change stability through Hopf bifurcations, where spatially periodic modes sustain oscillations in time. On the other hand, rotating states undergo saddle-node, Hopf, and double-Hopf bifurcations, where modes with orthogonal dynamics to the center-of-mass-motion change stability. For both states, the unstable oscillations correspond to dynamics not captured by standard mean-field approximations. Our results were verified in detail with large-agent simulations. Future work will extend our analysis to include the effects of repulsive forces, noise, and incomplete (and dynamic) communication topology – all of which are necessary for parametrically controlling real swarms of mobile robots.

3.3 Future work: On interacting swarm dynamics

The proposed future work uses the foundation of single swarm dynamics towards a comprehensive analysis of multiple interacting swarms, a topic which is still in its infancy, and remains an active area of research. Our aim is to develop new theories of interacting swarms dynamics in order to control multiple swarm behaviors. The future research will enable us to solve the problem of employing small and large swarms to sense and control other swarms. The interactions will be based on human leadership/animal hierarchical networks, but will be autonomous in application. Our results will aid in designing interacting swarms of robotic agents that can perform more complex tasks than a single swarm alone can, with resilience and robustness.

3.3.1 Statement of the problem

In recent years, improved mechanics in computer vision algorithms have enabled engineers to collect data and analyze the motions of individual agents in biological flocks, and formulate more accurate, empirical models for collective motion strategies of flocking species such as birds and fish [59, 81], resulting in the translation of swarm theory to communicating robotic systems. The swarm systems are particularly interesting to the robotics communities because they allow agents having simple rules to achieve complex objectives in ways that are scalable and robust to failures of individual agents.

Swarms of robots are now conducting tasks including search and rescue, density control, and mapping [58, 68]. The dynamics of single swarms and their bifurcation structures have been studied over the past decade, and it is well documented that swarms are able to converge to organized, coherent behaviors, which persist in spite of complicating factors such as communication delay, heterogeneity in agent dynamics, and environmental noise [63, 78]. In many applications, beyond the dynamics of single swarms, multiple swarms interact and produce even more complex spatio-temporal behavior [3, 48].

Our interacting swarms research will explore and develop control rules using external and internal forces to employ one swarm to modify the behavior of other swarms. In particular, to establish a task-oriented swarm control, we will consider swarm splitting techniques using swarm leader formation inspired by human leadership styles [29] and hierarchical networks in animal systems [25]. Bifurcation and stability analysis of interacting swarms will be viewed as high-dimensional nonlinear dynamical systems. We hope to answer questions such as how and when one swarm can capture/redirect another swarm, or how hierarchical topology might affect the motion and robustness of swarming patterns.

3.3.2 Background and relevance of previous work

In almost all models that predict a single swarm's dynamics, there are a relatively small number of controllable factors, since typically the agents operate based on just a few simple

rules and parameters. The parameter set is associated to the forces acting on the swarm which usually consists of a self-propulsion force and a potential function governing attracting and repelling forces between agents. In addition, latency, or delay, of communication between agents, as well as complex communication topology, may create new patterns not observed in ideal models which assume homogeneous communication.

Especially for delays that are fixed, one observes three basic swarming states or modes: translating, in which a center of mass of the swarm moves in a straight line with a constant velocity; ring, where the agents are splayed out on a ring in phase about a stationary center of mass; and rotating, where the center of mass itself rotates while the agents are clustered around it. Particularly, it has been shown that a fixed delay creates the rotational pattern, which is not observed in the case without any delay, both theoretically and experimentally [77, 78]. Furthermore, if we assume that the delays are range-dependent rather than uniform, we discover that rotational states which are typically periodic undergo a bifurcation that creates swarm dynamics on a torus. The observed bifurcation introduces additional frequencies into the dynamics, which may lead to quasi-periodic behavior of the swarm [75].

Generally, research on the spatio-temporal patterns of swarm dynamics presents results that are valid where the number of agents is assumed to be large. In such cases, we typically rely on mean-field equations to analytically predict transitions between regimes of different collective swarm motions as a function of model parameters, such as delay, coupling amplitude, or the radius outside of which communication delay is assumed. However, there is a limitation to mean-field analysis in swarm dynamics since it is based on an approximation of the center of mass of a swarm, failing to capture global bifurcation behavior, such as multi-stability. In particular, we have recently shown that it is necessary to test the relationship between a whole swarm model and the mean-field model [38, 39], as seen in the previous sections.

To guarantee swarming behavior experimentally, a control is typically employed [35, 64] to show convergence to a given state by relying on strict assumptions to ensure the desired

behavior. Consideration of emergent behaviors based on distance between agents or range-dependence has played some role in swarm control methods. In [91], two cases of control are analyzed, one with the nearest few neighbors allowing the swarm to follow the leader, and another without a leader but with a virtual spring damper mesh that connects the nearest neighboring robots. Another example of range-dependence in control method includes a coordination of an adaptive navigation mechanism in robotic swarms that assumes local interaction in a task-oriented control setting [66]. This method was inspired by a natural phenomenon: when schools of fish that are faced with obstacles, they can split themselves into a plurality of smaller groups to avoid collision and then merge into a single group after passing around the obstacles [92].

Range-dependent interactions in a single swarm have been extended to interacting swarms, helping to develop a control mechanism on how one swarm drives another to a desired location [55]. In any robotic swarm, delay also plays a role in sensing other agents. Every agent behaves as though the other agents are at the positions they occupied previously; therefore control actuation is affected. For instance, when two delay-coupled swarms with finite-scale sensing functions collide, they scatter, mill or flock together, depending on their relative motion, coupling strength, and delay [48]. These preliminary results suggest the possibility of having one swarm modify the intent of another by either capturing it, or redirecting the mean direction of the flock by taking the delay effect on a single swarm and extend it to interacting swarms. However, since most swarm-swarm applications are simulated on a case-by-case basis, there is no general theory that underscores the predictive principles for emergent dynamics in multiple swarm systems. In contrast to the abundance of promising results in works on single swarm dynamics, the analysis of multiple swarm interaction dynamics and control methods are still in a developmental stage.

3.3.3 General methodology and procedures

Notions such as nearest neighbors and range-dependence introduce a sense of quantitative order, which induces a hierarchical leadership structure in the relationships among agents in

swarming systems. The ability to infer and control differential influence is a vital component in understanding emergent group actions among interacting swarms. To effectively create a chain of command in a swarm of mobile agents, we first conceptualize different types of leadership analogous to those of hierarchical network structures in human leadership. There are different types of human leadership and each style is used in accordance with task and goal-specific purposes [29]. Consider an army as an analogy: There is a commander allocating different tasks to each battalion within the army; the commander has a holistic view of the army’s goals and how to actualize them. Each battalion has a leader that can interact with all of its soldiers. The commander gives orders to the battalion leaders and collects information from them. In addition, the commander can either be a battalion leader, or can operate from outside the battalions, unconnected to the individual soldiers. There can be a ranking among the battalion leaders so that if one leader is compromised, an emergent structure is in place to sustain a chain of command at a given time. We will use the ideas exemplified in the army analogy of hierarchical network structure to organize and derive mechanisms for interacting swarms to accommodate more task-oriented dynamics. For instance, we will study the bifurcations of swarms whose communication topologies [42] have hubs, directed (asymmetric) links, and fractal structures composed of teams of teams.

At first, with the range-dependent swarming model we used in [75], we choose an agent as a leader at random to follow an independent and user-specified path. The basic idea is to strengthen local coupling to the leader so that other agents within the prescribed range with respect to the leader are drawn to the designated path. We note that it is not a trivial task to find a suitable potential function that can capture some agents within ϵ radius of the leader. We have tried the well potential in [79], and attracting Morse potential from [60], but we seek to devise a better mechanism for the leader attracting other agents by designing a potential function that takes into account a relationship between leader and followers in terms of their new positions. Some potential functions, such as Lennard-Jones, can diverge when agents approach one another. This may create instabilities that require special treatment in case of swarm dynamics analysis and simulations.

Building on the initial work, we will create rules for leader formation dynamically, and methods to sustain the leadership structure from a single to multiple swarms in terms of explicit hierarchical topology. A general mathematical model in [25] describes hierarchical networks in animal systems such as schooling, herding, or flocking. More specifically for delay-coupled swarms, interaction through heterogeneous networks that have a relatively small fraction of highly connected nodes defined as "motherships" [42] can mimic the influence of leaders in social networks or the insertion of highly interacting controllers into a network of autonomous mobile robots, and can alter a swarms motion. We will explore how hierarchical network combined with the delay effects among swarms [48] may help us to specify generic conditions under which one swarm can capture or redirect other swarms depending on interaction rules and/or initial swarm states. Hierarchical topology will help to design swarms that can be more easily controlled, and more robust to noise and mechanical failures.

3.3.4 Explanation of new or unusual techniques

So far, the majority of research in swarm-control theory involves designing interfaces and algorithms that allow a human operator to influence swarm systems [55, 66]. The proposed research seeks to control interacting swarms using the foundation of swarm dynamics, by observing emergent behaviors of multiple swarms from a leader creation. This is an uncharted territory in the field of autonomy.

It should be noted that there is no general theory in the dynamics of multiple interacting swarms explaining when and how changes in pattern formations occur. By treating interacting swarms as high-dimensional nonlinear dynamical systems and analyzing their bifurcation structures, we will be able to identify changes in dynamic modal structures in different regions of parameter space due to effects of communication delay or noise. For instance, the U.S. Naval Research Laboratory (NRL) nonlinear dynamics group has recently identified techniques for embedding swarms on manifolds. Such techniques facilitate exact calculations of swarm pattern stability, and will be used in the interacting-swarms problems

discussed above.

Based on theory from the analysis of bifurcation structures, we can classify communication parameters of swarms by region. The parameters can be optimized dynamically in order to mitigate the effects of noise and delay on a particular spatio-temporal pattern, or even use them as a way to optimally control the swarms. In addition to model-based analysis, we plan to explore model-free techniques, such as machine-learning [22], to infer noise and delay sources in a swarm from position and velocity observations.

Most known bifurcation results related to delay-coupled swarms rely on mean-field approximation techniques. As a consequence, the utility of applying macroscopic theory as a guide for predicting and controlling swarms of mobile robots has been limited. To overcome, along with case specific methods [38, 39], rigorous numerics methods that appear in the previous chapter [45, 73] may be used to guarantee a precise bound on the error for our specific problem in contrast to general *a priori* estimates for the standard expected error. The classical implicit function theorem, which guarantees only the existence of a unique solution to the equation, is modified for use in numerics with interval arithmetic, such that we can also guarantee a precise error bound.

3.3.5 Expected results and their significance

The results of the proposed work will help develop general principles and tools for controlling multiple interacting swarms. We expect such interactive swarm control to open up new areas of research in the dynamics of multi-agent systems control. If successful, our control results with the modeling of leadership styles will represent a large step forward in the field of autonomy. We expect our approach to be a major leap in controlling the behavior of multi-agent autonomous systems, ensuring their resilience.

In terms of robotics platforms, a comprehensive interacting swarm-control theory will give us a theoretical understanding for current and future experiments at NRL and the University of Pennsylvania with interacting swarms of mobile robots. Furthermore, our results may help design interacting swarms that are robust to internal and external perturbations

and interference, and/or that can perform more complex tasks which a single swarm alone cannot accomplish.

Finally, since interacting complex groups occur in research fields not just limited to physically coupled groups, our research can show in such systems how to achieve more resilient and robust behavior regarding the multi-group system as a unified body. Such fields include biological or social group dynamics, bacterial cluster formation, as well as recruitment of individuals and avoidance behavior in the presence of a threat or disease.

Bibliography

- [1] M. Aldana, V. Dossetti, C. Huepe, V. M. Kenkre, and H. Larralde. Phase transitions in systems of self-propelled agents and related network models. *Phys. Rev. Letts.*, 98:095702, 2007.
- [2] G. Ansman, K. Lehnertz, and U. Feudel. Self-induced switchings between multiple space-time patterns on complex networks of excitable units. *Phys. Rev. X*, 6:011030, Mar 2016.
- [3] H. Armbruster, S. Martin, and A. Thatcher. Elastic and inelastic collisions of swarms. *Physica D: Nonlinear Phenomena*, 344:45–57, Apr. 2017.
- [4] F. Arrichiello, D. N. Liu, S. Yerramalli, A. Pereira, J. Das, U. Mitra, and G. S. Sukhatme. Effects of underwater communication constraints on the control of marine robot teams. In *2009 Second International Conference on Robot Communication and Coordination*, pages 1–8, 2009.
- [5] R. Aubourg. *Red coral in the Mediterranean sea*. Wikimedia Commons, 2017.
- [6] P. Bandyopadhyay. Trends in biorobotic autonomous undersea vehicles. *IEEE Journal of Oceanic Engineering*, 30:109, 2005.
- [7] L. Bayndr. A review of swarm robotics tasks. *Neurocomputing*, 172:292 – 321, 2016.
- [8] M. Brambilla, E. Ferrante, M. Birattari, and M. Dorigo. *Swarm Intelligence*, 7:1, 2013.
- [9] E. O. Budrene and H. Berg. Dynamics of formation of symmetrical patterns by chemo-tactic bacteria. *Nature*, 376:49–53, 1995.
- [10] M. J. Capinski, E. Fleurantin, and J. D. Mireles James. *Computer assisted proofs of two-dimensional attracting invariant tori for odes*. Discrete and Continuous Dynamical Systems, Series A, 2020.
- [11] Y. Chuang, M. R. D' Orsogna, D. Marthaler, A. L. Bertozzi, and L. S. Chayes. State transitions and the continuum limit for a 2D interacting, self-propelled particle system. *Physica D: Nonlinear Phenomena*, 232(1):33–47, Aug. 2007.
- [12] M. G. Crandall and P. H. Rabinowitz. *Bifurcation from simple eigenvalues*. Journal of Functional Analysis, 8:321–340, 1971.

- [13] S. Das, C. Dock, Y. Saiki, M. S-Flores, E. Sander, J. Wu, and J. Yorke. *Measuring quasiperiodicity*. *Europhysics Letters*, 114(4):40005, 2016.
- [14] J. P. Desai, J. P. Ostrowski, and V. Kumar. Modeling and control of formations of nonholonomic mobile robots. In *IEEE Transactions on Robotics and Automation*, volume 17(6), pages 905–908, 2001.
- [15] M. R. D’Orsogna, Y. L. Chuang, A. L. Bertozzi, and L. S. Chayes. *Phys. Rev. Lett.*, 96:104302, 2006.
- [16] L. Edelstein-Keshet, D. Grunbaum, and J. Watmough. Do travelling band solutions describe cohesive swarms? An investigation for migratory locusts. *Journal of Mathematical Biology*, 36(6):515–549, July 1998.
- [17] V. Edwards, P. deZonia, M. A. Hsieh, J. Hindes, I. Triandof, and I. B. Schwartz. *Delay-Induced Swarm Pattern Bifurcations in Mixed-Reality Experiments, Chaos [under review]*.
- [18] U. Erdmann, W. Ebeling, and A. S. Mikhailov. Noise-induced transition from translational to rotational motion of swarms. *Phys. Rev. E*, 71:051904, 2005.
- [19] J. Fehrenbach, J. Narski, J. Hua, S. Lemercier, A. Jelic, C. Appert-Rolland, S. Donikian, J. Pettr, and P. Degond. Time-delayed follow-the-leader model for pedestrians walking in line. 2014.
- [20] J. Fink, A. Ribeiro, and V. Kumar. Robust control for mobility and wireless communication in cyberphysical systems with application to robot teams. *Proceedings of the IEEE*, 100(1):164–178, 2012.
- [21] J. Fink, A. Ribeiro, and V. Kumar. Robust control of mobility and communications in autonomous robot teams. *IEEE Access*, 1:290–309, 2013.
- [22] M. Fliess and C. Join. Machine learning and control engineering: The model-free case. *arXiv e-prints*, page arXiv:2006.05738, June 2020.
- [23] E. Forgoston and I. B. Schwartz. Delay-induced instabilities in self-propelling swarms. *Phys. Rev. E*, 77:035203(R), 2008.
- [24] L. B. G. Santangelo and M. Iannelli. *Population dynamics and conservation biology of the over-exploited Mediterranean red coral*. 2007.
- [25] J. Garland, A. M. Berdahl, J. Sun, and E. M. Bollt. Anatomy of leadership in collective behaviour. *Chaos: An Interdisciplinary Journal of Nonlinear Science*, 28(7):075308, 2018.
- [26] V. Gazi. Swarm aggregations using artificial potentials and sliding-mode control. *IEEE Transactions on Robotics*, 21(6):1208–1214, Dec 2005.
- [27] P. Géry. *Corallium rubrum (Linnaeus, 1758) - Banyuls-sur-Mer, Sec deRédéris: 08/84*. Wikimedia Commons, 31 July 2011.

- [28] L. Giuggioli, T. J. McKetterick, and M. Holderied. Delayed Response and Biosonar Perception Explain Movement Coordination in Trawling Bats. *PLOS Computational Biology*, 11(3):e1004089, 2015.
- [29] D. Goleman. Leadership that gets results. *Leadership Perspectives*, pages 85–96, 2017.
- [30] W. J. F. Govaerts. *Numerical methods for bifurcations of dynamical equilibria*. Society for Industrial and Applied Mathematics (SIAM), Philadelphia, PA, 2000.
- [31] J. K. Hale. *Theory of Functional Differential Equations*. Applied Mathematical Sciences. Springer-Verlag, New York, 1977.
- [32] J. K. Hale and S. M. V. Lunel. *Introduction to Functional Differential Equations*. Springer, New York, 1993.
- [33] H. Hartle and R. Wackerbauer. Transient chaos and associated system-intrinsic switching of spacetime patterns in two synaptically coupled layers of morris-lecar neurons. *Phys. Rev. E*, 96:032223, Sep 2017.
- [34] F. Hartung, T. Krisztin, H. Walther, and J. Wu. *Chapter 5 Functional Differential Equations with State-Dependent Delays: Theory and Applications*, volume 3 of *Handbook of Differential Equations: Ordinary Differential Equations*, pages 435–545. 2006.
- [35] C. R. Heckman, M. A. Hsieh, and I. B. Schwartz. Controlling basin breakout for robots operating in uncertain flow environments. In *Experimental Robotics*, pages 561–576. Springer, Cham, 2016.
- [36] D. Helbing and P. Molnar. Social force model for pedestrian dynamics. *Physical Review E*, 51(5):4282–4286, 1995.
- [37] J. Hindes and M. Assaf. Degree dispersion increases the rate of rare events in population networks. *Phys. Rev. Lett.*, 123:068301, 2019.
- [38] J. Hindes, V. Edwards, S. Kamimoto, G. Stantchev, and I. B. Schwartz. Stability of milling patterns in self-propelled swarms on surfaces. *Phys. Rev. E*, 102:022212, Aug 2020.
- [39] J. Hindes, V. Edwards, S. Kamimoto, I. Triandaf, and I. B. Schwartz. Unstable modes and bistability in delay-coupled swarms. *Physical Review E*, 101(4):042202, 2020.
- [40] J. Hindes and C. R. Myers. Driven synchronization in random networks of oscillators. *Chaos: An Interdisciplinary Journal of Nonlinear Science*, 25(7):073119, 2015.
- [41] J. Hindes and I. B. Schwartz. Rare slips in fluctuating synchronized oscillator networks. *Chaos: An Interdisciplinary Journal of Nonlinear Science*, 28(7):071106, 2018.
- [42] J. Hindes, K. Szwajkowska, and I. B. Schwartz. Hybrid dynamics in delay-coupled swarms with mothership networks. *Phys. Rev. E*, 94:032306, Sep 2016.
- [43] M. A. Hsieh, A. Cowley, J. F. Keller, L. Chaimowicz, B. Grocholsky, V. Kumar, C. J. Taylor, Y. Endo, R. C. Arkin, B. Jung, D. F. Wolf, G. S. Sukhatme, and D. C. MacKenzie. Adaptive teams of autonomous aerial and ground robots for situational awareness. *Journal of Field Robotics*, 24(1112):991–1014, 2007.

- [44] A. Jadbabaie, Jie Lin, and A. S. Morse. Coordination of groups of mobile autonomous agents using nearest neighbor rules. *IEEE Transactions on Automatic Control*, 48(6):988–1001, June 2003.
- [45] S. Kamimoto, H. K. Kim, E. Sander, and T. Wanner. A computer-assisted study of red coral population dynamics. *To appear in Pure and Applied Functional Analysis*.
- [46] J. A. Y. Kathleen T. Alligood, Tim D. Sauer. *Chaos: An Introduction to Dynamical Systems*. Springer, corrected edition, 1996.
- [47] H. B. Keller. *Lectures on numerical methods in bifurcation problems*, volume 79 of *Tata Institute of Fundamental Research Lectures on Mathematics and Physics*, with notes by A. K. Nandakumaran and Mythily Ramaswamy. Published for the Tata Institute of Fundamental Research, Bombay; by Springer-Verlag, Berlin, 1987.
- [48] C. Kolon and I. B. Schwartz. The dynamics of interacting swarms. *arXiv preprint arXiv:1803.08817*, 2018.
- [49] D. Kularatne, E. Forgoston, and M. A. Hsieh. Using control to shape stochastic escape and switching dynamics. *Chaos*, 29(5):053128, 2019.
- [50] Y. A. Kuznetsov. *Elements of Applied Bifurcation Theory*. Springer, Berlin, 2004.
- [51] L. D. M. L. Bramanti, G. Magagnini and G. Santangelo. *Recruitment, early survival and growth of the Mediterranean red coral Corallium rubrum (L 1758), a 4-year study*. Journal of Experimental Marine Biology and Ecology, 314(1):69–78, 2005.
- [52] M. I. L. Bramanti and G. Santangelo. *Mathematical modelling for conservation and management of gorgonians corals: youngs and olds, could they coexist?* Ecological Modelling 220(21):2851–2856, 2009.
- [53] R. M. Lee, D. H. Kelley, K. N. Nordstrom, N. T. Ouellette, and W. Losert. Quantifying stretching and rearrangement in epithelial sheet migration. *New Journal of Physics*, 15(2), Feb. 2013.
- [54] S.-H. Lee. Predator’s attack-induced phase-like transition in prey flock. *Physics Letters A*, 357(4-5):270–274, Sept. 2006.
- [55] W. Lee and D. Kim. Autonomous shepherding behaviors of multiple target steering robots. *Sensors (Basel, Switzerland)*, 17(12), November 2017.
- [56] J. P. Lessard, E. Sander, and T. Wanner. *Rigorous continuation of bifurcation points in the diblock copolymer equation*. Journal of Computational Dynamics, 4(1–2):71–118, 2017.
- [57] H. Levine, W. J. Rappel, and I. Cohen. *Phys. Rev. E*, 63:017101, 2000.
- [58] H. Li, C. Feng, H. Ehrhard, Y. Shen, B. Cobos, F. Zhang, K. Elamvazhuthi, S. Berman, M. Haberland, and A. L. Bertozzi. Decentralized stochastic control of robotic swarm density: Theory, simulation, and experiment. In *2017 IEEE/RSJ International Conference on Intelligent Robots and Systems (IROS)*, pages 4341–4347, Sep. 2017.

- [59] J. Li and A. H. Sayed. Modeling bee swarming behavior through diffusion adaptation with asymmetric information sharing. *EURASIP Journal on Advances in Signal Processing*, 2012(1):18, Jan 2012.
- [60] Y. li Chuang, M. R. DOrsogna, D. Marthaler, A. L. Bertozzi, and L. S. Chayes. State transitions and the continuum limit for a 2d interacting, self-propelled particle system. *Physica D: Nonlinear Phenomena*, 232(1):33 – 47, 2007.
- [61] B. Lindley, L. Mier-y-Teran-Romero, and I. B. Schwartz. Noise induced pattern switching in randomly distributed delayed swarms. In *2013 American Control Conference*, pages 4587–4591, June 2013.
- [62] M. C. Marchetti, J. F. Joanny, S. Ramaswamy, T. B. Liverpool, J. Prost, M. Rao, and R. A. Simha. *Rev. Mod. Phys.*, 85:1143, 2013.
- [63] L. Mier-y Teran-Romero, E. Forgoston, and I. B. Schwartz. Noise, bifurcations, and modeling of interacting particle systems. *IEEE/RSJ International Conference on Intelligent Robots and Systems*, pages 3905–3910, 2011.
- [64] D. S. Morgan and I. B. Schwartz. Dynamic coordinated control laws in multiple agent models. *Physics Letters A*, 340(1):121 – 131, 2005.
- [65] N. Nagy, Z. Akos, D. Biro, and T. Vicsek. Hierarchical group dynamics in pigeon flocks. *Nature*, 464:890–893, 2010.
- [66] Y. Nishimura, G. Lee, N. Y. Chong, S. H. Ji, and Y.-J. Cho. Adaptive navigation control for swarms of autonomous mobile robots. In A. Barrera, editor, *Advances in Robot Navigation*, chapter 5. IntechOpen, Rijeka, 2011.
- [67] A. A. Polezhaev, R. A. Pashkov, A. I. Lobanov, and I. B. Petrov. Spatial patterns formed by chemotactic bacteria Escherichia coli. *The International Journal of Developmental Biology*, 50:309–314, Jan. 2006.
- [68] R. K. Ramachandran, K. Elamvazhuthi, and S. Berman. *An Optimal Control Approach to Mapping GPS-Denied Environments Using a Stochastic Robotic Swarm*, pages 477–493. Springer International Publishing, Cham, 2018.
- [69] S. M. Rump. *INTLAB - INTerval LABoratory, Developments in Reliable Computing*. pages 77–104. Kluwer Academic Publishers, Dordrecht, <http://www.ti3.tuhh.de/rump/>, 1999.
- [70] D. B. S. Beslin and V. de Angelis. *Small denominators: No small problem*. Mathematics Magazine, 71(2):132–138, 1998.
- [71] A. G. Salinger, E. A. Burroughs, R. P. Pawlowski, E. T. Phipps, and L. A. Romero. Bifurcation tracking algorithms and software for large scale applications. *International Journal of Bifurcation and Chaos*, 15(03):1015–1032, 2005.
- [72] E. Sander and J. D. Meiss. *Birkhoff averages and rotational invariant circles for area-preserving maps*. *Physica D*, 411:132569, 2020.

- [73] E. Sander and T. Wanner. *Validated saddle-node bifurcations and applications to lattice dynamical systems*. SIAM Journal on Applied Dynamical Systems, 15(3):1690–1733, 2016.
- [74] E. Sander and T. Wanner. *Equilibrium validation in models for pattern formation based on Sobolev embeddings*. Discrete and Continuous Dynamical Systems, Series B, 2020,.
- [75] I. B. Schwartz, V. Edwards, S. Kamimoto, K. Kasraie, M. Ani Hsieh, I. Triandaf, and J. Hindes. Torus bifurcations of large-scale swarms having range dependent communication delay. *Chaos: An Interdisciplinary Journal of Nonlinear Science*, 30(5):051106, 2020.
- [76] K. Szwakowska, L. M.-y.-T. Romero, and I. B. Schwartz. Collective Motions of Heterogeneous Swarms. *IEEE Transactions on Automation Science and Engineering*, 12(3):810–818, July 2015.
- [77] K. Szwakowska, I. B. Schwartz, and T. W. Carr. State transitions in generic systems with asymmetric noise and communication delay. In *2018 11th International Symposium on Mechatronics and its Applications (ISMA)*, pages 1–6, March 2018.
- [78] K. Szwakowska, I. B. Schwartz, L. Mier-y Teran Romero, C. R. Heckman, D. Mox, and M. A. Hsieh. Collective motion patterns of swarms with delay coupling: Theory and experiment. *Phys. Rev. E*, 93:032307, Mar 2016.
- [79] H. G. Tanner, A. Jadbabaie, and G. J. Pappas. Stable flocking of mobile agents part ii: dynamic topology. In *42nd IEEE International Conference on Decision and Control (IEEE Cat. No.03CH37475)*, volume 2, pages 2016–2021 Vol.2, Dec 2003.
- [80] H. G. Tanner, A. Jadbabaie, and G. J. Pappas. Flocking in fixed and switching networks. *IEEE Transactions on Automatic Control*, 52(5):863–868, May 2007.
- [81] G. Theraulaz, E. Bonabeau, S. C. Nicolis, R. V. Solé, V. Fourcassié, S. Blanco, R. Fournier, J.-L. Joly, P. Fernández, A. Grimal, P. Dalle, and J.-L. Deneubourg. Spatial patterns in ant colonies. *Proceedings of the National Academy of Sciences*, 99(15):9645–9649, 2002.
- [82] C. M. Topaz, Bertozzi, and A. L. Swarming Patterns in a Two-Dimensional Kinematic Model for Biological Groups. *SIAM Journal on Applied Mathematics*, 65(1):152–174, Jan. 2004.
- [83] K. r. Tunstrø m, Y. Katz, C. C. Ioannou, C. Huepe, M. J. Lutz, and I. D. Couzin. Collective states, multistability and transitional behavior in schooling fish. *PLoS computational biology*, 9(2):e1002915, Jan. 2013.
- [84] J. B. van den Berg, J. P. Lessard, and E. Queirolo. *Rigorous verification of Hopf bifurcations via desingularization and continuation*. arXiv:2006.13373 [math.DS], 2020.
- [85] T. Vicsek, A. Czirok, E. Ben-Jacob, I. Cohen, and O. Shochet. Novel type of phase transition in a system of self-driven particles, 2006.
- [86] T. Vicsek and A. Zafeiris. Collective motion. *Physics Reports*, 517(3):71 – 140, 2012. Collective motion.

- [87] C. Viragh, G. Vasarhelyi, N. Tarcai, Szorenyi, and et al. Flocking algorithm for autonomous flying robots. *Bioinspiration & biomimetics*, 9(2):025012, 2014.
- [88] T. Wanner. Bifurcation theory course notes. Department of Mathematical Sciences, George Mason University, Spring 2018.
- [89] T. Wanner. *Computer-assisted equilibrium validation for the diblock copolymer model*. Discrete and Continuous Dynamical Systems, Series A, 37(2):1075–1107, 2017.
- [90] T. Wanner. *Computer-assisted bifurcation diagram validation and applications in materials science*. Proceedings of Symposia in Applied Mathematics, 74:123–174, 2018.
- [91] J. Wiech, V. A. Eremeyev, and I. Giorgio. Virtual spring damper method for nonholonomic robotic swarm self-organization and leader following. *Continuum Mechanics and Thermodynamics*, 30(5):1091–1102, Sep 2018.
- [92] E. O. Wilson. *Sociobiology : the new synthesis*. Belknap Press of Harvard University Press, Cambridge, Mass., 2000.
- [93] W. Wu and F. Zhang. Cooperative exploration of level surfaces of three dimensional scalar fields. *Automatica*, 47(9):2044–2051, Sept. 2011.
- [94] L. M. y Teran-Romero, E. Forgoston, and I. B. Schwartz. Coherent pattern prediction in swarms of delay-coupled agents. *IEEE Transactions on Robotics*, 28(5):1034–1044, Oct 2012.
- [95] L. M. y Teran-Romero and I. B. Schwartz. Capturing pattern bi-stability dynamics in delay-coupled swarms. *EPL (Europhysics Letters)*, 105(2):20002, jan 2014.
- [96] M. ying Ani Hsieh, P. Srivastava, V. Kumar, and C. J. Taylor. Composable communication constraint-based control. In D. W. Gage, editor, *Mobile Robots XVII*, volume 5609, pages 192 – 200. International Society for Optics and Photonics, SPIE, 2004.

Curriculum Vitae

Sayomi Kamimoto is originally from Japan. She currently resides in Washington DC with her husband Emmanuel, their children and plants. After finishing her PhD, Sayomi plans to get back to playing the piano, hopefully for fun this time But in a meantime, from January 2021, she is set to start her postdoctoral research position at the US. Naval Research Laboratory as a National Research Council Research Associate for the next few years. (As of December 2020)